Technische Universität München
TUM School of Engineering and Design

On the incorporation of industrial constraints in node-based optimization for car body design

Efthymios Papoutsis

Vollständiger Abdruck der von der TUM School of Engineering and Design der Technischen Universität München zur Erlangung eines

Doktors der Ingenieurwissenschaften (Dr.Ing.)

genehmigten Dissertation.

Vorsitz: Priv.-Doz. Dr.-Ing. habil. Stefan Kollmannsberger

Prüfer*innen der Dissertation:

1. Prof. Dr.-Ing. Kai-Uwe Bletzinger
2. Prof. Dr.-Ing. habil. Fabian Duddeck

Die Dissertation wurde am 04.07.2022 bei der Technischen Universität München eingereicht und durch die TUM School of Engineering and Design am 28.11.2022 angenommen.

Schriftenreihe des Lehrstuhls für Statik TU München

Band 55

Efthymios Papoutsis

On the incorporation of industrial constraints in node-based optimization for car body design

München 2023

Abstract

With the advance of computing technology in the past decades, structural optimization has been in the focus of attention of the research community and lately integrated in the automotive industry design process. Naturally, industrial functional requirements impose constraints on the admissible optimal shapes. Herein, the focus is on reducing the existing disparity between numerically optimized designs and those which satisfy such industrial constraints.

In this work, three different methods for the incorporation of industrial constraints in node-based structural optimization with Vertex Morphing, an explicit kernel-based parametrization method, are presented. It is an attempt to highlight that different components of an optimization problem's formulation can be modified in order to satisfy requirements and inspire the implementation of more constraints with novel approaches. Firstly, a constraint that prohibits undercuts from developing in the geometry is proposed. The local point-wise problem is converted into an aggregate undercut volume minimization problem with improved computational efficiency. Secondly, reflection symmetry of optimal designs is investigated. Instead of formulating a constraint function and adding it to the mathematical optimization problem, the Vertex Morphing parametrization is enhanced to yield symmetric geometry updates. Finally, a four-dimensional extension of Vertex Morphing is proposed with the inclusion of nodal thickness design variables. The simultaneous optimization of thickness and nodal coordinates design variables facilitates mass-constrained shape optimization. The industrial constraint of constant thickness sheet metals was solved by introducing a reparametrization of the thickness variables based on an s-shaped function. In addition, a root-finding algorithm is utilized to tackle the problem of proportionality of the step length ratio of shape to thickness design updates during optimization.

All methods were successfully implemented in a solver-agnostic node-based structural optimization workflow in order to be integrated in the car body design process at BMW. Several industrial applications were optimized to test and prove the robustness of the methods for complex engineering problems.

Contents

Chapter 1

Introduction

Structural numerical optimization techniques have been applied with different forms in the automotive industry during the past forty years. With the advance of computing technology and numerical methods, lowering of computational effort became feasible during the '90s. To this end, software vendors have been forced under the pressure of competition for lightweight and performance-optimal designs to include such methods in their products. At the same time, manufacturing engineering imposes certain hard geometric constraints on the optimal shapes which cannot be neglected and need to be carefully treated. Thus, considerable effort in the last two decades has been devoted to including such constraints in the structural optimization methods, both in topology and shape optimization, so that the advantages in optimality can be harvested from the industry.

Any sheet metal vehicle component must fulfill specifications in three distinct areas: it must withstand the static and dynamic loads that "describe" its structural purpose, it should be as light as possible, and it must

be manufacturable with the intended manufacturing method. Numerical structural optimization suggests a design with respect to structural optimality of the former conditions. A disparity between the numbers of numerically optimized designs and those who satisfy the manufacturing constraints persists even though optimization techniques are constantly refined. As expected, manual design changes on the optimal geometry so that it complies to the manufacturing process can have adverse effects on the optimality of the component. This thesis aims to reduce this existing chasm in the framework of node-based shape optimization.

1.1 Node-based parameterization for shape optimization

Numerical shape and topology optimization have been growing independently as research fields in the past decades, each of them attracting supporting groups in academia. Maximizing performance of an existing component with respect to material cost is particularly relevant for the automotive industry. One of the most well-researched areas in shape optimization is that of shape parametrization techniques or, in other words, the question of how to describe the geometry and its shape variation during optimization. The two most common approaches are the CAD-based, where design variables are CAD parameters, and the parameter-free or node-based approach, where design variables are the nodal coordinates of the computational model. A more comprehensive report on the parametrization techniques is found in [20, 79, 80]. The main advantages of a node-based approach are that it offers a large design space that does not impose strong assumptions on the optimal geometry shape as is the case with CAD-based techniques. This work builds on an existing node-based parametrization technique named Vertex Morphing. The development of the adjoint method by Lions and Pironneau [61, 73] in the ’70s has enabled the extensive combination of gradient-based optimization algorithms and node-based shape parametrization since the computational cost to calculate the derivatives of the objective function with respect to the design variables is independent of the number of design variables.

Various node-based formulations have been proposed for the handling of large-scale shape optimization problems, as are usually encountered in the industry. The main challenge in node-based shape optimization is the elimination of high frequency noise from the shape derivatives and the extraction of dominant information. Both explicit methods, like kernel-based filtering of the sensitivities, and implicit ones, where the numerical solution of a partial differential equation represents the smoothed shape update, have been proposed. However, to the author's knowledge, the first effort to consistently incorporate a filtering technique formulation in optimization theory has been done in [20, 49] with the Vertex Morphing method.

In Vertex Morphing [20, 49], the simulation model can be used directly for shape optimization since the design variables are automatically generated from the discretized geometry. In addition to the geometry field, a control field and a map that relates it to the geometry field are defined, in which the mathematical optimization problem is formulated and solved. The mapping between geometry field and design control field is achieved through convolution of a kernel function with the design surface. In its discretized form, the convolution integral transforms into a weighted summation of a matrix vector multiplication. Surface smoothness and mesh regularity criteria in the geometry field are satisfied through this filtering. Some industrial applications of the method can be found in [14, 36, 49, 66, 70].

1.2 Inclusion of constraints in structural optimization

Naturally, the next step after the success of node-based shape optimization in the industry is the incorporation of geometric constraints to steer the shape optimization towards desired resultant designs. Herein, the terms "geometric" and "manufacturing" are used interchangeably. In node-based shape optimization geometric constraints are, more often than not, point-wise, in that they are applied on the nodal coordinates design variables and must be satisfied for all of them. Introducing a constraint for every design variable increases dramatically the adjoint sensitivity analysis computation time. Thus, the topic of constraint ag-

gregation in order to reduce this time cost has been well discussed in literature [12, 54, 74].

One of the first geometric constraints that attracted research interest was that of length scale control of structural members in discretized topology optimization, since it is tied to the existence of solutions and obtaining mesh-independent results [42, 43, 75, 100]. As a remedy to the same problem, global total perimeter constraints have also been proposed [8, 46]. In similar spirit are the research publications in thickness control with a level-set based approach to ensure manufacturability and structural robustness [6, 27, 29, 44].

With regard to geometric constraints arising directly from manufacturing limitations, contributions on demolding constraints for cast parts have been made, wherein no undercut regions in optimal designs are allowed to permit the removal of casting molds [2, 59, 60, 92, 95, 96]. Recent developments in additive manufacturing have facilitated the exploitation of topology optimization design complexity and initiated the research on a new range of manufacturing constraints tied to the process. Namely, surface angle, with respect to the build direction, of structural parts overhanging over void should be constrained to a permitted value [1, 39].

Shape optimization with geometric and manufacturing constraints has attracted less attention than topology optimization. In the framework of node-based shape optimization, point-wise [55] packaging constraints have been recently successfully included in the Vertex Morphing formulation [66]. A minimum thickness constraint in Vertex Morphing and a comparison of different aggregation functions for point-wise geometric constraints have been investigated in [40]. Moreover, a series of manufacturing constraints—namely different types of symmetry, demolding, curvature and minimum member size constraints—were formulated in terms of the finite element node coordinates in a parameter-free shape optimization [81–83].

One of the biggest challenges the automotive industry faces today is weight reduction (lightweighting). Topology optimization essentially answers the question of optimal distribution of material in a domain

under a mass constraint [18]. The two most widely applied topology optimization methods are the density-based [16], wherein a Lagrangian approach is utilized, and the level-set-based, wherein mostly an Eulerian approach is used [3, 7, 69, 84, 93]. For a detailed comparative review of the methods, which is out of the scope of this thesis, the reader is referred to the literature [34, 78, 88]. In shape optimization, on the other hand, mass change is trivial since the topology of the structure cannot be changed. Hence, volume-constrained shape optimization has been researched in the form of simultaneous shape and topology optimization. Several attempts have been made to combine these two optimization approaches. In the bubble method [37] hole nucleation steps are interlaced with shape optimization steps to achieve optimal shape of the holes and Lagrangian mesh surface. In similar spirit is the, also Lagrangian-based, approach of Christiansen et al. [31]. The topological gradient method, first introduced in the aforementioned bubble method, [26, 37, 45, 90] was also incorporated into level-set based formulations to accommodate Eulerian-based staggered shape and topology optimization approaches [5, 9, 25, 67, 94]. Combined approaches in a consecutive manner wherein a topology optimized design is subsequently the starting point of a shape optimization, or vice versa, have been also proposed in the literature [22, 62, 68, 72]. Ansola et al. proposed a staggered approach where shape and topology optimization steps are alternated during the process and shape and density design variables are optimized sequentially [10, 11]. Hassani et al. combined CAD-based shape and density-based topology design variables to optimize shell structures with a Method of Moving Asymptotes (MMA) algorithm [47]. To the author's knowledge, to date there is no thorough investigation on the combination of topology optimization with parameter-free shape optimization approaches.

1.3 Goal of thesis

As explored above, although geometric and manufacturing constraints have found their way into structural optimization—admittedly mostly into topology optimization—in node-base shaped optimization there has been less effort to explore methods of constraint incorporation other than directly adding mathematically formulated constraint functions to

the problem. At the same time, volume constraints in node-based shape optimization are still to be tackled sufficiently. As such, this thesis deals with the inclusion of geometric constraints in node-based structural optimization with the Vertex Morphing parameterization, which are imposed by manufacturing and physical limitations in the automotive industry. The focus was kept on computational efficiency of the methods and ease of use for the engineer since the goal was to incoroporate the methods in an in-house structural node-based optimization software used during the design process. To this end, different approaches of incorporating geometric constraints were explored with the wish to work as inspiration for the implementation of further geometric constraints. Specifically, reparameterization of the design variables by enhancing the existing mapping or by introducing a new one is explored in this thesis. Moreover, reduction methods of point-wise geometric constraints to a sole global constraint simplify the optimization problem.

As an example of the reduction approach discussed above, the case of a sheet metal forming or casting constraint is presented. Undercut regions are strictly prohibited in optimal designs so that they are manufacturable with the intended manufacturing method. Instead of imposing pointwise constraints on the finite element model nodes and subsequently aggregating them with formulations such as the Kreisselmeier-Steinhauser function, we propose a single constraint equal to a domain integral representing the imaginary volume “trapped” in the undercut regions. A fast ray tracing-like technique was utilized for the discrete approximation of the constraint continuous integral. As such, the original undercut constraint is reduced to a volume minimization problem. Shape sensitivities of the undercut constraint are then easily derived. In addition, the maximum allowable surface angle is defined by the user and can be either positive or negative, allowing both undercut and slab regions, by introducing a buffer zone and modifying the direction of the ray tracing.

Secondly, a new method for a reflection-symmetry constraint is presented. Avoiding the addition of one more mathematical constraint on the optimization problem, the method is based on a reparametrization of the design variables. This reparametrization is implemented by directly enhancing the Vertex Morphing mapping to utilize a variable discontinuous kernel for the mapping convolution, which has a filtering effect on

the field. The modified kernel is composed by the original Gaussian kernel of Vertex Morphing and Gaussian kernel placed symmetrically with respect to the user defined symmetry plane. As the kernel shifts over the field during convolution, at any point, the mapping operator averages the shape sensitivity and the shape update field across both sides of the symmetry plane. As the convolution approaches the symmetry plane, the kernel transforms to an overlapping of the two Gaussian functions, fulfilling the field continuity and smoothness criteria.

Finally, the problem of weight reduction and optimal material distribution in sheet metal structures with Vertex Morphing was tackled. Node-based shape optimization, wherein optimization shape updates are normal to the surface, has trouble reducing the mass of a structure to a meaningful order of magnitude. The Vertex Morphing parameterization was extended from 3D to 4D space by introducing nodal thickness design variables in the formulation. At the same time, the geometric constraint of a constant thickness in blanks during production with stamping was dealt with a reparametrization of the thickness design variables by use of an s-shaped function to push optimized values towards the desired binary 0 or 1, indicating material and void respectively, for the thickness of the part. The reparametrization is consistent with the Vertex Morphing mapping and can be viewed as an additional control field for the nodal thickness design variables. Borrowing from the SIMP (Solid Isotropic Material with Penalization) [89] topology optimization approach, the original topology problem is transformed to a geometric one by using thickness instead of density as a design variable. It is a point-wise constraint in the sense that it is applied on all nodes of the design. Shape and thickness sensitivities are obtained from commercial solvers independent to each other. Their maximum norms, which are responsible for the step size of the shape and thickness updates, when left untreated are disproportionate to each other leading to either insignificant shape update or unnaturally large thickness update. A root finding algorithm is used to determine the suitable multiplier for the unfiltered sensitivities such that the desired shape to thickness update ratio is achieved while respecting the gradient projection method [76, 77].

1.4 Outline

This thesis is structured as follows: In chapter 2, the foundation of the current work is laid. First, the mathematical formulation of the general optimization problem, along with explanation of its different aspects, is described. The gradient-based algorithms for constrained and unconstrained optimization that were used are then briefly explained. Finally, the main aspects of shape and topology optimization are presented, which will be useful for the thorough understanding of the the upcoming chapters.

In chapter 3, a reflection symmetry and an undercut constraint are presented. To further understand their implementation and inclusion in shape optimization, 2D test cases are presented therein. Moreover, it deals with the simultaneous shape and topology optimization of shell structures. The coupled 4D mathematical problem is described, where shape and thickness design variables work in synergy, and compared to a staggered approach, where shape and topology optimization act independently on the same geometry.

In chapter 4, large-scale car-body components from different BMW models are optimized with the algorithms from chapter 3.

Finally, conclusions of this work and an outlook are presented in chapter 5.

Chapter 2

Structural optimization foundation

In this chapter, the foundation material needed to understand the framework of this work is presented. As is common practice in most text books or dissertations on structural optimization, the optimization problem and a brief classification of solution algorithms are described in section 2.1. Subsequently, since gradient-based algorithms have been applied in this thesis, the extraction of sensitivities with the most common numerical methods is discussed in section 2.2. Finally, common shape and topology optimization methods are presented in sections 2.3 and 2.4, respectively.

2.1 The optimization problem

2.1.1 Mathematical formulation

In its most general form, the following discretized optimization problem is considered:

$$\begin{aligned} \min_{\boldsymbol{X}} \quad & F(\boldsymbol{X}, \boldsymbol{u}(\boldsymbol{X})) \qquad \boldsymbol{X} \in \mathbb{R}^n, \boldsymbol{u} \in \mathbb{R}^m \\ & h_i(\boldsymbol{X}) = 0 \qquad h_i \in \mathbb{R}, i = 1, ..., p \\ & g_j(\boldsymbol{X}) \leq 0 \qquad g_j \in \mathbb{R}, j = 1, ..., q \\ & r_k(\boldsymbol{X}, \boldsymbol{u}(\boldsymbol{X})) = 0, k = 1, ..., m \end{aligned} \tag{2.1}$$

where F is the objective function and h_i and g_j are the equality and inequality constraints, respectively. $\boldsymbol{X}$ and $\boldsymbol{u}$ are the design variables and state variables, respectively. In node-based shape optimization $\boldsymbol{X}$ is the vector of the discretized mesh nodal coordinates, whereas in density-based topology optimization $\boldsymbol{X}$ denotes the vector of the discretized mesh element or nodal densities. r_k are the residuals of the state governing equations, which act as physical constraints on the problem.

2.1.2 Solution strategies

There exist many ways to classify optimization techniques. Analytic solutions in structural problems are unattainable due to the high number of design variables and the complexity of the state equations describing the problem. Thus, iterative techniques, wherein the optimal solution is approached in several iterations, are favored. Herein, optimization algorithms are classified on the basis of the information they require in this iterative scheme in order to find the next intermediate step:

Zero-order methods Zero-order or direct search methods use only objective and constraint function values to compute the optimal solution. They can be in turn divided into search methods and population-based methods. The former make several trial steps by evaluating the objective function at these points and then choose the best one to proceed to the next step. They typically have good convergence characteristics and low memory requirements but lack generality, in that by changing the initial step size and starting point the optimum and number of iterations

vary. The latter are comprised of evolutionary strategies [13], genetic algorithms [41], and simulated annealing techniques [56]. The selection is based on natural principles of evolution and genetic inheritance notions extrapolated in engineering. An initial population of agents is assigned fitness values that represent their proximity to the optimal solution. After randomly mutating the agents or combining them to create new ones in each iteration, the next generation is chosen by evaluating their fitness values. Evolutionary algorithms are probabilistic methods. Generally, non-gradient methods become inefficient for many design variables since the computational effort scales with them. They are better for non-repeatable stochastic problems.

Gradient-based methods Gradient methods require derivative information of the objective and constraints with respect to the design variables. The derivatives can be of first order (first order methods) or second order (second order methods). They are more appropriate for rich design space problems, when combined with the adjoint method, but can be stuck in local extrema. The most basic gradient method is the steepest descent. The premise of descent methods, for the kth optimization iteration, is that the objective F is guaranteed to improve in every step:

$$F(\boldsymbol{s}^k) < F(\boldsymbol{s}^k + \Delta\boldsymbol{s}^k) \tag{2.2}$$

where

$$\Delta\boldsymbol{s}^k = a^k \boldsymbol{d}^k \tag{2.3}$$

is the design update. $\boldsymbol{d}^k = -\nabla F_{\boldsymbol{s}^k}$ is the objective function negative gradient with respect to the design variables $\boldsymbol{s}$ and a^k the step size, either constant throughout the optimization or derived from a line search. In steepest descent, subsequent search directions are orthogonal to each other:

$$\boldsymbol{s}^k \boldsymbol{s}^{k+1} = 0 \tag{2.4}$$

2.2 Sensitivity Analysis

In the previous section, gradient-based methods for structural optimization were briefly discussed. What remains to be shown is how the gradi-

ent information is computed. That lies within the scope of the sensitivity analysis. It consists of computing the response functions' gradients with respect to the design variables. It highlights how much a system's output varies, subjected to a perturbation in the input.

Accuracy is defined as the difference between the derivatives we obtain and the derivatives obtained by an exact analytic solution. Consistency is the difference between the derivatives we obtain and the exact derivatives of the numerical model. It becomes apparent that there exist two different errors while computing the gradient: a) the error emanating from the inexact approximation of the real life problem through our chosen structural model and b) the error that relates to the differences in exactness between the sensitivity methods applied on that chosen model. The main concern in sensitivity analysis is consistency, since accuracy is a subjective measure. Computational cost and implementation effort are two other criteria for the selection of a sensitivity analysis method.

2.2.1 Direct vs adjoint sensitivities

In this subsection, the two most widespread methods for sensitivity analysis are presented. Discrete derivatives of state variable constraints, also known as analytic methods, are the most consistent and efficient techniques but require knowledge of the state equations and the finite element method. They are derived by differentiating the discretized governing system of equations, denoted by r_k. There are two ways of calculating the discrete analytic sensitivities that differ only in the order of the calculations and are explained in the following paragraph.

Goal of sensitivity analysis is to calculate the gradients of the objective function F with respect to the design variables X_n. Generally, F depends both on the design variables and the physical state variables y_i, e.g. displacement vector u in the case of a structural system:

$$F = F(X_n, u_i) \tag{2.5}$$

The dependency of the governing equations can be written as:

$$r_k(X_n, u_i(X_n)) = 0 \tag{2.6}$$

since the state equations when fed with an independent design variable vector yield a dependent state variable vector.

Using the chain rules to obtain the gradient of F, we get:

$$\frac{dF}{dX_n} = \frac{\partial F}{\partial X_n} + \frac{\partial F}{\partial u_i}\frac{dy_i}{dX_n} \tag{2.7}$$

The total derivative in the right hand side of the equation requires the solution of the governing equations:

$$\frac{dr_k}{dX_n} = \frac{\partial r_k}{\partial X_n} + \frac{\partial r_k}{du_i}\frac{du_i}{dX_n} = 0 \tag{2.8}$$

since the residuals r_k need to be zero, their derivatives with respect to the design variables need to also be zero. By rewriting equation 2.8, it holds:

$$\begin{aligned} &\frac{\partial r_k}{\partial u_i}\frac{du_i}{dX_n} = -\frac{\partial r_k}{\partial X_n} \\ &\quad\mapsto \frac{du_i}{dX_n} = -\left[\frac{\partial r_k}{\partial u_i}\right]^{-1}\frac{\partial r_k}{\partial X_n} \end{aligned} \tag{2.9}$$

and substituting back to 2.7:

$$\frac{dF}{dX_n} = \frac{\partial F}{\partial X_n} - \frac{\partial F}{\partial u_i}\left[\frac{\partial r_k}{\partial u_i}\right]^{-1}\frac{\partial r_k}{\partial X_n} \tag{2.10}$$

In the case of a structural linear system, the discretized governing equations are:

$$r_k = K_{ki}\,u_i - f_k = 0 \tag{2.11}$$

The inverse term in the right hand of equation 2.9, the derivative of the system state equation with respect to the state variables, is nothing but the stiffness matrix $\boldsymbol{K}$. The term $\partial r_k/\partial X_n$ is called the *pseudo-load vector* P^* and is equal to:

$$P^* = \frac{dF_k}{dX_n} - \frac{dK_{ki}}{dX_n}u_i \tag{2.12}$$

Equations 2.9 and 2.10 now become:

$$\frac{d\,u_i}{d\,X_n} = -K^{-1}\overbrace{\left[\frac{d\,f_k}{d\,X_n} - \frac{d\,K_{ki}}{d\,X_n}\,u_i\right]}^{P^*} \tag{2.13}$$

$$\frac{d\,f}{d\,X_n} = \frac{\partial\,f}{\partial\,X_n} - \frac{\partial\,f}{\partial\,u_i}\,K^{-1}\left[\frac{d\,F_k}{d\,X_n} - \frac{d\,K_{ki}}{d\,X_n}\,u_i\right] \tag{2.14}$$

We can now distinguish between two approaches: the direct and the adjoint method for sensitivity calculation.

Direct method In the direct method the derivatives of the state variables with respect to the design variables $d\,u_i/d\,X_n$ are first calculated by using equation 2.9 and then substituted to equation 2.10. The easiest way to grasp the method is by writing down the matrix multiplications and their respective dimensions. The matrix equation has to be solved as many times as the design variables. This can be visualized as solving the linear system with as many loads as the pseudo load vector has columns. The $\boldsymbol{K}$ matrix in this equation represents the governing equation equilibrium in the form of a linear system of equations. Equation 2.13 is shown in matrix notation as:

$$\begin{bmatrix} \frac{du_1}{dX_1} & \frac{du_1}{dX_2} & \cdots & \frac{du_1}{dX_n} \\ \frac{du_2}{dX_1} & \frac{du_2}{dX_2} & \cdots & \frac{du_2}{dX_n} \\ \frac{du_3}{dX_1} & \frac{du_3}{dX_2} & \cdots & \frac{du_3}{dX_n} \\ \vdots & \vdots & \ddots & \vdots \\ \frac{du_m}{dX_1} & \frac{du_m}{dX_2} & \cdots & \frac{du_m}{dX_n} \end{bmatrix} = \begin{bmatrix} K_{11} & K_{12} & K_{13} & \cdots & K_{1m} \\ K_{21} & K_{22} & K_{23} & \cdots & K_{2m} \\ K_{31} & K_{32} & K_{33} & \cdots & K_{3m} \\ \vdots & \vdots & \vdots & \ddots & \vdots \\ K_{m1} & K_{m2} & K_{m3} & \cdots & K_{mm} \end{bmatrix}^{-1} \begin{bmatrix} P^*_{11} & P^*_{12} & \cdots & P^*_{1n} \\ P^*_{21} & P^*_{22} & \cdots & P^*_{2n} \\ P^*_{31} & P^*_{32} & \cdots & P^*_{3n} \\ \vdots & \vdots & \ddots & \vdots \\ P^*_{m1} & P^*_{m2} & \cdots & P^*_{mn} \end{bmatrix}$$

For each column of $d\,u_i/d\,X_n$, the system matrix governing equations have to be solved for the corresponding column load of the pseudo load vector. This results in solving the system for every design variable X_n.

Or, visually:

$$\begin{bmatrix} \frac{du_1}{dX_j} \\ \frac{du_2}{dX_j} \\ \frac{du_3}{dX_j} \\ \vdots \\ \frac{du_m}{dX_j} \end{bmatrix} = \begin{bmatrix} K_{11} & K_{12} & K_{13} & \cdots & K_{1m} \\ K_{21} & K_{22} & K_{23} & \cdots & K_{2m} \\ K_{31} & K_{32} & K_{33} & \cdots & K_{3m} \\ \vdots & \vdots & \vdots & \ddots & \vdots \\ K_{m1} & K_{m2} & K_{m3} & \cdots & K_{mm} \end{bmatrix}^{-1} \begin{bmatrix} P^*_{1j} \\ P^*_{2j} \\ P^*_{3j} \\ \vdots \\ P^*_{mj} \end{bmatrix} \quad \text{for } j = 1, ..., n \tag{2.15}$$

Adjoint method In the adjoint method an auxiliary vector Ψ_k can be acquired by solving the adjoint state problem:

$$\frac{\partial \mathcal{R}_k}{d u_i} \Psi_k = -\frac{\partial f}{\partial u_i} \tag{2.16}$$

or, in the case of a structural system:

$$\begin{aligned} K_{ik} \Psi_k &= -\frac{\partial f}{\partial u_i} \\ \mapsto \Psi_k &= -K_{ik}^{-1} \frac{\partial f}{\partial u_i} \end{aligned} \tag{2.17}$$

In matrix notation, as before, this system is visualized as:

$$\begin{bmatrix} \Psi_{11} & \Psi_{12} & \cdots & \Psi_{1n} \\ \Psi_{21} & \Psi_{22} & \cdots & \Psi_{2n} \\ \Psi_{31} & \Psi_{32} & \cdots & \Psi_{3n} \\ \vdots & \vdots & \ddots & \vdots \\ \Psi_{m1} & \Psi_{m2} & \cdots & \Psi_{mn} \end{bmatrix} = - \begin{bmatrix} K_{11} & K_{12} & K_{13} & \cdots & K_{1m} \\ K_{21} & K_{22} & K_{23} & \cdots & K_{2m} \\ K_{31} & K_{32} & K_{33} & \cdots & K_{3m} \\ \vdots & \vdots & \vdots & \ddots & \vdots \\ K_{m1} & K_{m2} & K_{m3} & \cdots & K_{mm} \end{bmatrix}^{-1} \begin{bmatrix} \frac{df_1}{du_1} & \frac{df_1}{du_2} & \frac{df_1}{du_3} & \cdots & \frac{df_1}{du_m} \\ \frac{df_2}{du_1} & \frac{df_2}{du_2} & \frac{df_2}{du_3} & \cdots & \frac{df_2}{du_m} \\ \vdots & \vdots & \vdots & \ddots & \vdots \\ \frac{df_M}{du_1} & \frac{df_M}{du_2} & \frac{df_M}{du_3} & \cdots & \frac{df_M}{du_m} \end{bmatrix}^T$$

In this case, the system has to be solved for every response function (objectives and constraints). That is, $M = p + q + 1$ times:

$$\begin{bmatrix} \Psi_{1j} \\ \Psi_{2j} \\ \Psi_{3j} \\ \vdots \\ \Psi_{mj} \end{bmatrix} = \begin{bmatrix} K_{11} & K_{12} & K_{13} & \cdots & K_{1m} \\ K_{21} & K_{22} & K_{23} & \cdots & K_{2m} \\ K_{31} & K_{32} & K_{33} & \cdots & K_{3m} \\ \vdots & \vdots & \vdots & \ddots & \vdots \\ K_{m1} & K_{m2} & K_{m3} & \cdots & K_{mm} \end{bmatrix}^{-1} \begin{bmatrix} \frac{df_j}{du_1} \\ \frac{df_j}{du_2} \\ \vdots \\ \frac{df_j}{du_m} \end{bmatrix} \quad \text{for } j = 1, ..., M \tag{2.18}$$

Then, it is substituted back into equation 2.14.

Direct vs Adjoint The sole difference between the direct and the adjoint method is the order of operations which affect the number of back-solving times. In the direct method the problem is tackled by firstly giving an answer to how the design variables, through the pseudo load vector, affect the physical system response. Once du_i/dx_n is calculated it is valid for any response function. On the other hand, in the adjoint method an answer is initially given to how the state variables themselves, through their influence on the response functions, affect the physical system. After the adjoint vector Ψ_k is found, it is the same for all the design variables. The final choice of which method is more appropriate for a sensitivity analysis comes down to the dimensions of the problem. If the design variables number n is greater than the number of responses M then the adjoint method is computationally less demanding. If the number of responses though is larger than the design variable number, then the direct method is faster.

2.3 Shape optimization

Any introduction in the fundamentals of structural optimization should start with definitions: shape optimization can be defined as the modification of domain boundaries to establish the optimal geometric configuration that minimizes an objective function, while design topology remains

rigid. In its continuous form, it is an infinite-dimensional optimization problem since a continuous quantity, i.e., the surface of a body is sought.

As discussed in the previous section, the optimization problem's design variables are iteratively updated to determine the optimal shape. Hence, design variables describe the shape variation and their definition is a core process in shape optimization. The two most widespread shape optimization approaches are the parametric, or CAD-based approach, and the parameter-free, or node-based approach. In the parametric approach design variables are a limited number of geometric parameters such as structural member sizes, radii, distances and other CAD parameters or even polynomial functions, e.g., NURBS [19, 23, 50, 85]. Shape variation is thus limited to the geometric diversity of the initial parameters. On the other hand, in parameter-free techniques geometry representation is through nodal coordinates of the discretized finite element model mesh. Thus, optimization and analysis model is one and the same and no further geometric parametrization is required before optimization. Since every nodal coordinate is updated based on a displacement vector, such methods allow for the richest design space possible. As discussed in section 2.2.1, the development of adjoint sensitivity methods has enabled the application of gradient-based algorithms for large-scale node-based shape optimization problems.

The fundamental challenge in node-based shape optimization is related to the highly non-convex response functions that emerge due to the rich design space and lead to mesh irregularity, mesh dependency and non-smooth shape gradients [28, 49, 58, 64]. A common technique to deal with this, amongst others, is the filtering of shape gradients. Mesh regularization methods are also applied in combination with shape gradient filtering to retain the mesh quality. The next sections presents the Vertex Morphing method, a geometry parametrization technique that tackles the aforementioned shortcomings.

2.3.1 Vertex Morphing

Vertex Morphing is a surface control method for node-based shape optimization [20, 49]. The method introduces a control field for the geometry and an explicit relationship between them in the form of a mapping

operator. The mathematical optimization problem is solved in the control space, which is the space where the control field is defined. The shape update is then obtained after backward mapping of the control field update. Surface smoothness and mesh regularity constraints are satisfied implicitly as a result of the inherent characteristics of the mapping matrix. Different aspects and the most important components of the Vertex Morphing method are described in the following pages.

A volume Ω of a body and its surface Γ are defined. Material points are introduced on Γ, based on the material surface coordinates $\xi = \{\xi_1, \cdots, \xi_{d-1}\} \in \mathbb{R}^d$. For the general case of 3-dimensional geometries $d = 3$. Subsequently, all surface material points can be traced through the spatial position vector field $\boldsymbol{x}(\xi, t) \in \mathbb{R}^d$:

$$\boldsymbol{x}(\xi, t) = \left\{ \begin{array}{c} x_1(s(\xi, t)) \\ x_2(s(\xi, t)) \\ x_3(s(\xi, t)) \end{array} \right\} \tag{2.19}$$

Pseudo time t represents the iterative shape evolution of the geometry during the optimization process.

The proposed control field $s(\xi, t) \in \mathbb{R}^3$ is also dependent on the surface coordinates and controls the geometry through a functional $\mathcal{A}(s, \xi) = x(\xi), \mathcal{A} : \mathbb{R}^3 \rightarrow \mathbb{R}^3$. The mapping between $s(\xi, t)$ and $\boldsymbol{x}(\xi, t)$ is then an explicit kernel-based filter as follows:

$$\begin{aligned} \boldsymbol{x}(\xi_0) &= \mathcal{A}(s, \xi_0) \\ &= \int_\Gamma A(\xi - \xi_0) s(\xi) d\Gamma \end{aligned} \tag{2.20}$$

The nodal coordinates $\boldsymbol{x}$ at point ξ_0 are obtained as a convolution of operator $A(\xi - \xi_0)$ over the control field $s(\xi)$. A is kernel function, most often a linear hat or a Gaussian function. Both filters have a similar qualitative performance; in this work the latter is used:

$$A(\xi - \xi_0) = \frac{1}{r\sqrt{2\pi}} e^{-\frac{\|\xi - \xi_0\|^2}{2r^2}} \tag{2.21}$$

From (2.20) it follows that the derivative of the spatial vector at point ξ_0 with respect to control coordinates at point ξ_1 is:

$$\frac{d\boldsymbol{x}(\xi_0)}{ds(\xi_1)} = A(\xi_1, \xi_0) \tag{2.22}$$

We set aside equation 2.22 for the moment since it will help us later.

We now consider a design objective Φ with a volume density f_Ω for minimization. The optimization takes place in the control space so the objective is a function of the control field:

$$\Phi(s(\xi, t)) = \int_\Omega f_\Omega(s(\xi, t))d\Omega \tag{2.23}$$

or expressed as a surface Γ problem, as is most often the case in shape optimization:

$$\Phi(s(\xi, t)) = \int_\Gamma f_\Gamma(s(\xi, t))d\Omega \tag{2.24}$$

with the surface density f_Γ obtained from volume density f_Ω by integration through the thickness for the example of shell geometries:

$$f_\Gamma = \int_h f_\Omega dn; \qquad \boldsymbol{n}(\xi, t) \in \mathbb{R}^3 \tag{2.25}$$

To solve a continuous problem with numerical analysis it has to be discretized. In most problems solving for the continuum fields analytically is impossible. Discretization of the geometry sets up the problem for a numerical analysis. Therefore, the geometry field $x(\xi)$ is discretized into finite parts with shape functions R_j and the vector of nodal coordinates $\boldsymbol{X} = \left[x_1, x_2, ..., x_n\right]$ with $\boldsymbol{X} \in \mathbb{R}^n$:

$$\boldsymbol{x}(\xi) \approx \boldsymbol{x}_h(\xi) = \sum_i R_i(\xi)X_i \tag{2.26}$$

Similarly, to discretize the design control field $s(\xi)$ we assume s_j control points and N_j shape functions:

$$s(\xi, t) \approx s_h(\xi) = N(\xi)_j s_j(t) \tag{2.27}$$

and equation 2.20 transforms to

$$\boldsymbol{x}_h(\xi_0) = \int_\Gamma A(\xi - \xi_0) N_j(\xi) s_j \, d\Gamma \tag{2.28}$$

Control points s_j are independent of the integral and can be taken out of it:

$$\boldsymbol{x}_h(\xi_0) = \int_\Gamma A(\xi - \xi_0) N_j(\xi) d\Gamma s_j = B_j(\xi_0) s_j \tag{2.29}$$

where B_j are the morphing functions. If A and N_j are chosen to be polynomial functions of degree p and q respectively, B_j is of degree $(p+q+1)$ [20]. The design control field then resembles a CAD parametrization function, e.g. NURBS. s_j are equivalent to the control points and B_j equivalent to the shape functions of the CAD function [21, 49]. Using the same grids s_i, X_j and shape function N_i, R_j for the discretization of geometry $\boldsymbol{x}(\xi)$ and control field $s(\xi)$ offers an important advantage: the same meshed design can be used for the control and the geometric quantities. Thus, one needs to choose only the filter radius to guide the optimization towards a desired shape, which works as a spatial low-pass filter and eliminates wavelengths smaller than the input radius [49]. In this case, the Vertex Morphing mapping is a square matrix $\boldsymbol{A}$ and represents simply a re-parametrization of the design variables $\boldsymbol{X}$ into $\boldsymbol{s}$ without any dimensionality reduction.

As discussed in chapter 1, adjoint methods yield gradient information of the design objective $\Phi(s(\xi))$ with respect to the design variables at almost the same computational cost as the primal solution of the problem. Thus, in node-based optimization gradient-based methods are used for the solution of the problem. It has become clear now that the optimization design variables are the control points s_j of the geometrical coordinates X_j. The update rule for the new design according to the steepest descent described in section 2.1.2 is as follows:

$$\begin{aligned} \boldsymbol{s}^{k+1} &= \boldsymbol{s}^k + \Delta \boldsymbol{s}^k \\ &= \boldsymbol{s}^k - a^k \frac{d f_\Gamma}{d \boldsymbol{s}^k} \end{aligned} \tag{2.30}$$

We denote with F the approximation of the design objective Φ after discretization of the control field $s(\xi)$ with s_h. The variation $\delta\Phi$ due to

an infinitesimal variation of the geometry $\delta \boldsymbol{x}$ at the surface Γ is:

$$\delta \Phi = \int_\Gamma \frac{df_\Gamma}{d\boldsymbol{x}} \delta \boldsymbol{x} \, d\Gamma \tag{2.31}$$

and is approximated by δF in the control space:

$$\delta \Phi(s) \approx \delta F(s_h) = \frac{dF}{ds_i} \delta s_i = \int_\Gamma \frac{df_\Gamma}{ds} N_i \delta s_i \, d\Gamma \tag{2.32}$$

The design gradient at position ξ_1 is then:

$$\begin{aligned} \frac{df_\Gamma}{ds}(\xi_1) &= \int_\Gamma \frac{df_\Gamma}{d\boldsymbol{x}} \frac{d\boldsymbol{x}}{ds(\xi_1)} d\Gamma \\ &= \int_\Gamma \frac{df_\Gamma}{d\boldsymbol{x}} A(\xi_1 - \xi) d\Gamma \\ &= \int_\Gamma A_{adj}(\xi_1 - \xi) \frac{df_\Gamma}{d\boldsymbol{x}} d\Gamma \end{aligned} \tag{2.33}$$

for rectangular matrices the adjoint matrix is equal to the transpose. The shape gradient field $\frac{df_\Gamma}{d\boldsymbol{x}}$ needs to be also discretized. By applying the geometry discretization of equation (2.26) it yields:

$$\frac{df_\Gamma}{d\boldsymbol{x}_h} \approx \sum_i R_i(\xi) \frac{df_\Gamma}{d\boldsymbol{X}_i} \tag{2.34}$$

$\frac{df_\Gamma}{d\boldsymbol{X}_i}$ is calculated locally for every nodal coordinate by a sensitivity analysis from a solver.

The discrete design derivative of F with respect to control point s_i is then as follows:

$$\begin{aligned} \frac{dF}{ds_i} &= \int_\Gamma \frac{df_\Gamma}{ds} \frac{ds}{ds_i} d\Gamma \\ &= \int_\Gamma \left(\int_\Gamma \frac{df_\Gamma}{dx} A \, d\Gamma \right) N_i \, d\Gamma \end{aligned} \tag{2.35}$$

Finally, the control field $s(\xi)$ is updated, as equation (2.30) shows, in the direction of the negative gradient $\frac{df_\Gamma}{ds}$:

$$\Delta s = -\frac{df_\Gamma}{d\boldsymbol{x}} \frac{d\boldsymbol{x}}{ds} = -\int_\Gamma A^T \frac{df_\Gamma}{d\boldsymbol{x}} d\Gamma \tag{2.36}$$

Finally, in order to update the original geometry $\boldsymbol{x}$, the forward filter operation is applied:

$$\Delta \boldsymbol{x} = \int_\Gamma A \Delta s \, d\Gamma = -\int_\Gamma \int_\Gamma A A^T \frac{d f_\Gamma}{d \boldsymbol{x}} d\Gamma \, d\Gamma \tag{2.37}$$

An important advantage of Vertex Morphing is that the control field s does not have to be calculated at every iteration of the optimization. In the next section constrained optimization with Vertex Morphing will be discussed.

2.3.2 Constrained optimization in the control space

Most engineering optimization problems in the automotive industry are constrained, in that a series of physical, geometric or manufacturing constraints have to be fulfilled. In this context, Rosen's gradient projection algorithm [76, 77] is utilized, which can be seen as an extension of the gradient descent method for constrained optimization problems. The premise of the algorithm is that by projecting the search direction into the subspace tangent to the active constraints and moving with a small step size length, the design will respect the constraints. After every projection an appropriate correction is applied to ensure that the constraint is not violated. The method is briefly described in the following paragraphs with the use of matrix and vector notation for the discretized problem, since it is the basis for the industrial constraints described in chapter 3.

In the case of linearly constrained shape optimization with Vertex Morphing in the control space, the general optimization problem of equation 2.1 can be expressed as:

$$\begin{aligned} \min_{\boldsymbol{s}} \quad & F(\boldsymbol{s}) \\ s.t. \quad & g_j(\boldsymbol{s}) = \sum_{i=1}^{n} a_{ji} s_i - b_j \leq 0, \qquad j = 1, ..., n_g \end{aligned} \tag{2.38}$$

which can be written in vector form as

$$g_j = \boldsymbol{a}_j^T \boldsymbol{s} - b_j \leq 0 \tag{2.39}$$

At every optimization iteration, relevant to the mathematical problem is only the vector of active constraints $\boldsymbol{g}_a$

$$\boldsymbol{g}_a = \boldsymbol{C}_m^T \boldsymbol{s} - \boldsymbol{b} = 0 \tag{2.40}$$

where $\boldsymbol{C}_m$ is a matrix whose columns are the sensitivities of the active constraints in the control space. To obtain $\boldsymbol{C}_m$, the sensitivities of the active constraints in the geometry space $\boldsymbol{C}$ have to be mapped to the control space using matrix $\boldsymbol{A}$:

$$\boldsymbol{C}_m = \frac{d\,\boldsymbol{g}_a}{d\,\boldsymbol{x}} \frac{d\,\boldsymbol{x}}{d\,\boldsymbol{s}} = \boldsymbol{C}\boldsymbol{A} \tag{2.41}$$

Using the common update rule of gradient methods:

$$\boldsymbol{s}^{k+1} = \boldsymbol{s}^k + \alpha \boldsymbol{p} \tag{2.42}$$

if both $\boldsymbol{s}^{k+1}$ and $\boldsymbol{s}^k$ satisfy equation 2.40, the search direction $\boldsymbol{p}$ must lie in the subspace tangent to the active constraints:

$$\boldsymbol{C}_m^T \boldsymbol{p} = 0 \tag{2.43}$$

and the optimization problem of equation 2.38 is transformed to the following one:

$$\begin{aligned} \min_{\boldsymbol{p}} \quad & \boldsymbol{p}^T \nabla F \\ s.t. \quad & \boldsymbol{C}_m^T \boldsymbol{p} = 0 \\ and \quad & \boldsymbol{p}^T \boldsymbol{p} = 1 \end{aligned} \tag{2.44}$$

which can be interpreted as finding the direction $\boldsymbol{p}$ which is the closest to the unconstrained search direction ∇F, while it is also perpendicular to all the active constraint gradients in order not to violate them.

Forming the Lagrangian we get:

$$\mathcal{L}(\boldsymbol{p}, \lambda, \mu) = \boldsymbol{p}^T \nabla F - \boldsymbol{p}^T \boldsymbol{C}_m \lambda - \mu\left(\boldsymbol{p}^T \boldsymbol{p} - 1\right) \tag{2.45}$$

where $\boldsymbol{\lambda}$ and $\boldsymbol{\mu}$ are the Lagrange multipliers of the constraints. $\mathcal{L}$ is stationary when the Karush-Kuhn-Tucher (KKT) conditions are satisfied:

$$\begin{aligned}\frac{\partial \mathcal{L}}{\partial \boldsymbol{p}} &= \nabla F - \boldsymbol{C}_m \boldsymbol{\lambda} - 2\mu \boldsymbol{p} = 0 \\ \frac{\partial \mathcal{L}}{\partial \boldsymbol{\lambda}} &= \boldsymbol{C}_m \boldsymbol{p} = 0 \\ \frac{\partial \mathcal{L}}{\partial \mu} &= \boldsymbol{p}^T \boldsymbol{p} - 1 = 0\end{aligned} \tag{2.46}$$

From the solution of this system of equations, we obtain the Lagrange multiplies as:

$$\boldsymbol{\lambda} = \left(\boldsymbol{C}_m^T \boldsymbol{C}_m\right)^{-1} \boldsymbol{C}_m^T \nabla F \tag{2.47}$$

and by replacing $\boldsymbol{\lambda}$ in equation 2.45, the direction $\boldsymbol{p}$ is calculated as

$$\boldsymbol{p} = \frac{1}{2\mu}\left[\boldsymbol{I} - \boldsymbol{C}_m \left(\boldsymbol{C}_m^T \boldsymbol{C}_m\right)^{-1} \boldsymbol{C}_m^T\right] \nabla F = \frac{1}{2\mu} \boldsymbol{P} \nabla F \tag{2.48}$$

where $\boldsymbol{P}$ is the projection matrix and the factor $\frac{1}{2\mu}$ is to be neglected since it is irrelevant to the search direction $\boldsymbol{p}$.

Due to the high non-linearity of the constraint functions, search direction $\boldsymbol{p}$ is corrected in the direction of the constraint gradient multiplied by a factor β and the constraint value $\boldsymbol{g}_a$:

$$\tilde{\boldsymbol{p}} = \boldsymbol{p} - \beta \boldsymbol{C}_m \left(\boldsymbol{C}_m^T \boldsymbol{C}_m\right)^{-1} \boldsymbol{g}_a(\boldsymbol{s}) \tag{2.49}$$

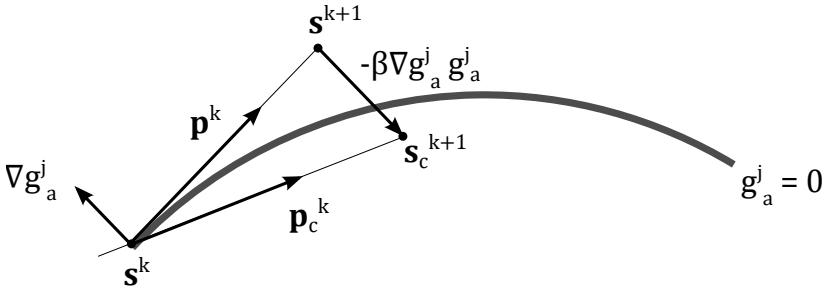

Figure 2.1 : Gradient projection.

2.4 Topology optimization

Topology optimization offers maximal design flexibility in that the optimal material distribution in a given boundary is sought. Essentially, the problem is the following: find the material distribution in a given boundary that minimizes/ maximizes an objective function F, subject to a volume constraint $G_0 \leq 0$ and, often, N other constraints $G_i \leq 0$, $i = 1...N$. In structural optimization, the state equations of the mathematical problem can be formulated as additional constraints. The material distribution is expressed by a density function $\rho(\boldsymbol{x})$. Nodal or element densities should be either 0-void or 1-material.

The general optimization problem of equation 2.1 for the case of topology optimization is transformed to:

$$\begin{aligned} \min_{\rho} \quad & F(\boldsymbol{u}(\rho),\rho) = \int_{\Omega} f(\boldsymbol{u}(\rho),\rho)\,dV \\ & G_0(\rho) = \int_{\Omega} \rho(x)\,dV - V_0 \leq 0 \\ & G_i(\boldsymbol{u}(\rho),\rho) \leq 0, \qquad i = 1...j \\ & \rho(\boldsymbol{x}) = 0 \quad or \quad 1, \qquad \forall \boldsymbol{x} \in \Omega \end{aligned} \tag{2.50}$$

It is well-known, that this continuous form of the so-called $0-1$ problem is ill-posed and lacks solutions. By introducing new holes while keeping the volume constant a structure becomes stiffer. This means a lack of closedness for the set of admissible solutions [4, 57, 89, 91]. Typically,

in numerical topology optimization the general continuous problems is discretized by division of domain Ω in n finite elements and assigning a density value on each of them as a design variable. Since it is finite-dimensional, it generally has solutions. Then, the problem becomes:

$$\begin{aligned} \min_{\boldsymbol{\rho}} \quad & F(\boldsymbol{u}(\boldsymbol{\rho}),\boldsymbol{\rho}) = \sum_i \int_{\Omega_i} f(\boldsymbol{u}(\rho_i),\rho_i) dV \\ & G_0(\boldsymbol{\rho}) = \sum_i V_i \rho_i - V_0 \leq 0 \\ & G_i(\boldsymbol{u}(\boldsymbol{\rho}),\boldsymbol{\rho}) \leq 0, \qquad i = 1...j \\ & \rho_i = 0 \quad or \quad 1, \qquad \rho_i = 1...n \end{aligned} \tag{2.51}$$

However, in its discretized form, the nonexistence of solutions of the continuous problem is manifested in the form of mesh-dependency, where for larger n more holes develop, and numerical instabilities, i.e. checkerboard problems [30, 42]. Existence of solutions can be achieved by either restricting or relaxing the solution space. In the former case, ways to restrict the admissible designs are through perimeter control, global or local slope constraints and design sensitivity filtering [89]. In the latter case, enlargement of the admissible designs was proposed with the homogenization approach to topology optimization [17] by introducing a microscale.

Since the seminal work of Bendsøe and Kikuchi, various concepts have been proposed, i.e., the density approach [16, 99], the level set approach [3, 7, 93], discrete and evolutionary approaches [15, 97], topological derivatives [37, 90] and several others. In the next section a density-based approach will be briefly presented.

2.4.1 Density approach

The design variables of the discretized problem of equation 2.51 can only take the discrete values 0 or 1. An efficient way to solve such discrete problems is by allowing continuous design variables with values between 0 and 1 and using gradient-based optimization methods to solve the problem. The SIMP or power-law approach [16, 63, 99] is a material interpolation scheme where the stiffness tensor of a density material is

given by:

$$\boldsymbol{C}_{ijkl}(\rho) = \boldsymbol{C}^0_{ijkl}\rho^p \tag{2.52}$$

where $\boldsymbol{C}^0_{ijkl}$ is the stiffness tensor of the solid material and p is the penalization parameter which forces the continuous design variables towards 0 or 1. For $p > 1$, local stiffness of elements with $\rho < 1$ decreases, thus making it more costly to retain intermediate thicknesses since mass is a linear function of density but stiffness a sublinear one. For $p = 1$ the formulation yields the variable thickness sheet problem. A widely accepted number for p that offers convergence to $0-1$ solutions is $p = 3$.

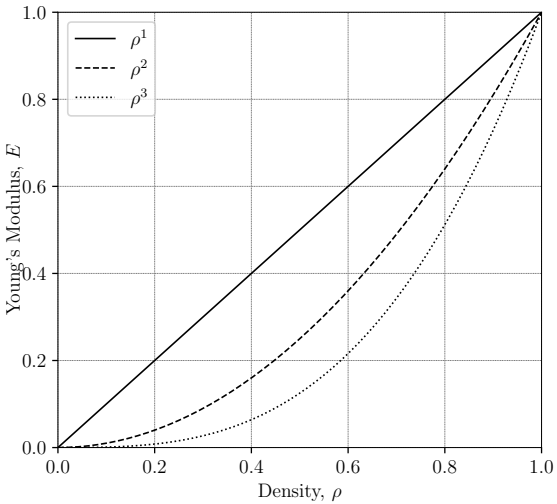

Figure 2.2 : SIMP model for $p = 1$, $p = 2$ and $p = 3$.

Chapter 3

Industrial constraints for admissible shapes

Unconstrained gradient-based shape optimization has proven its efficacy in finding optimal designs. In practice, geometry adjustments take place a posteriori by the engineer to ensure compliance with manufacturing and geometric constraints. Naturally, modifying the optimal design cedes some of the optimality that was gained through the optimization. By introducing these industrial limitations in the formulation of the optimization problem, no manual adjustments are required and the optimality is only slightly compromised.

The purpose of this chapter is to propose different approaches to include industrial constraints in the optimization problem. The most direct way is by adding a range of point-wise constraint functions. As will be seen below, the desired effect on the optimal design can be achieved by modifying other elements of the optimization formulation.

In the following sections, three constraint inclusion methods are described: (a) a novel aggregation formulation for an undercut-prevention constraint, (b) an enhancement of the Vertex Morphing parametrization for reflection-symmetry constraint and (c) the dimensional extension of the Vertex Morphing formulation along with a nonlinear reparametrization of a set of design variables for volume-constrained shape optimization of surface geometries with a constant thickness constraint.

3.1 Aggregation and reduction of point-wise constraints

Two very common manufacturing processes in the automotive industry are deep drawing, for sheet metal, and casting, for solid components. Both processes subject the optimal design to a set of geometric restrictions that influence the design concept to ensure manufacturability of the geometry. A common limitation is the prevention of undercut regions in the optimal shape. In casting, undercut features prevent the ejection of the part from the molds whereas in deep drawing, undercut features in the stamping direction are not realizable.

Point-wise constraints formulations lead to a very high number of active constraints and thus a disproportionate increase in the computational cost. To counterbalance this disadvantage, constraint aggregation methods have been introduced in various publication [52, 54, 74]. The most common aggregation approaches are the p-norm and Kreisselmaier-Steinhausser functionals, with different draw-down factors ρ, or considering only the most violated constraint.

3.1.1 Ray tracing for volume calculation

In this section, a different aggregation approach for the undercut formation problem is followed. The idea is to convert the local point-wise constraint formulation into a global problem of volume minimization, sensitivity for which can be easily calculated. The new function is defined as the “trapped” volume in the undercut regions and added as an equality constraint to the optimization problem $g_U = 0$. Figure 3.1 illustrates an undercut region in a solid body with area V_U (in 2D volume

naturally becomes area). The area is calculated as an integral of the differentiable surface function $f(x_1)$ along the infeasible region depicted with red nodes:

$$g_U(\boldsymbol{X}) = V_U = \int_D f(x_1) d\, x_1 = 0 \tag{3.1}$$

On a view plane normal to the demolding or deep drawing direction all surfaces should be visible for a feasible geometry without undercuts. Infeasible regions are defined as those that are invisible and those that are covering other regions. A ray tracing technique is employed to detect the infeasible nodes. For every geometry point i a ray is shot towards the deep drawing direction:

$$\boldsymbol{r}_i = \boldsymbol{X}_i + \alpha \boldsymbol{d} \tag{3.2}$$

and checked for intersections with the geometry elements. Every point on the plane of j-th triangular element with nodes A, B and C can be written in the form:

$$\boldsymbol{A} + \beta(\boldsymbol{B} - \boldsymbol{A}) + \gamma(\boldsymbol{C} - \boldsymbol{A}) \tag{3.3}$$

for some numbers β and γ. If the point is also on the ray, then it is also equal to:

$$\boldsymbol{X}_i + \alpha \boldsymbol{d} \tag{3.4}$$

for some number α. Setting equations equal we obtain the following linear system:

$$\begin{aligned} \boldsymbol{X}_i + \alpha \boldsymbol{d} &= \boldsymbol{A} + (\boldsymbol{B} - \boldsymbol{A})\beta + (\boldsymbol{C} - \boldsymbol{A})\gamma \\ \beta(\boldsymbol{A} - \boldsymbol{B}) + \gamma(\boldsymbol{A} - \boldsymbol{C}) + \alpha \boldsymbol{d} &= \boldsymbol{A} - \boldsymbol{X}_i \\ \begin{bmatrix} x_A - x_B & x_A - x_C & x_d \\ y_A - y_B & y_A - y_C & y_d \\ z_A - z_B & z_A - z_C & z_d \end{bmatrix} \begin{bmatrix} \beta \\ \gamma \\ \alpha \end{bmatrix} &= \begin{bmatrix} x_A - x_i \\ y_A - y_i \\ z_A - z_i \end{bmatrix} \end{aligned} \tag{3.5}$$

which can be solved with multiple ways. If $0 < \beta < 1$, $0 < \gamma < 1$ and $0 < 1 - \beta - \gamma < 1$, then the ray intersects the triangle and α is the distance between $\boldsymbol{X}_i$ and intersection point.

Naturally, checking for intersections with every element would be computationally ineffective. This cost can be reduced by utilizing a fixed-radius near neighbors search on the nodes after projecting them into the tangent plane normal to the deep drawing direction. This is equivalent to using a cylinder with an axis passing through the ray r_i instead of a sphere for the search. The concept is depicted in figure 3.1.

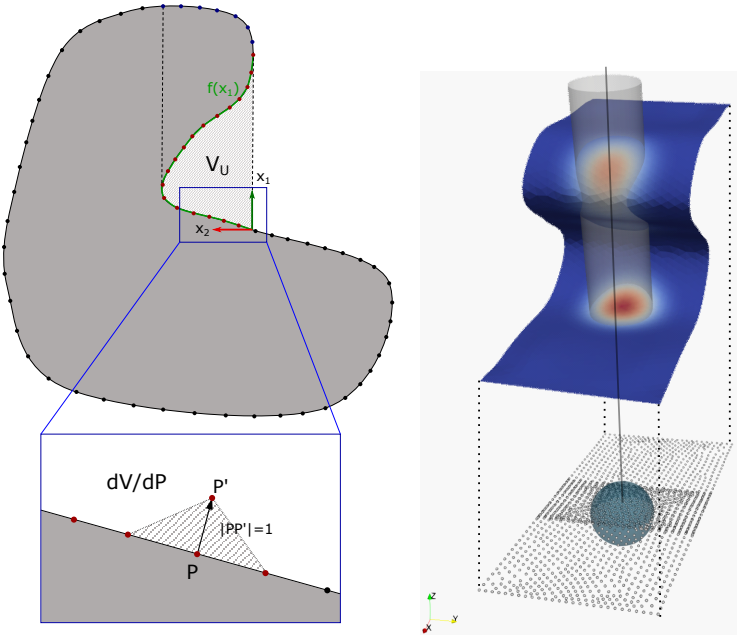

Figure 3.1 : A schematic representation of the undercut formation problem. Left: definition of undercut volume to be minimized and shape gradient calculation. Right: Fixed-radius node search in cylinder for calculation of infeasible nodes.

In the 3D case, the boundary that is formed by axis x_1 in the 2D case becomes a surface and is harder to analytically define. For discrete geometries, the volume integral is calculated as a sum over the infeasible domain nodal values by utilizing again the ray tracing algorithm:

$$g_U = \sum_{i=1}^{n_n} N_i \alpha_i \tag{3.6}$$

where N_i the area of influence and α_i the distance to the first collision in the deep drawing direction of i-th node.

3.1.2 Derivation of constraint function sensitivities

The gradient of the undercut volume function with respect to the nodal coordinates is calculated, for every node, as the geometry volume change after a unit displacement of the node in the normal-to-surface direction. Simplifying the calculation, sensitivity is equal to the volume of the tetrahedral elements formed by the adjacent to node triangular elements and the perturbed node, as illustrated in figure 3.2.

$$\begin{aligned}\frac{dg_U}{d\boldsymbol{X}_i} &= \frac{g_U(\boldsymbol{X}_i')-g_U(\boldsymbol{X}_i)}{\|\boldsymbol{X}_i'-\boldsymbol{X}_i\|_2} \\ &= \sum_{j=1}^{n_e}\frac{1}{3}A_j h_j \\ &= \sum_{j=1}^{n_e}\frac{1}{3}A_j\|\boldsymbol{X}_i'-\boldsymbol{X}_i\|_2\end{aligned} \tag{3.7}$$

where the base area A_j of j-th element can be calculated easily based on the coordinates of its nodes $\boldsymbol{X}_i$, $\boldsymbol{X}_{i-1}$ and $\boldsymbol{X}_{i+1}$ as

$$A_j = \|(\boldsymbol{X}_i-\boldsymbol{X}_{i-1})\times(\boldsymbol{X}_{i+1}-\boldsymbol{X}_{i-1})\|_2 \tag{3.8}$$

and the height H_j of j-th element equal to the norm of difference between the perturbed $\boldsymbol{X}_i'$ and the original $\boldsymbol{X}_i$ node. In the case of non-triangular meshes, the volume calculation can either be generalized for polyhedra or the surface mesh can be triangulated beforehand.

The sensitivity direction is decided based on the normal curvature κ_n at every node, which is the curvature projected onto the plane containing the normal unit vector and the projected onto the tangent plane deep drawing vector $\boldsymbol{d}'$. The deep drawing direction is projected into the tangent plane to the surface unit normal $\boldsymbol{n}$:

$$\boldsymbol{d}' = (\boldsymbol{I}-\frac{\boldsymbol{n}\boldsymbol{n}^T}{\|\boldsymbol{n}\|_2^2})\boldsymbol{d} \tag{3.9}$$

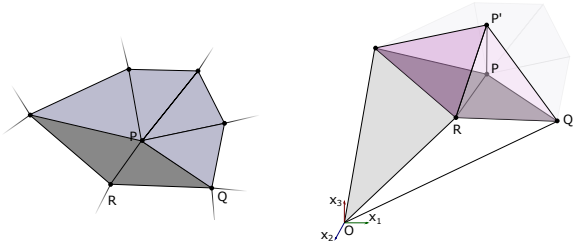

Figure 3.2 : Undercut constraint shape gradient calculation based on finite-difference method. Left: neighboring elements of node. Right: Perturbed node and neighboring elements.

Figure 3.3 shows the surface tangent plane in light blue and the plane that contains the surface normal $\boldsymbol{n}$ and the the projected drawing direction $\boldsymbol{d}'$ in light green. κ_n is then calculated as:

$$\kappa_n = \kappa_1 \cos^2\theta + \kappa_2 \sin^2\theta \tag{3.10}$$

where κ_1 and κ_2 are the principal curvature values at every geometry point, represented by the red lines in figure 3.3. They measure the maximum and minimum that a surface bends in different directions, the principal curvature directions $\boldsymbol{t}_1$ and $\boldsymbol{t}_2$. θ is the angle between the direction $\boldsymbol{d}'$ in which the normal curvature is calculated and the principal direction $\boldsymbol{t}_1$:

$$\frac{\boldsymbol{d}'}{\|\boldsymbol{d}'\|_2} = \cos\theta\,\boldsymbol{t}_1 + \sin\theta\,\boldsymbol{t}_2 \tag{3.11}$$

Principal curvatures are defined on differentiable surfaces so for their calculation on discretized geometries a quadric fitting approach is utilized [71]. At every node and its neighboring elements, a best-fit quadric surface is defined and principal curvature values and directions are analytically computed. For their efficient computation, an external computational geometry library was used, libigl[51].

The idea is, that every infeasible node should move towards the feasible domain, where it does not “hide” the nodes below it and is not “hidden” from other nodes. For outwards pointing surface normal vectors, a

positive normal curvature means the constraint sensitivity is pointing in the direction which maximizes the normal curvature, whereas at a negative curvature, it is pointing in the direction which minimizes it. In this way, the sensitivities ensure that all undercuts will be minimized, and in their place, optimal surfaces will be "neutral", with surface normal perpendicular to the deep drawing direction and a curvature as close to zero as possible.

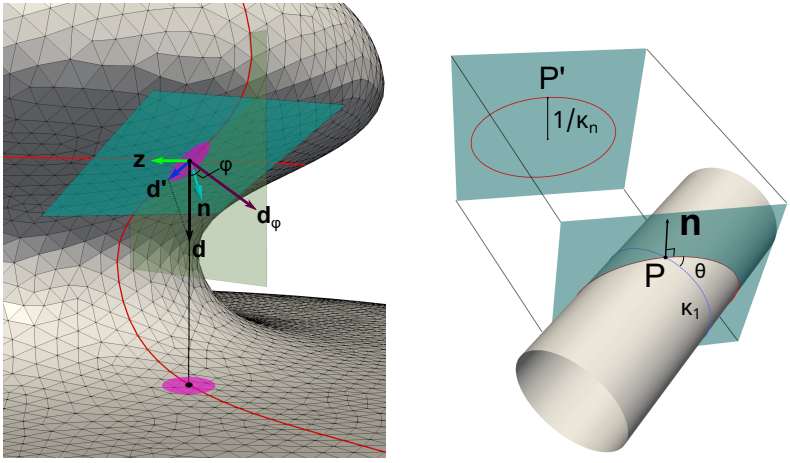

Figure 3.3 : Curvature calculation for undercut constraint. Left: Ray tracing direction for an infeasible node during undercut response function calculation. Right: Normal curvature in tangent plane slicing a cylinder.

The simple shape optimization example of figure 3.4 illustrates the concept of the constraint. The initial geometry comprises of infeasible domains with undercuts and the undercut constraint is set as the objective function. For the optimization, the steepest descent algorithm with a constant step size was utilized. The Vertex Morphing filter radius r was chosen as large as five times the minimum element size. The deep drawing direction $\boldsymbol{d}$ is co-linear to the negative z direction. As expected, after a few optimization iterations the undercuts are eliminated and the regions at around $y = \pm 0.4$ become vertical and flat with minimal curvature.

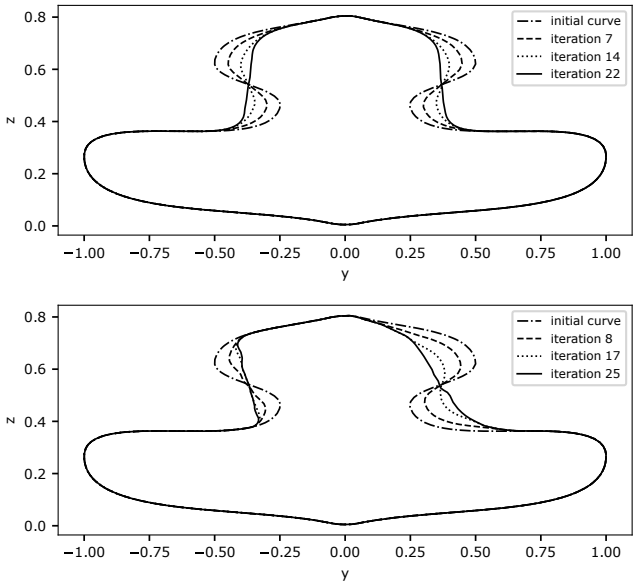

Figure 3.4 : 2D example of node-based shape optimization with Vertex Morphing under an undercut constraint. Top: Mold removing direction equal to $-z$. Bottom: Mold removing direction rotated 20° around x direction.

3.1.3 Conical surface buffer zone

In many cases, due to mechanical limitations of the manufacturing processes, all sloped regions of a geometry have to fulfill an angle limit, either positive or negative. For example, overhang features of additively manufactured components should rise at the building direction at a “shallow” angle to avoid support material. This angle, above which support material is not needed, is the self-supporting angle. Another example is the contact angle of the blank and the forming tools during a deep drawing process. When the contact angle is too large and the surfaces are almost parallel to the deep drawing direction, there is a high risk of excessive thinning and, eventually, cracking. This can be avoided by “softening” this angle.

A simple change of the input deep drawing direction would not eliminate the problem in symmetric geometries since the optimal design would contain both underhang features and sloped surfaces, as illustrated in figure 3.4 where the deep drawing direction has been rotated around the x axis by 20°. Technically, the design has no undercut regions in the deep drawing direction but it still is not acceptable.

To avoid this problem, a imaginary cone-shaped buffer zone with an axis coinciding with the deep drawing direction is defined, on which the ray tracing directions of every node are projected. The angle ϕ to the axis can be either negative, in which case overhang features can be formed, or positive, in which case inclined surfaces are allowed. In this way, the optimization of the 3D geometry is implicitly broken down to a number of sub-optimizations of cutting plane sections which contain every infeasible node, its unit normal vector and the deep drawing direction. The ray direction is rotated by the angle ϕ in this plane. The rotation axis for the ray of i-th node can be retrieved as:

$$\boldsymbol{z} = \boldsymbol{n} \times \frac{\boldsymbol{d}'}{\|\boldsymbol{d}'\|_2} = \boldsymbol{n} \times \tilde{\boldsymbol{d}}' \tag{3.12}$$

so that $\boldsymbol{z}$, $\boldsymbol{n}$ and $\tilde{\boldsymbol{d}}'$ form an orthonormal basis. As mentioned above, normal curvature κ_n at node i is calculated in the direction of $\boldsymbol{d}'$. The above basis is reminiscent of the *Darboux frame* [33], a concept in differential geometry which is a natural moving frame constructed on a all non-umbilical points of a surface.

Finally, the general formula for a rotation matrix by angle ϕ about the unit vector $\boldsymbol{z}$ is as follows:

$$R_{ij}(z,\phi) = \cos\phi\,\delta_{ij} + (1-\cos\phi) z_i z_j - \sin\phi\,\epsilon_{ijk} z_k \tag{3.13}$$

where δ_{ij} the Kronecker delta and ϵ_{ijk} the Levi-Civita symbol:

$$\delta_{ij} = \begin{cases} 0, & \text{if} i \neq j, \\ 1, & \text{if} i = j. \end{cases} \tag{3.14}$$

$$\epsilon_{ijk} = \begin{cases} +1, & \text{if } (i,j,k) \text{ is an even permutation of} (1,2,3), \\ -1, & \text{if } (i,j,k) \text{ is an odd permutation of} (1,2,3), \\ 0, & \text{if there is a repeated index.} \end{cases} \quad (3.15)$$

Using equation 3.13, matrix $\boldsymbol{R}(z,\phi)$ can be written explicitly:

$$\boldsymbol{R}(\boldsymbol{z},\phi) = \begin{bmatrix} \cos\phi + z_1^2(1-\cos\phi) & z_1 z_2(1-\cos\phi) - z_3\sin\phi & z_1 z_3(1-\cos\phi) - z_2\sin\phi \\ z_1 z_2(1-\cos\phi) - z_3\sin\phi & \cos\phi + z_2^2(1-\cos\phi) & z_2 z_3(1-\cos\phi) - z_1\sin\phi \\ z_1 z_3(1-\cos\phi) - z_2\sin\phi & z_2 z_3(1-\cos\phi) - z_1\sin\phi & \cos\phi + z_3^2(1-\cos\phi) \end{bmatrix} \quad (3.16)$$

and the rotated ray direction is naturally,

$$\boldsymbol{d}_\phi = \boldsymbol{R}\,\boldsymbol{d} \quad (3.17)$$

The shape optimization example of figure 3.4 is re-run using the buffer zone formulation, once with a negative angle $\phi = -20°$ and once for a positive angle $\phi = 20°$. Step size and filter radius was kept constant as for the original example. Convergence is achieved after a different number of iterations based on how deep in the infeasible domain the initial geometry is.

Algorithm 3.1 outlines the steps needed for a constrained shape optimization with Vertex Morphing parametrization under an undercut constraint.

3.1.4 Limitations of weakly enforced constraints

There is an interesting limitation of our aggregate undercut constraint formulation. In Vertex Morphing, as discussed in chapter 2.3.1, the filter radius of the linear mapping acts as a low-pass filter of geometric wavelengths. Undercuts with a size smaller than the filter radius can therefore not be easily resolved and might lead to oscillatory optimization iterations around the features. This particularity holds for any weakly enforced aggregate constraint. A similar phenomenon can be observed

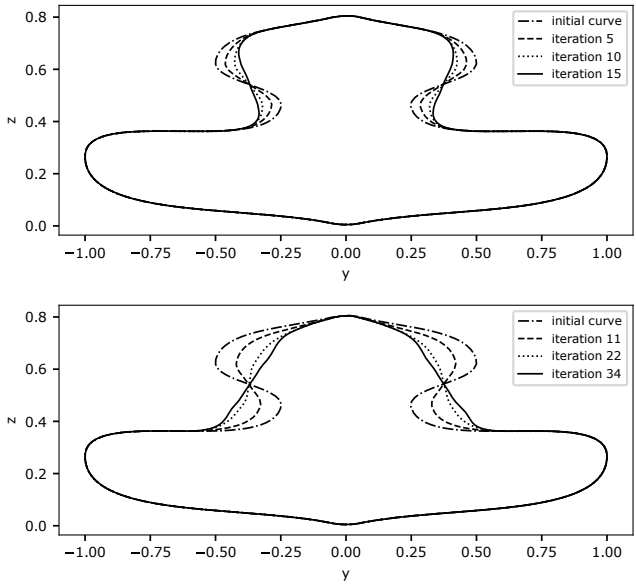

Figure 3.5 : 2D example of node-based shape optimization with Vertex Morphing under an undercut constraint. Mold removing direction equal to $-z$ and application of a negative angle (top) and a positive angle (bottom) for the conical buffer zone.

in density-based SIMP topology optimization, where the length of the grey scale transition between solid and void regions is dependent on the applied density or sensitivity filtering.

The effect of the filter radius size is illustrated in figure 3.6. The simple example of figure 3.4 was optimized with a filter radius of 50 mm and was optimized again for three different filter radii, 100 mm, 150 mm and 200 mm. As can be seen, the optimizations with the two largest filter radii do not fully resolve the undercuts. Possible solutions are the mesh refinement around the undercut regions and the selection of a smaller filter radius.

Algorithm 3.1: Vertex Morphing parametrization with an undercut constraint.

initialize geometry $\boldsymbol{X}^0$
for *optimization loop* $k = 1, 2, 3..., k$ **do**
  solve state problem
  $r(\boldsymbol{X}^k, \boldsymbol{u}^k(\boldsymbol{X}^k)) = 0$
  solve adjoint problem
  $\frac{df_r}{d\boldsymbol{X}^k}$
  begin initialize undercut constraint
    Compute unit normal vectors of nodes $\rightarrow \boldsymbol{n}_i$
    Compute surface influence domains of nodes $\rightarrow \boldsymbol{A}$
    Compute principal curvatures $\rightarrow \kappa_1, \kappa_2$
    Compute Gaussian curvatures $\rightarrow K = \kappa_1 \odot \kappa_2$
    Compute normal curvatures $\rightarrow \kappa_n = \kappa_1 cos^2\theta + \kappa_2 cos^2\theta$
  calculate constraint value
  for *node* $i = 1, 2, 3, ..., n$ **do**
    calculate $\boldsymbol{R}_i(\hat{\boldsymbol{d}}_i, \theta_i)$
    $\hat{\boldsymbol{d}}_i = \boldsymbol{R}_i \boldsymbol{d}_i$
    ray tracing along the ray $\hat{\boldsymbol{d}}_i + t\Delta\hat{\boldsymbol{d}}_i | t \leq 0$
    $g_V += h_i A_i$;
  calculate constraint sensitivities
  for *node* $i = 1, 2, 3, ..., n$ **do**
    $\frac{d\boldsymbol{g}_V}{d\boldsymbol{X}_i} = sign(\kappa_{n_i})\boldsymbol{n}_i A_i$
  calculate mapping matrix
  $\boldsymbol{A}^k = \frac{d\boldsymbol{X}^k}{d\boldsymbol{s}^k}$
  map objective and constraint sensitivities to control space
  $\frac{dJ}{d\boldsymbol{s}^k} = \frac{dJ}{d\boldsymbol{X}^k}\boldsymbol{A}^k$, $\frac{d\boldsymbol{g}_V}{d\boldsymbol{s}^k} = \frac{d\boldsymbol{g}_V}{d\boldsymbol{X}^k}\boldsymbol{A}^k$
  calculate search direction and design update
  $\boldsymbol{p}^k = \boldsymbol{P}\nabla_{\boldsymbol{s}} J$
  $\Delta\boldsymbol{s}^k = \alpha^k \boldsymbol{p}^k$
  calculate geometry update
  $\Delta\boldsymbol{X}^k = \boldsymbol{A}^k \Delta\boldsymbol{s}^k$
  check convergence
end procedure

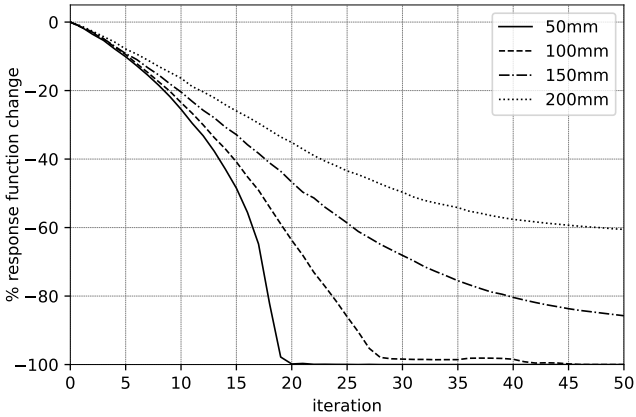

Figure 3.6 : Comparison of the evolution of the undercut response function value for the 2D optimization example for different filter radii.

3.2 Enhancement of Vertex Morphing parametrization

Bilateral reflection symmetry is an important feature of automotive design due to a series of multifaceted reasons, i.e., manufacturing limitations such as ease of production and assembly, pure aesthetic reasons of the final product and functionality issues such as weight balance to increase stability and control. In practical terms, any optimal design of a symmetric car part, should also be symmetric.

The Vertex Morphing parametrization itself is an example of such an approach. Node-based methods suffer from mesh dependency and sensitivity irregularity because of the ill-posed nature of the optimization problem [58, 64]. Common approaches for shape and mesh regularization are the addition of a penalization term into the objective functional. This is equal to adding a constraint to the optimization problem and formulating it by the use of a Lagrangian multiplier. On the other hand, Vertex Morphing introduces an explicit filter between control and geometry, an elaborate scaling of the design parameters in order to fulfill the aforementioned irregularities only through convolution of kernel with the geometry. Naturally, depending on the kernel values and type, a

wide range of effects are caused. The explicit linear mapping is chosen in a way to satisfy surface smoothness and mesh regularity criteria without burdening additional computational cost during solution.

In a similar manner, the kernel element values can be manipulated to incorporate geometric constraints in the optimization while avoiding adding a constraint to the mathematical problem. In this section, the reflection symmetry problem is tackled by modifying the kernel of the parametrization.

3.2.1 Variable convolution kernel

As discussed in section 2.3.1, the Vertex Morphing filter kernel, motivated by the Gaussian probability density function, has the following form:

$$A(\xi,\xi_0)=\frac{1}{\sqrt{2\pi}r}e^{-\frac{\|\boldsymbol{x}(\xi)-\boldsymbol{x}(\xi_0)\|^2}{2r^2}} \tag{3.18}$$

In 3D Vertex Morphing with implicit regularization, the regularizing term is in included directly in the filtering operator A in the form of the surface normal direction:

$$\bar{A}(\xi-\xi_0)=\frac{1}{\sqrt{2\pi}r}e^{-\frac{\|\boldsymbol{x}(\xi)-\boldsymbol{x}(\xi_0)\|^2}{2r^2}}\frac{g_1\otimes g_2}{\|g_1\times g_2\|_2} \tag{3.19}$$

and has an averaging effect on the surface normal direction scaled by the shape derivative or shape update [49]. Motivated by this, the following enhancement of the filter kernel is proposed:

$$A_{sym}(\xi-\xi_0)=\frac{1}{\sqrt{2\pi}r}e^{-\frac{\|\boldsymbol{x}(\xi)-\boldsymbol{x}(\xi_0)\|^2}{2r^2}}+\frac{1}{\sqrt{2\pi}r}e^{-\frac{\|\boldsymbol{x}(\xi)-\boldsymbol{x}'(\xi_0)\|^2}{2r^2}}\boldsymbol{S}(\xi,\boldsymbol{n}_p) \tag{3.20}$$

where the second term is an identical Gaussian kernel around the symmetric point $\boldsymbol{x}'(\xi_0)$ of $\boldsymbol{x}(\xi_0)$ and $\boldsymbol{S}(\xi)$ the function that returns the symmetric position of ξ coordinates over the symmetry plane with normal

vector $\boldsymbol{n}_p$:

$$\boldsymbol{S}(\xi, \boldsymbol{n}_p) = \begin{Bmatrix} S_1(\xi, \boldsymbol{n}_p) \\ S_2(\xi, \boldsymbol{n}_p) \\ S_3(\xi, \boldsymbol{n}_p) \end{Bmatrix} \tag{3.21}$$

with $S_i \in \mathbb{R}$.

In order to formulate the desired matrix that returns the reflected vector $\boldsymbol{p}'$ of ny vector $\boldsymbol{p}$ across the plane with aforementioned unit normal $\boldsymbol{n}_p$ we start from:

$$\boldsymbol{p}' = \boldsymbol{p} - 2\boldsymbol{p} \times \boldsymbol{n}_p \boldsymbol{n}_p \tag{3.22}$$

and the orthogonal matrix corresponding to the above equation is:

$$\boldsymbol{S}_{ij} = \delta_{ij} - 2n_{p,i} n_{p,j} \tag{3.23}$$

or

$$\boldsymbol{S}(\boldsymbol{n}_p) = \begin{bmatrix} 1-2n_{p1}^2 & -2n_{p1}n_{p2} & -2n_{p1}n_{p3} \\ -2n_{p2}n_{p1} & 1-2n_{p2}^2 & -2n_{p2}n_{p3} \\ -2n_{p3}n_{p1} & -2n_{p3}n_{p2} & 1-2n_{p3}^2 \end{bmatrix} \tag{3.24}$$

Unlike other methods where for every point $\boldsymbol{X}$ a symmetric point $\boldsymbol{X}'$ on the mesh has to exist, in the proposed enhanced parametrization mesh density around the reflection plane does not have to be identical, as also shown in figure 3.7 where $\Psi_1 \neq \Psi_2$. This increases the robustness of the method and avoids inaccuracies because of numerical and precision errors.

3.2.2 Reflection-symmetric Vertex Morphing

The geometry at point $\boldsymbol{X}_0$ is calculated based on the convolution between the new kernel and the control field $\boldsymbol{s}$ exactly as before only with the

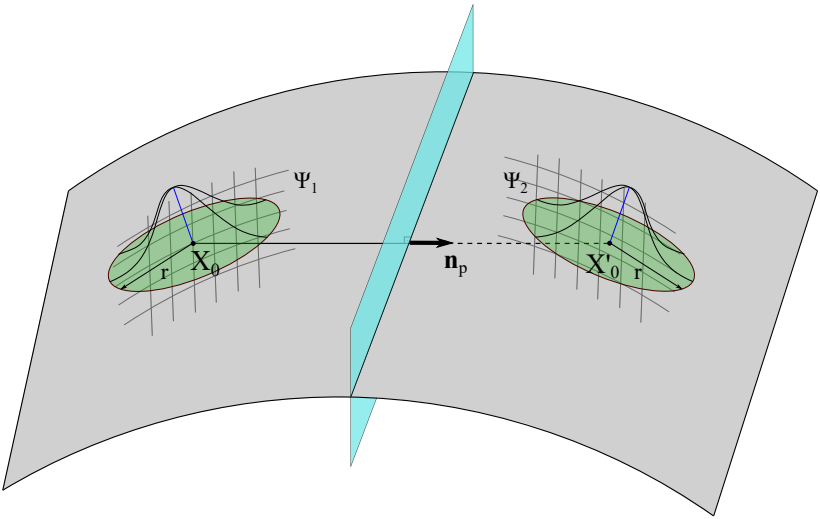

Figure 3.7 : Schematic representation of the proposed filter function for reflection symmetric node-based shape optimization with Vertex Morphing.

new convolution kernel as:

$$\begin{aligned} \boldsymbol{x}(\xi_0) &= \int_\Gamma A_{sym}(\xi-\xi_0)\boldsymbol{s}(\xi)d\Gamma \\ &= \int_\Gamma A(\xi-\xi_0)+A_{sym}(\xi-\xi_0')\boldsymbol{s}(\xi)d\Gamma \\ &= \int_\Gamma A(\xi-\xi_0)\boldsymbol{s}(\xi)d\Gamma + \int_\Gamma A(\xi-\xi_0')\boldsymbol{S}(\xi,\boldsymbol{n}_p)\boldsymbol{s}(\xi)d\Gamma \end{aligned} \tag{3.25}$$

Applying the proposed filter is equivalent to averaging the shape derivative or shape update along the symmetry plane. Figure 3.7 illustrates the concept of the proposed filter. Finally, the inclusion of the surface normal direction of equation 3.19 as a regularizing term has no effect on the reflection symmetry and is a matter of choice.

3.2.3 Example

The modified Vertex Morphing mapping is applied on a simple 1D optimization, shown in figure 3.8, and is compared against the classical Vertex Morphing. Two different filter radius sizes were applied.

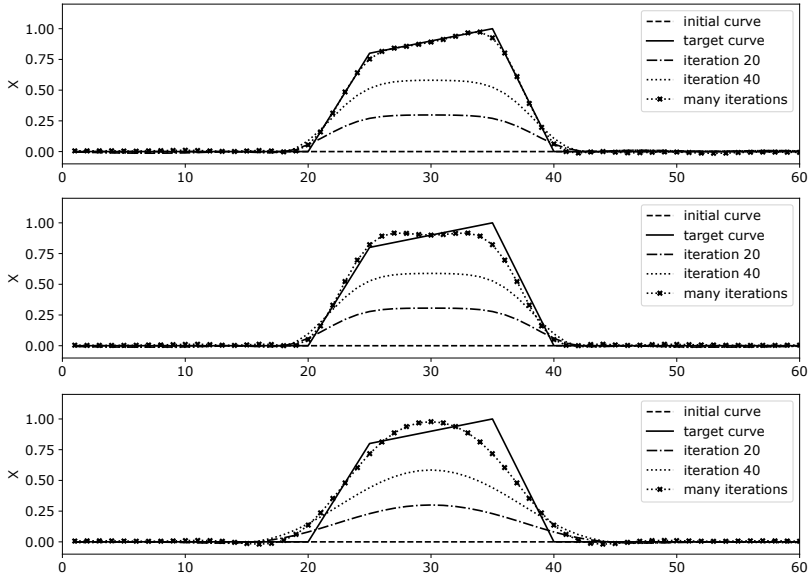

Figure 3.8 : 2D example of node-based shape optimization with Vertex Morphing (top) and reflection symmetric Vertex Morphing with two filter radii, 6 (middle) and 12(bottom).

It is interesting to be noted, that the proposed enhancement densifies the mapping matrix. The level of densification also depends on the symmetry plane orientation. When it coincides with one of the global coordinate planes, the diagonal elements of the reflection matrix $\boldsymbol{S}(\boldsymbol{n}_p)$ become zero. Since the components of the filtered vector field are multiplied with $\boldsymbol{S}(\boldsymbol{n}_p)$ around symmetric point $\boldsymbol{X}_0'$, the matrix densification is greater for symmetry planes which not coincide with a global coordinate plane. By rotating the geometry of figure 3.8 by 45° and calculating again the mapping matrix, the observation becomes apparent in figure 3.9.

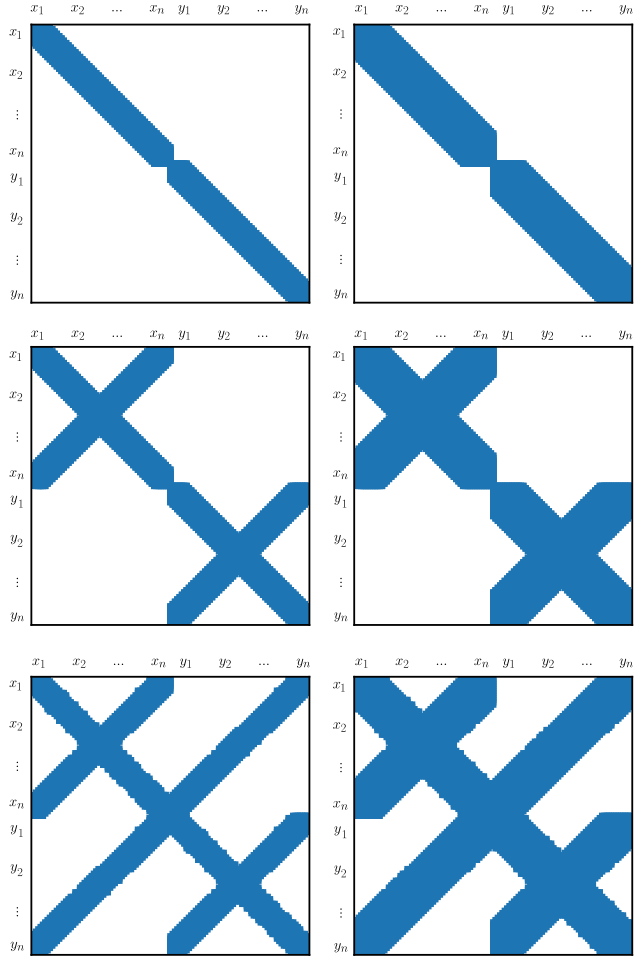

Figure 3.9 : Sparsity pattern of Vertex Morphing mapping matrix without (top) and with (middle and bottom) reflection symmetry (bottom example rotated by 45° for two different radii, 6 (left row) and 12 (right column).

3.3 Extension of Vertex Morphing parametrization

This chapter discusses the 1-dimensional extension of Vertex Morphing parametrization with a new set of nodal design variables to accommodate the need for weight reduction in the automotive industry. The added design variables are the nodal thickness values of the geometry to be optimized. The method described in this chapter is the first approach to use the Vertex Morphing parametrization with non-geometric design variables other than nodal coordinates. The explicit filtering smoothing function of Vertex Morphing replaces the common sensitivity filtering of topology optimization. At the center of attention was the satisfaction of the strict manufacturing (industrial) constraint of constant sheet thickness. To this end, along with the use of a SIMP-inspired formulation, a re-parametrization of the newly introduced thickness design variables is suggested with the use of another mapping function, on top of the existing Vertex Morphing mapping. Finally, the scaling of shape and thickness updates is tackled with an appropriate scaling of the initial objective sensitivities resulting from a root finding algorithm.

3.3.1 Industrial problem formulation

As already discussed, weight reduction is an important factor in the design of car components. It reduces manufacturing and material costs, as well as the ecological footprint of a structure. The most well-fitted optimization type for weight reduction is topology optimization. The classical topology optimization problem has already been thoroughly described in 2.4 as the search for the topology of a sub-domain Ω_s, which maximizes an objective function Φ, under the volume constraint $\frac{V_{\Omega_s}}{V_\Omega} < 1.0$. For weight reduction of solid geometries node-based shape optimization can also be used, under the condition that the internal nodes are updated according to the shape update of the surface (a relevant industrial application and the implemented mesh motion framework are presented in chapter 4).

For surface geometries specifically, weight reduction is equivalent to surface minimization. Shape optimization is a rather inefficacious approach, since the main mode of surface minimization is through geometry shrink-

age i.e., in-plane translation of the edge nodes, and flattening of the surface through update of non-edge nodes in the surface normal direction. Shape change of the edge nodes is often prohibited because of geometric limitations e.g., neighboring or contact with other components. Likewise, surface flattening is depriving sheet metal components of invaluable stiffening beads, which are usually a result of stiffness shape optimization. In constrained shape optimization it becomes difficult, if not impossible, to minimize the weight of a geometry and, at the same time, increase its stiffness and/ or satisfy general industrial constraints.

A possible solution is to sequentially shape optimize for stiffness maximization and then reduce the part thickness manually until the desired weight reduction and compliance improvement are reached. On the other hand, the realization of classical topology optimization in the case of optimizing preexisting car components is more complex. Any reduction of mass because of the topology optimization leads obviously to a reduced stiffness. This has to be counteracted with a total thickness increase to achieve the desired stiffness. As before, this has to be conducted manually and the whole process might have to be done more than once.

Combining shape and topology optimization exploits the potential of both methods; structural stiffening through out-of-plane shape update and void creation to reduce mass. To this end, we propose the extension of Vertex Morphing parametrization with a new set of design variables that lead to a variable thickness distribution of the surface shell. The optimization problem, with both sets of design variables, may then be defined as:

$$
\begin{aligned}
\min_{\boldsymbol{X},\boldsymbol{t}} \quad & F(\boldsymbol{X},\boldsymbol{t},\boldsymbol{u}(\boldsymbol{X},\boldsymbol{t})) && \boldsymbol{X},\boldsymbol{t} \in \mathbb{R}^n, \boldsymbol{u} \in \mathbb{R}^m \\
& h_i(\boldsymbol{X},\boldsymbol{t}) = 0 && h_i \in \mathbb{R}, i = 1,...,p \\
& g_j(\boldsymbol{X},\boldsymbol{t}) \leq 0 && g_j \in \mathbb{R}, j = 1,...,q \\
& r_k(\boldsymbol{X},\boldsymbol{t},\boldsymbol{u}(\boldsymbol{X},\boldsymbol{t})) = 0 && k = 1,...,m \\
& t_{min} \leq t_l \leq t_{max} && l = 1,...,n
\end{aligned}
\tag{3.26}
$$

where $\boldsymbol{X} = \left[X_1^1, X_1^2, X_1^3, ..., X_n^1, X_n^2, X_n^3\right]^T$ stands for the nodal coordinates vector, $\boldsymbol{t} = \left[t_1, t_2, ..., t_n\right]^T$ is the nodal thickness vector. $\boldsymbol{u}$ is the state variables vector and $\boldsymbol{r}$ is the residual vector of the governing equations of the problem, usually linear in gradient-based optimization. Finally, F is the objective function to be minimized, h_i and g_j the ith equality constraint and jth inequality constraint respectively. Since Vertex Morphing is a node-based parametrization, the initial element thickness values are mapped on the nodes and mapped back at every optimization iteration.

In this work attention was given to develop methods that fit to the present design development and optimization techniques. During the automotive design process, more often than not, it is a preexisting design that needs to be optimized in terms of weight and structural performance. For every car component there exist a series of loading conditions and respective structural limit i.e, a total compliance value, a maximum allowed total displacement of a node of interest or a maximum allowed element stress in the structure under a load case. Setting those functions as constraints to be satisfied facilitates the problem formulation, since the limit value are known. The objective function then becomes the mass $F = \int_\Omega \rho \, d\Omega$ to be minimized. The question to be answered by the optimization is: “what is the maximal possible mass reduction that can be achieved while the structural performance is not compromised?”.

Moreover, the starting values $\boldsymbol{t}_0$ of the thickness design variables are chosen to be equal to the maximum allowed thickness t_{max} of the problem. In this way, the discretized geometry of the finite element simulation is the input, as such, of the optimization. The implication here is that the thickness change during the optimization will be only in one direction, towards the minimum t_{min} which is usually 0 (void).

A simple approach to solve the problem is to decouple the shape from the thickness design variables and effectively solve two optimization problems per optimization iteration i.e., calculate one search direction for the shape and one for the thickness design variables separately. Consequently, we obtain a shape update $\Delta\boldsymbol{X}$ and a thickness update $\Delta\boldsymbol{t}$ independently and then move on to the next iteration. The projection

matrix is, as mentioned in chapter 2.3.2:

$$\boldsymbol{P} = \boldsymbol{I} - \boldsymbol{C}_m(\boldsymbol{C}_m^T \boldsymbol{C}_m)^{-1} \boldsymbol{C}_m^T \tag{3.27}$$

In the case where the optimization problem has only one constraint, the active constraint matrix $\boldsymbol{C}_m$ is equal to the vector gradient ∇g. The term $(\boldsymbol{C}_m^T \boldsymbol{C}_m)^{-1} = 1/\|\nabla g\|_2^2$ is for normalization of the constraint gradient. Formulating two projected directions we obtain:

$$\begin{aligned} \boldsymbol{p}_{\boldsymbol{X}} &= \left(\boldsymbol{I} - \frac{\nabla_{\boldsymbol{X}} g \nabla_{\boldsymbol{X}} g^T}{\|\nabla_{\boldsymbol{X}} g\|_2^2} \right) \nabla_{\boldsymbol{X}} F = \left(\boldsymbol{I} - \nabla_{\boldsymbol{X}} \tilde{g} \nabla_{\boldsymbol{X}} \tilde{g}^T \right) \nabla_{\boldsymbol{X}} F \\ \boldsymbol{p}_{\boldsymbol{t}} &= \left(\boldsymbol{I} - \frac{\nabla_{\boldsymbol{t}} g \nabla_{\boldsymbol{t}} g^T}{\|\nabla_{\boldsymbol{t}} g\|_2^2} \right) \nabla_{\boldsymbol{t}} F = \left(\boldsymbol{I} - \nabla_{\boldsymbol{t}} \tilde{g} \nabla_{\boldsymbol{t}} \tilde{g}^T \right) \nabla_{\boldsymbol{t}} F \end{aligned} \tag{3.28}$$

The outer product $\nabla \tilde{g} \nabla \tilde{g}^T$ projects the gradient ∇F parallel to the direction of $\nabla \tilde{g}$. Using this approach, the objective gradient with respect to thickness variables is not projected into the subspace tangent to the active constraint gradient with respect to shape variables, and vice versa.

$$\begin{bmatrix} \boldsymbol{p}_{\boldsymbol{X}} \\ \boldsymbol{p}_{\boldsymbol{t}} \end{bmatrix} =$$

$$\begin{bmatrix} \nabla^2_{\boldsymbol{X}} \tilde{g}_1 & \nabla_{\boldsymbol{X}} \tilde{g}_1 \nabla_{\boldsymbol{X}} \tilde{g}_2 & \cdots & \nabla_{\boldsymbol{X}} \tilde{g}_1 \nabla_{\boldsymbol{X}} \tilde{g}_{3n} & 0 & 0 & \cdots & 0 \\ \nabla_{\boldsymbol{X}} \tilde{g}_2 \nabla_{\boldsymbol{X}} \tilde{g}_1 & \nabla^2_{\boldsymbol{X}} \tilde{g}_2 & \cdots & \nabla_{\boldsymbol{X}} \tilde{g}_2 \nabla_{\boldsymbol{X}} \tilde{g}_{3n} & 0 & 0 & \cdots & 0 \\ \vdots & & \ddots & \vdots & \vdots & \vdots & \ddots & \vdots \\ \nabla_{\boldsymbol{X}} \tilde{g}_n \nabla_{\boldsymbol{X}} \tilde{g}_1 & \nabla_{\boldsymbol{X}} \tilde{g}_n \nabla_{\boldsymbol{X}} \tilde{g}_2 & \cdots & \nabla^2_{\boldsymbol{X}} \tilde{g}_{3n} & 0 & 0 & \cdots & 0 \\ 0 & 0 & \cdots & 0 & \nabla^2_{\boldsymbol{t}} \tilde{g}_1 & \nabla_{\boldsymbol{t}} \tilde{g}_1 \nabla_{\boldsymbol{t}} \tilde{g}_2 & \cdots & \nabla_{\boldsymbol{t}} \tilde{g}_1 \nabla_{\boldsymbol{t}} \tilde{g}_n \\ 0 & 0 & \cdots & 0 & \nabla_{\boldsymbol{t}} \tilde{g}_2 \nabla_{\boldsymbol{t}} \tilde{g}_1 & \nabla^2_{\boldsymbol{t}} \tilde{g}_2 & \cdots & \nabla_{\boldsymbol{t}} \tilde{g}_2 \nabla_{\boldsymbol{t}} \tilde{g}_n \\ \vdots & \vdots & \ddots & \vdots & \vdots & \vdots & \ddots & \vdots \\ 0 & 0 & \cdots & 0 & \nabla_{\boldsymbol{t}} \tilde{g}_n \nabla_{\boldsymbol{t}} \tilde{g}_1 & \nabla_{\boldsymbol{t}} \tilde{g}_n \nabla_{\boldsymbol{t}} \tilde{g}_2 & \cdots & \nabla^2_{\boldsymbol{t}} \tilde{g}_n \end{bmatrix} \begin{bmatrix} \nabla_{\boldsymbol{X}} F_1 \\ \nabla_{\boldsymbol{X}} F_2 \\ \vdots \\ \nabla_{\boldsymbol{X}} F_{3n} \\ \nabla_{\boldsymbol{t}} F_1 \\ \nabla_{\boldsymbol{t}} F_2 \\ \vdots \\ \nabla_{\boldsymbol{t}} F_n \end{bmatrix} \tag{3.29}$$

There is no synergy between thickness and shape sensitivities and the optimization problem is effectively constrained twice i.e., once for the shape and once for the thickness design variables. Shape change cannot reduce the mass drastically and thickness change cannot increase the stiffness without increasing the maximum allowed thickness t_{max}. No surface cutting evolution since structural limit cannot be reached without thickness increase.

This is illustrated schematically in the simple 2D optimization problem of figure 3.10. Starting from design $\boldsymbol{x}^{(i)}$ in the graph, optimizing once for design variable x_1 and subsequently for design variable x_2 violates constraint g after the design is updated to $\boldsymbol{x}^{(x+1)}$, even though g is not violated after optimizing only for x_1 (design $\boldsymbol{x}_1^{(i+1)}$) and x_2 (design $\boldsymbol{x}_2^{(i+1)}$). On other hand, treating the problem as whole, violation would not occur and would only depend on the step size length.

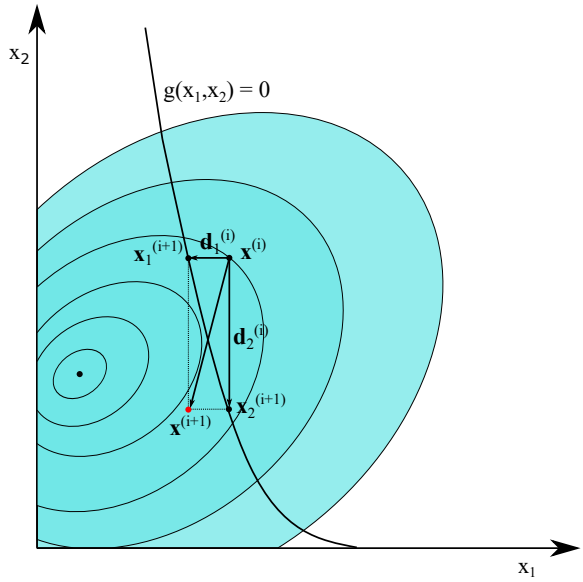

Figure 3.10 : Staggered 2D function constrained optimization iteration first for design variable x_1 and then for x_2.

In this work, shape and thickness design variables are optimized simultaneously and only one search direction and geometry update are considered at every step as a solution to the problems of the previous paragraph. The unified approach is presented in the next section.

3.3.2 4D Vertex Morphing

A new 4D design variable vector $\boldsymbol{v}$ is introduced. The optimization problem of 3.26 is reformulated:

$$\begin{aligned}
\min_{\boldsymbol{v}} \quad & F(\boldsymbol{v},\boldsymbol{u}(\boldsymbol{v})) && \boldsymbol{v}\in\mathbb{R}^n, \boldsymbol{u}\in\mathbb{R}^m && \\
& h_i(\boldsymbol{v})=0 && h_i\in\mathbb{R} && i=1,...,p \\
& g_j(\boldsymbol{v})\le 0 && g_j\in\mathbb{R} && j=1,...,q \\
& r_k(\boldsymbol{v},\boldsymbol{u}(\boldsymbol{v}))=0 && && k=1,...,m \\
& t_{min}\le t_l\le t_{max} && && l=1,...,n
\end{aligned} \tag{3.30}$$

where $\boldsymbol{v}=\left[s_x^1,s_y^1,s_z^1,s_t^1,...,s_x^n,s_y^n,s_z^n,s_t^n\right]^T$ is the vector of shape and thickness design variables in the Vertex Morphing control space which will be simultaneously optimized in a unified formulation. The search direction is now:

$$\begin{aligned}
\boldsymbol{p_v} &= \left(\boldsymbol{I}-\nabla_{\boldsymbol{v}}\tilde{g}\otimes\nabla_{\boldsymbol{v}}\tilde{g}\right)\nabla_{\boldsymbol{v}}F \\
&= \left(\begin{bmatrix} 1 & 0 & \dots & 0 \\ 0 & 1 & \dots & 0 \\ \vdots & \vdots & \ddots & \vdots \\ 0 & 0 & \dots & 1 \end{bmatrix} - \begin{bmatrix} \nabla_{\boldsymbol{v}}^2\tilde{g}_1 & \nabla_{\boldsymbol{v}}\tilde{g}_1\nabla_{\boldsymbol{v}}\tilde{g}_2 & \dots & \nabla_{\boldsymbol{v}}\tilde{g}_1\nabla_{\boldsymbol{v}}\tilde{g}_n \\ \nabla_{\boldsymbol{v}}\tilde{g}_2\nabla_{\boldsymbol{v}}\tilde{g}_1 & \nabla_{\boldsymbol{v}}^2\tilde{g}_2 & \dots & \nabla_{\boldsymbol{v}}\tilde{g}_2\nabla_{\boldsymbol{v}}\tilde{g}_n \\ \vdots & \vdots & \ddots & \vdots \\ \nabla_{\boldsymbol{v}}\tilde{g}_n\nabla_{\boldsymbol{v}}\tilde{g}_1 & \nabla_{\boldsymbol{v}}\tilde{g}_n\nabla_{\boldsymbol{v}}\tilde{g}_2 & \dots & \nabla_{\boldsymbol{v}}^2\tilde{g}_n \end{bmatrix}\right) \begin{bmatrix} \nabla_{\boldsymbol{v}}F_1 \\ \nabla_{\boldsymbol{v}}F_2 \\ \vdots \\ \nabla_{\boldsymbol{v}}F_n \end{bmatrix} \\
&= \begin{bmatrix} 1-\nabla_{\boldsymbol{v}}^2\tilde{g}_1 & \nabla_{\boldsymbol{v}}\tilde{g}_1\nabla_{\boldsymbol{v}}\tilde{g}_2 & \dots & \nabla_{\boldsymbol{v}}\tilde{g}_1\nabla_{\boldsymbol{v}}\tilde{g}_n \\ \nabla_{\boldsymbol{v}}\tilde{g}_2\nabla_{\boldsymbol{v}}\tilde{g}_1 & 1-\nabla_{\boldsymbol{v}}^2\tilde{g}_2 & \dots & \nabla_{\boldsymbol{v}}\tilde{g}_2\nabla_{\boldsymbol{v}}\tilde{g}_n \\ \vdots & \vdots & \ddots & \vdots \\ \nabla_{\boldsymbol{v}}\tilde{g}_n\nabla_{\boldsymbol{v}}\tilde{g}_1 & \nabla_{\boldsymbol{v}}\tilde{g}_n\nabla_{\boldsymbol{v}}\tilde{g}_2 & \dots & 1-\nabla_{\boldsymbol{v}}^2\tilde{g}_n \end{bmatrix} \begin{bmatrix} \nabla_{\boldsymbol{v}}F_1 \\ \nabla_{\boldsymbol{v}}F_2 \\ \vdots \\ \nabla_{\boldsymbol{v}}F_n \end{bmatrix}
\end{aligned} \tag{3.31}$$

It now becomes obvious that by calculating one search direction and optimizing both sets of design variables in one go the objective function is projected into the subspace tangent to the constraint function with respect to shape and thickness variables and the objective gradient components of thickness and shape are projected on the constraint gradient components of shape and thickness respectively.

In Vertex Morphing the linear mapping between control and geometry space is numerically computed as a matrix-vector-multiplication in its discretized form. A 1D extension of the parametrization technique does not modify the formulation since there is no distinction between shape

and thickness sensitivities and design variables, at least algorithmic-wise. Unless otherwise noted, the mapping matrix $\boldsymbol{A}$ projects the 4D geometry to a 4D control field, i.e., control and geometry field have the same discretization, in which case the matrix is square and symmetric. Following this approach the geometry variation at point $\delta \boldsymbol{w}(\xi_0)$ and control update is:

$$\delta w(\xi_0) = \int_\Gamma A(\xi - \xi_0)\delta v(\xi) d\Gamma \tag{3.32}$$

where

$$A(\xi - \xi_0) = \frac{1}{\sqrt{2\pi r}} e^{-\frac{\|w(\xi)-w(\xi_0)\|^2}{2r^2}} \tag{3.33}$$

and $w(\xi), v(\xi)$ the continuous geometry and control fields.

The sensitivity vector is then calculated as in equation 2.35 of section 2.3.1:

$$\frac{dF}{dv(\xi_0)} = \int_\Gamma \frac{dF}{dw(\xi)} A(\xi - \xi_0) d\Gamma \tag{3.34}$$

and on the discretized geometries as a sum over weighted nodal values

$$\begin{aligned} \boldsymbol{v} &= \left(s_x^1, s_{x_y}^1, s_{x_z}^1, s_t^1, \cdots, s_x^n, s_{x_y}^n, s_{x_z}^n, s_t^n \right) \\ \frac{dF}{d\boldsymbol{w}} &= \left(\frac{dF}{dx_x^1}, \frac{dF}{dx_y^1}, \frac{dF}{dx_z^1}, \frac{dF}{dt^1}, \cdots, \frac{dF}{dx_x^n}, \frac{dF}{dx_y^n}, \frac{dF}{dx_z^n}, \frac{dF}{dt^n} \right) \end{aligned} \tag{3.35}$$

it becomes:

$$\frac{dF}{dv_i} = A_{ji} \frac{dF}{dw_j} \tag{3.36}$$

In the case of Vertex Morphing with implicit mesh regularization, the filter kernel becomes:

$$A(\xi - \xi_0) = \frac{1}{\sqrt{2\pi r}} e^{-\frac{\|w(\xi)-w(\xi_0)\|^2}{2r^2}} \frac{g_1 \otimes g_2}{\|g_1 \times g_2\|_2} \tag{3.37}$$

where $\frac{g_1 \otimes g_2}{\|g_1 \times g_2\|_2} = \boldsymbol{n}$ is the surface normal unit vector. The convolution over shape control and thickness control fields should happen separately with different $\boldsymbol{n}$ unit vectors, since the 3D shape vector field is projected onto a 1D shape control scalar field and the 1D thickness scalar field is projected onto a 1D thickness control scalar field:

$$\boldsymbol{n}_{\boldsymbol{X}} = \frac{g_1 \otimes g_2}{\|g_1 \times g_2\|_2}; \quad \boldsymbol{n}_{\boldsymbol{t}} = [0,0,0,1]^T \tag{3.38}$$

3.3.3 Filtering in topology optimization

Regularization schemes are also used in density-based topology optimization to avoid numerical problems such as checkerboard patterns and mesh-dependency, and to ensure manufacturability of the optimal design. One of the most widely used category of restriction methods is that of sensitivity, or density, filtering [86]. The original density or sensitivity fields are heuristically modified as weighted averages of the densities or sensitivities in the neighborhood elements $N_e = \{i \in \quad \|\boldsymbol{x}_i - \boldsymbol{x}_e\| \leq R\}$, respectively.

Bruns and Tortorelli [24] introduced the density filter:

$$\tilde{\rho_e} = \frac{\sum\limits_{i \in N_e} \alpha(\boldsymbol{x}_i) V_i \rho_i}{\rho_e \sum\limits_{i \in N_e} \alpha(\boldsymbol{x}_i)} \tag{3.39}$$

where α is the weighing function equal to a hat or Gaussian distribution function and V_i is the volume of ith element. Sigmund [87] presented the original form of the sensitivity filter as:

$$\frac{\partial \tilde{F}}{\partial \rho_e} = \frac{\sum\limits_{i \in N_e} \alpha(\boldsymbol{x}_i) \rho_i \frac{\partial f}{\partial \rho_i}}{\rho_e \sum\limits_{i \in N_e} \alpha(\boldsymbol{x}_i)} \tag{3.40}$$

After a closer look, that is equivalent to the shape, forward mapping, and sensitivity, backward mapping, filtering applied with $\boldsymbol{A}$ matrix in Vertex Morphing. Thus, Vertex Morphing proves a fitting frame for density-based and thickness optimization.

3.3.4 Manufacturing restriction-reparametrization of thickness design variables

Geometries optimized with the 4D Vertex Morphing parametrization are composed of mostly intermediate thickness areas. At the same time, in Vertex Morphing the control field $\boldsymbol{v}$ does not need to be resolved and so neither the inverse of matrix $\boldsymbol{A}$. Therefore, the update rule for geometry $\boldsymbol{w}$ is simplified to $\boldsymbol{w}_{k+1} = \boldsymbol{w}_k + \Delta\boldsymbol{w} = \boldsymbol{w}_k + \boldsymbol{A}\Delta\boldsymbol{v}$ and without adding a constraint the nodal thickness can attain values larger than the allowed $\boldsymbol{t}_{max}$.

The above facts violate a crucial manufacturing-industrial constraint in the automotive industry, in that only constant thickness metal sheets can be mass-produced with current manufacturing methods e.g., drawing, hot working, forging. In this work, the SIMP power law, as described in chapter 2.4, is employed:

$$\begin{aligned} E &= t_e^p E_0 \\ \rho &= \rho_0 \\ \nu &= \nu_0 \\ m_e^i &= \rho\, t_e^i A_e^i \end{aligned} \tag{3.41}$$

where $p = 3$, ρ the material density of the geometry, ν the Poisson's ratio and m_e^i the mass of ith element.

The thickness variation of the geometry is represented by the scalar function $t(\xi, t) \in \mathbb{R}$ where $\xi = \{\xi_1, \cdots, \xi_{d-1}\} \in \mathbb{R}^d$ are the surface coordinates, as in the case of classical Vertex Morphing. Pseudo time t can be neglected for the sake of simplicity in the formulations.

The desired control field $\tau(\xi, t)$ that we are looking for should have desirable characteristics. The thickness update is driven by the gradient vector field. It is, thus, possible to control the desired update pattern by manipulating the sensitivities. This has to be accomplished in a consistent manner that does not alter the original problem, as was the case in Vertex Morphing. Goal is to restrict thickness from attaining unfeasible and physically meaningless values through reparametrization. Sensitivities close to t_{max}, t_{min} should be close to zero, whereas sensitivities of

intermediate thickness nodes should be magnified in order to steer the thickness values to either the upper or the lower limit and accelerate convergence. At the same time, any thickness values smaller than t_{min} or larger than t_{max} should be consistently prohibited as an innate feature of the mapping. The new design control field τ can attain values between 0 and 1 whereas the original thickness field between t_{min} and t_{max}.

The proposed relation between thickness and thickness-control field is a nonlinear S-shaped mapping $\Pi : \mathbb{V} \rightarrow \mathbb{V}$.

$$t(\xi) = \Pi(\tau(\xi)) = \frac{1}{1 + e^{-a(b\,\tau(\xi) - c)}} \tag{3.42}$$

where a, b and c are function parameters that affect the shape, steepness and placement of the S curve. In this work, $a = 0.3$, $b = 60$ and $c = 30$ are used, as is attested to be the "magic numbers" in Yoon and Kim [98].

The calculation of the inverse function that maps the thickness field to the control thickness field is easily retrieved as:

$$\tau(\xi) = \Pi^{-1}(t(\xi)) = \frac{1/\tilde{t}(\xi) - 1}{b\,s} + \frac{1}{2} \tag{3.43}$$

where $\tilde{t}$ is the normalized thickness in range from 0 to 1:

$$\tilde{t}_i = \frac{t_i - t_{min}}{t_{max} - t_{min}} \tag{3.44}$$

The simplicity of the calculation of the inverse mapping, in contrast to Vertex Morphing where the inverse $\boldsymbol{A}^{-1}$ is computationally costly, allows us to map backward and forward with ease. Therefore, instead of mapping back only the variation $\delta t(\xi_0)$ as:

$$\delta t(\xi_0) = \frac{1}{1 + e^{-a(b\,\delta\tau(\xi_0) - c)}} \tag{3.45}$$

we update the control thickness field and re-calculate the geometry thickness based on it. Note that the variation $\delta t(\xi_0)$ depends exclusively on the variation $\delta\tau(\xi_0)$ and not that of neighboring nodal values as is the convolution-based mapping of Vertex Morphing.

Naturally, the sensitivity of the objective with respect to the design control field is needed for our gradient-based optimizer:

$$\frac{dF}{d\tau} = \frac{\partial \Pi(\tau)}{\partial \tau} \frac{dF}{dt(\xi)} \tag{3.46}$$

and the sensitivity field is scaled by the mapping function derivative of next figure. It can be noted that the design sensitivity becomes very small as τ approaches 0 or 1 and very large when τ has a value around 0.5. The derivative of the mapping function can be retrieved easily and is equal to:

$$\frac{\partial \Pi}{\partial \tau(\xi)} = \frac{b\,s\,e^{-s(b\tau(\xi)-a)}}{(e^{-s(b\tau(\xi)-a)}+1)^2} \tag{3.47}$$

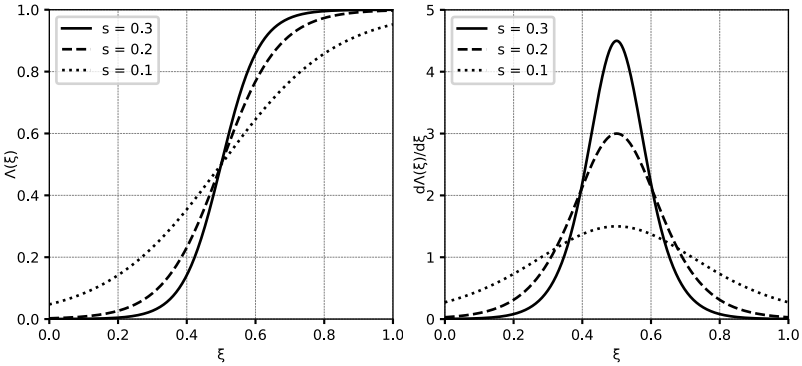

Figure 3.11 : S-shaped mapping function for thickness design variables (left) and its derivative with respect to new design variable τ for different values of s (right).

3.3.5 Root finding algorithm for step size scaling

The kth design update is derived, as a explained above, from the projection of the objective function into the subspace tangent to the active constraints and subsequently the correction step. In many gradient-based optimization algorithms a one-dimensional search is carried out in the projected direction in order to determine the optimal step size. In this work a constant step size is applied in every optimization iteration. In

classical Vertex Morphing, the step size is usually chosen reasonably small and a rule of thumb is a few times smaller than the geometry element size. With the addition of thickness variables in the optimization problem and by solving them simultaneously with the shape ones, we immediately face the problem of contradicting step size magnitudes. The step size for the thickness variables should be much smaller than that for the shape variables. Scaling the shape variables and the thickness variables part of the update vector with different step sizes modifies the search direction and it not lying onto the subspace tangent space to the active constraints anymore and updating in this direction will violate the constraints.

Volume and compliance functions of the structure are more sensitive to a unit thickness change than to a unit change of the coordinates. Thus, the gradient of the objective and physical constraint with respect to thickness variables are greater in magnitude than gradient with respect to shape.

By scaling the objective thickness sensitivities with a scalar value μ, we manipulate the difference in the order of magnitude between the shape and the thickness component of the search direction after the projection into the tangent subspace. Consequently, after scaling the search direction with the constant step size, we can achieve the desired shape and thickness step size ratio

$$Q^{\star} = \frac{d_{s_x}}{d_{s_t}} \tag{3.48}$$

where d_{s_x} the shape step size and d_{s_t} the thickness step size in the control space.

This becomes a root-finding problem at every optimization iteration k of the function:

$$f(\mu) = Q_{\mu}^{k}(\mu) - Q^{*} = 0 \tag{3.49}$$

where Q_{μ}^{k} is the step size ratio of iteration k after scaling of thickness sensitivities with factor μ i.e., the factor μ is sought, for which $Q_{\mu}^{k} = Q^{*}$. A closed-form expression of Q_{μ}^{k} is remained to be formulated.

Going back to equation 2.49 of the search direction, after correction we get:

$$\boldsymbol{p_v} = \left(\boldsymbol{I} - \nabla_{\boldsymbol{v}}\tilde{g} \otimes \nabla_{\boldsymbol{v}}\tilde{g}\right)\nabla_{\boldsymbol{v}}F - \nabla_{\boldsymbol{v}}\tilde{g}\, g_a \tag{3.50}$$

and by setting $\boldsymbol{P} = \boldsymbol{I} - \nabla_{\boldsymbol{v}}\tilde{g} \otimes \nabla_{\boldsymbol{v}}\tilde{g}$ as the projection matrix, the equation is simplified to:

$$\boldsymbol{p_v} = \boldsymbol{P}\nabla_{\boldsymbol{v}}F - \nabla_{\boldsymbol{v}}\tilde{g}\, g_a \tag{3.51}$$

To obtain the shape and the thickness step sizes, the shape and thickness components of the search direction vector have to be separated by multiplication with matrices $\boldsymbol{X}$ and $\boldsymbol{T}$ where

$$X_{ij} = \begin{cases} 1, & \text{if } i = j \quad \text{and} \quad i \bmod 4 \neq 0 \\ 0, & \text{otherwise} \end{cases} \tag{3.52}$$

$$T_{ij} = \begin{cases} 1, & \text{if } i = j \quad \text{and} \quad i \bmod 4 = 0 \\ 0, & \text{otherwise} \end{cases} \tag{3.53}$$

with $\boldsymbol{X}$ the matrix that after the matrix-vector multiplication $\boldsymbol{X}\nabla_{\boldsymbol{v}}F$ extracts the shape sensitivity components and $\boldsymbol{T}$ the equivalent matrix for the thickness sensitivity components.

and then normalized with their respective max-norm.

$$\begin{aligned} d^k_{s_x} &= \lim_{p\to\infty}\left(\sum_{i=1}^{4n} \| \boldsymbol{X}\left(\nabla_v F^k_\mu \boldsymbol{P}^k - \boldsymbol{C}^k_m(\boldsymbol{C}^{k,T}_m \boldsymbol{C}^k_m)^{-1}\boldsymbol{g}^k_a\right)\|^p_i\right)^{1/p} \\ d^k_{s_\tau} &= \lim_{p\to\infty}\left(\sum_{i=1}^{4n} \| \boldsymbol{T}\left(\nabla_v F^k_\mu \boldsymbol{P}^k - \boldsymbol{C}^k_m(\boldsymbol{C}^{k,T}_m \boldsymbol{C}^k_m)^{-1}\boldsymbol{g}^k_a\right)\|^p_i\right)^{1/p} \end{aligned} \tag{3.54}$$

Finally, applying the above equations the ratio of shape to thickness step size takes the following form:

$$Q^k = \frac{\| \boldsymbol{X}\left(\nabla_v F^k_\mu \boldsymbol{P}^k - \boldsymbol{C}^k_m(\boldsymbol{C}^{k,T}_m \boldsymbol{C}^k_m)^{-1}\boldsymbol{g}^k_a\right)\|_\infty}{\| \boldsymbol{T}\left(\nabla_v F^k_\mu \boldsymbol{P}^k - \boldsymbol{C}^k_m(\boldsymbol{C}^{k,T}_m \boldsymbol{C}^k_m)^{-1}\boldsymbol{g}^k_a\right)\|_\infty} \tag{3.55}$$

where

$$\nabla_v F_\mu^k = \boldsymbol{X} \nabla_v F^k + \boldsymbol{T} \nabla_v F^k \mu \tag{3.56}$$

is the modified search direction of optimization iteration k after multiplication of thickness sensitivities with the factor μ. It should be noted, that constraint thickness sensitivities are only factored with μ in the correction term of the search direction. The reason for this is, that scaling the constraint thickness sensitivity terms of projection matrix $\boldsymbol{P}$ would lead to altering of the physical problem and moving in the projected direction would be moving away from the constraint limit.

Since the problem is solved in its discretized form and no analytic expression of the rational equation is available, an effective way to find the roots is by applying a robust closed-domain (bracketing) method. The idea is is to start the algorithm with two guess values of μ that "bracket" the root, and iteratively reduce the interval between left and right guess values while the root remains in this interval. The advantage is that if the initial guesses indeed bracket the root, then the algorithm is guaranteed to converge. The Illinois algorithm [35], based on the classic regular falsi method [32], is used.

Regarding the factor μ, we are looking for positive values, so that the physical meaning of gradients does not change. A negative value would swap the search direction and instead of minimizing the objective function it would be maximized. The denominator of the fraction in equation 3.55 can be zero, if and only if the thickness components' search direction is a zero vector. This is the case when the objective thickness sensitivity is equal to the negative of the thickness correction direction, which is only possible when objective and constraint gradients are anti-parallel. However, that would mean that a local minimum has been reached and the objective function cannot further be reduced without violating the constraint.

To obtain an upper bound μ_R for the bracketing interval, the largest $|(\boldsymbol{X} \nabla_v F_\mu^k \boldsymbol{P}^k)_i|$ and the largest $|(\boldsymbol{T} \nabla_v F_\mu^k \boldsymbol{P}^k)_j|$ are taken to solve the fol-

lowing equation:

$$\begin{aligned} Q_\mu^k(\mu) - Q^* &= 0 \\ Q_\mu^k(\mu) &= Q^* \\ |\boldsymbol{X}\left((\nabla_v F_\mu^k \boldsymbol{P}^k)_i - (\tilde{\boldsymbol{C}}_m^k \boldsymbol{g}_a^k)_i\right)| &= Q^* |\boldsymbol{T}\left((\nabla_v F_\mu^k \boldsymbol{P}^k)_j - (\tilde{\boldsymbol{C}}_m^k \boldsymbol{g}_a^k)_j\right)| \end{aligned} \tag{3.57}$$

as above that value the two terms in Q_μ^k should not cross the horizontal asymptote again. For the lower bound μ_L a very small positive value is ascribed.

Considering again equation (3.49) and the two initial approximations $\mu_{i-1} = \mu_L$ and $\mu_i = \mu_R$ for which $f(\mu_{i-1}) f(\mu_i) < 0$, a new approximation μ_{i+1} is obtained from:

$$\mu_{i+1} = \mu_i - \frac{f_i(\mu_i - \mu_{i-1})}{f_i - f_{i-1}} \tag{3.58}$$

and f_{i+1} is calculated. The estimates for the next iteration according to the Illinois method are decided based on:

- if $f_{i+1} f_i < 0$, then (μ_{i-1}, f_{i-1}) are displaced by (μ_i, f_i).
- if $f_{i+1} f_i > 0$, then (μ_{i-1}, f_{i-1}) are displaced by $(\mu_{i-1}, f_{i-1}/2)$.
- (μ_i, f_i) are displaced by (μ_{i+1}, f_{i+1}).

The modification of the second point above increases the asymptotic rate of convergence from linear, in the regula falsi method, to super-linear, in the Illinois method [38].

In the case where the estimations μ_L and μ_R at the start of the process do not yield $f(\mu_L) f(\mu_R) < 0$, μ_L and μ_R can be successively reduced and increased, respectively, until the limitation holds or a pure shape or topology optimization iteration can be implemented.

3.3.6 Example

In order to demonstrate the particularities of our method, a simple geometry is examined. A simultaneous shape and topology optimization of the geometry shown in figure 3.12 is solved. The maximum shape update length and maximum thickness update length in the control space were chosen equal to 0.25 mm and 0.025 mm, respectively, with a $4\,mm$ grid size and $1\,mm$ initial thickness. A Gaussian function is used for the filtering, as is the case for all applications in the framework of this dissertation. Finally, the optimization was performed with the gradient projection method until convergence. Customarily, the optimization is stopped either after full convergence is achieved or before severe mesh distortion occurs, which is the most common case for industrial applications.

Figure 3.13 shows the response functions' evolution along with a visual illustration of the optimized design and its thickness distribution during optimization. As it can be seen in the same figure, for approximately the first 15 iterations the rate of mass reduction is small, then rapidly increases for the next 50 iterations until it slows down again while converging to a value of around 40% less mass. This phenomenon can be explained by the nonlinearity of the introduced parametrization for the thickness design variables. At the extremities of the admissible thickness values, which are 0 and 1, the parametrization function slope is very close to zero, as can be seen in figure 3.11. Thus, even a relatively large thickness update in the control space, when mapped back amounts to a small thickness update. From a control thickness of around 0.75, the geometry thickness update is much larger than the control thickness update until control thickness reaches the low-end extremity again. At the same time, the strain energy minimization behavior is asymptotic until the constraint limit is reached. Once a local minimum is approached and all thickness values have reached either extremity (0 or 1), then the material and void pattern is almost impossible to change since thickness sensitivities very small. The slight increase in mass that is observed around the 100th iteration is due to the shape change (deepening of the beads etc.) needed to reach the constraint limit.

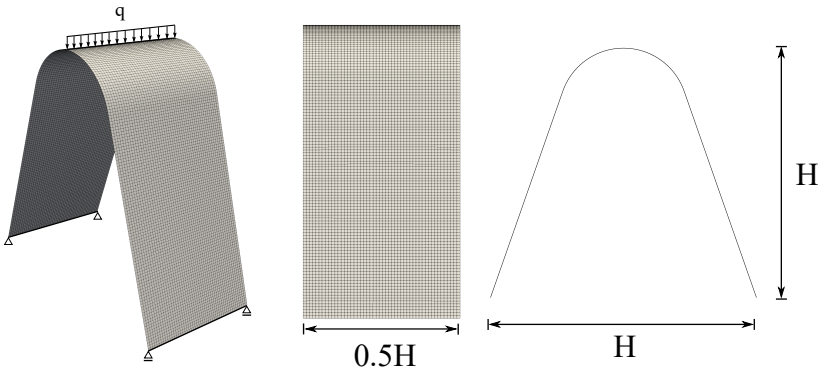

Figure 3.12 : 3D view of the example arch geometry (left), a front (middle) and side (right) view.

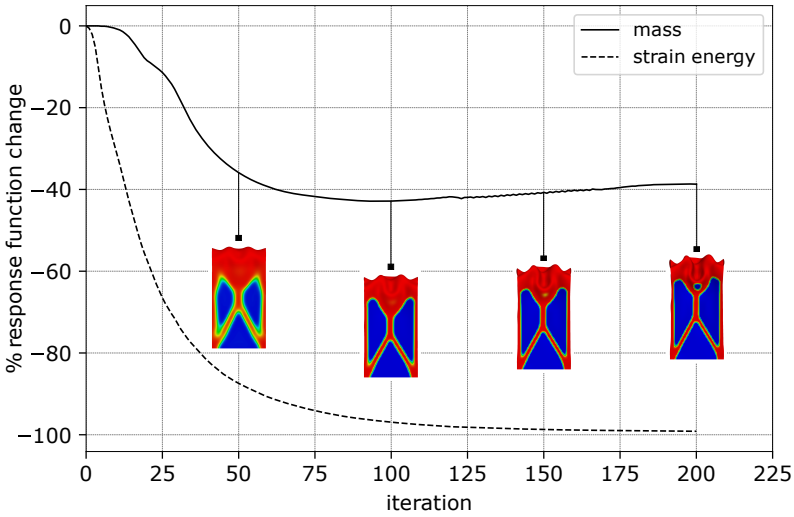

Figure 3.13 : Response function and design evolution of the example 3D arch geometry with the proposed simultaneous shape and topology optimization method.

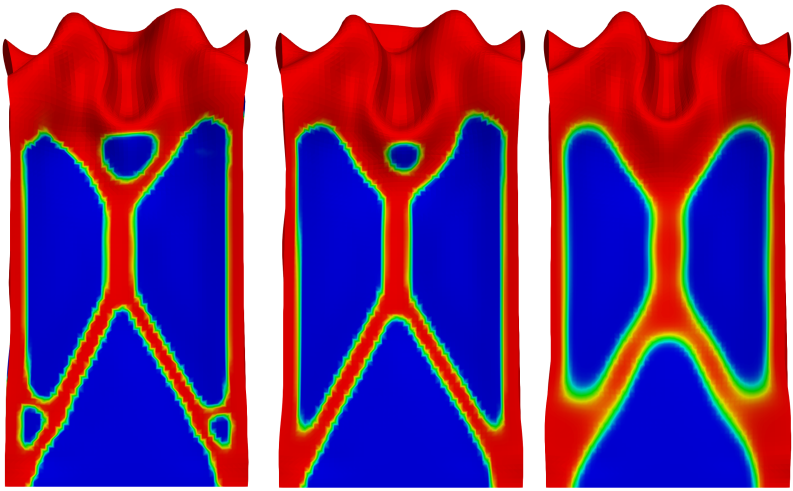

Figure 3.14 : Simultaneous shape and topology optimization result design with a filter radius length of 6 (left), 10 (middle) and 20 (right).

3.3.7 Simultaneous optimization design handles

The choice of the filter function and most importantly the filter radius size have already been identified as a design handles for shape optimization with the Vertex Morphing method [21, 48, 65]. Operator $\boldsymbol{A}$ acts as a low-pass filter that dictates the minimum shape wavelengths of the optimal design giving the engineer the option to steer the design towards local minima that satisfy functional and non-functional requirements.

The same effect is observed by varying the filter function radius size of the thickness design variables. Choosing a larger radius size explicitly affects the grey area phase between void and material. At the same time, it implicitly acts as a perimeter control for the thickness design variables evolution and limits the geometric complexity of the design. Larger and smoother voids are favored by a larger filter size. Moreover, appropriate selection of the filter size can also control the minimum member size of the topology. Figure 3.14 illustrates the aforementioned remarks. The larger the filter radius used for the thickness design variables, the

fewer and smoother the developed voids with a greater intermediate grey phase. The same phenomenon can be observed in the inner panel industrial application 4.4 of chapter 4.

3.3.8 Simultaneous optimization algorithm

In this section, the algorithm that was used in the context of this dissertation for the simultaneous shape and topology optimization with Vertex Morphing is thoroughly presented.

In order to not distract the focus from the main idea of the method, attention is not given on the optimization algorithm details. For a complete account of the Rosen's gradient projection algorithm, the reader is referred to chapter 2.3.2. The obtained results in the framework of this thesis can be consistently reproduced with the application of the following algorithm since there are no "hidden" or trial-and-error parameters.

Algorithm 3.2: Simultaneous shape and topology optimization algorithm.

initialize geometry $\boldsymbol{X}$ and nodal thickness $\boldsymbol{t}$

design variable vector $\rightarrow \boldsymbol{v} = \begin{bmatrix} \boldsymbol{X} \\ \boldsymbol{t} \end{bmatrix}$

define $t_{min}, t_{max}, d_{s_x}, d_{s_\tau}$

calculate initial thickness control field $\tilde{\boldsymbol{t}}$

$\boldsymbol{t} = \boldsymbol{T}\boldsymbol{v}$

$\tilde{t}_i = \frac{t_i - t_{min}}{t_{max} - t_{min}}$

$\boldsymbol{\tau} = \Lambda^{-1}(\tilde{\boldsymbol{t}}) \rightarrow \tau_i = -\frac{\ln\left(\frac{1}{\tilde{t}_i} - 1\right)}{60s} + 0.5$

for *optimization loop* $k = 1, 2, 3..., k$ **do**

  solve state problem

  $r(\boldsymbol{v}, \boldsymbol{u}(\boldsymbol{v})) = 0$

  solve adjoint problem

  $\frac{dF_L}{d\boldsymbol{X}_i}, \frac{dg_L^j}{d\boldsymbol{X}_i}, \frac{dF_L}{d\boldsymbol{t}_i}, \frac{dg_L^j}{d\boldsymbol{t}_i}$

  map thickness sensitivities to thickness control space

  $\frac{dF}{\boldsymbol{d\tau}} = \frac{dF}{d\boldsymbol{t}}\frac{d\boldsymbol{t}}{d\boldsymbol{\tau}} = \frac{dF}{d\boldsymbol{t}}\frac{d\Lambda}{d\boldsymbol{\tau}}$

  $\frac{dg_L^j}{d\boldsymbol{\tau}} = \frac{dg_L^j}{d\boldsymbol{t}}\frac{d\Lambda}{d\boldsymbol{\tau}}$

  assemble sensitivity vector

  $\frac{dF}{d\boldsymbol{v}} = \begin{bmatrix} \frac{dF_L}{d\boldsymbol{X}} \\ \frac{dF_L}{d\boldsymbol{\tau}} \end{bmatrix}, \frac{d\boldsymbol{g}}{d\boldsymbol{v}} = \begin{bmatrix} \frac{d\boldsymbol{g}_L}{d\boldsymbol{X}} \\ \frac{d\boldsymbol{g}_L}{d\boldsymbol{\tau}} \end{bmatrix}$

  calculate mapping matrix

  $\boldsymbol{A} = \frac{d\boldsymbol{X}}{d\boldsymbol{s}}$

  map sensitivities to Vertex Morphing control space

  $\boldsymbol{s} = \begin{bmatrix} \boldsymbol{s_X} \\ \boldsymbol{s_\tau} \end{bmatrix}$

  $\frac{dF}{d\boldsymbol{s}} = \frac{dF}{d\boldsymbol{v}}\boldsymbol{A}, \frac{d\boldsymbol{g}}{d\boldsymbol{s}} = \frac{d\boldsymbol{g}}{d\boldsymbol{v}}\boldsymbol{A}$

  calculate desired step-size ratio $Q^\star = \frac{d_{s_X}}{d_{s_\tau}}$

  initialize $\mu_L = 10^{-5}, \mu_R = 10^5$

  evaluate Q_k^L, r_k^R with $Q_k = \frac{\|\boldsymbol{X}\left(\nabla_s^\mu F \boldsymbol{P} - \boldsymbol{C}_m(\boldsymbol{C}_m^T\boldsymbol{C}_m)^{-1}\boldsymbol{g}_a\right)\|_\infty}{\|\boldsymbol{T}\left(\nabla_s^\mu F \boldsymbol{P} - \boldsymbol{C}_m(\boldsymbol{C}_m^T\boldsymbol{C}_m)^{-1}\boldsymbol{g}_a\right)\|_\infty}$ for μ_L, μ_R

```
13
14  f(μ) = Q_μ^k(μ) − Q*
15  while Q_μ^k(μ) ≠ Q* do
16      evaluate sign
        s = f_L^k f_R^k / (‖f_L^k‖‖f_R^k‖)
17      if s < 0 then
18          initialize i = 0
19          while f(μ) ≠ 0 do
20              evaluate c = (f_L^k μ_R − f_R^k μ_L) / (f_L^k − f_R^k)
21              evaluate f_c^k which is f^k for μ = c
22              if f_c^k f_R^k > 0 then
23                  μ_R = c
24                  f_R^k = f_c^k
25                  if side == −1 then f_L^k /= 2;
26                  side = −1
27              else
28                  μ_L = c
29                  f_L^k = f_c^k
30                  if side == 1 then f_R^k /= 2;
31                  side = 1
32              end
33              f^k = f_c^k
34              i → i + 1
35          end
36      end
37  end
38  calculate design update by applying the step-size
     if ‖X p^k‖_∞ > ‖T p^k‖_∞ then
39      Δs^k = d_{s_x} p^k / ‖p^k‖_∞
40  else
41      Δs^k = d_{s_τ} p^k / ‖p^k‖_∞
42  end
43  calculate geometry and thickness update
    Δv^k = A^k Δs^k
    t = Λ(τ) = Λ(T b)
44 end
```

Chapter 4

Applications

In this chapter, a variety of applications taken from the design process of BMW are optimized with respect to different functional requirements. In the framework of such an industrial setting, even the simplest looking component is subject to a multitude of manufacturing, geometric and physical constraints, which have been conceptualized and brought into optimization with the abilities of our optimization software. The adequacy of the presented methods is put to test with respect to robustness and efficiency in the following paragraphs.

Every application conveys a different story on how optimization in the industry can be approached and tackled. Since in all cases a geometry already exists and has to be improved through optimization, especially in topology optimization, the initial conditions play a significant role. All use cases simulations are subject to implicit and explicit nonlinear loading. The linearization of the load-cases was an important part of the optimization, since it greatly affects the quality of the gradient information.

4.1 Cross member

In this industrial application, a cross member beam was optimized for transverse stiffness capacity. An important factor was manufacturability of the improved geometry with the deep drawing technique. To achieve this, the proposed undercut prevention constraint for Vertex Morphing, that is presented in chapter 3.1, was enforced to constrain the admissible shapes of the optimal design. Several aspects of the implemented optimization are explained in the following paragraphs.

Model description

The main function of the front-end cross member beam is the protection of the internal parts of the vehicle in low speed crash. The beam is connected to two crash boxes on both sides that dissipate energy in high speed front crash through deformation. A linearization of the low speed crash load case was achieved with the application of an equivalent force in the middle of the beam, as depicted if figure 4.1. The two crash boxes are fixed in place by fixing the nodes of the bolt holes. Finally, the model mesh density was refined in order to enable a higher degree of surface smoothness of the optimized design.

Optimization setup

Objective of the optimization is the maximization of the structural stiffness for the given load case. A comparison between an unconstrained optimization and a constrained optimization with the undercut response is made to investigate the effect of the geometric constraint on optimality. To further evaluate the constraint, a maximal angle of 75° was enforced, instead of the default 90°, for the undercut response function. The step size for every iteration was kept constant and relatively small at 0.5 mm. Since the mesh and loading is symmetric there was no need to use the plane symmetric formulation of Vertex Morphing (2.3.1). Finally, the edge nodes of the component were frozen during shape optimization due to connectivity to other assembly parts.

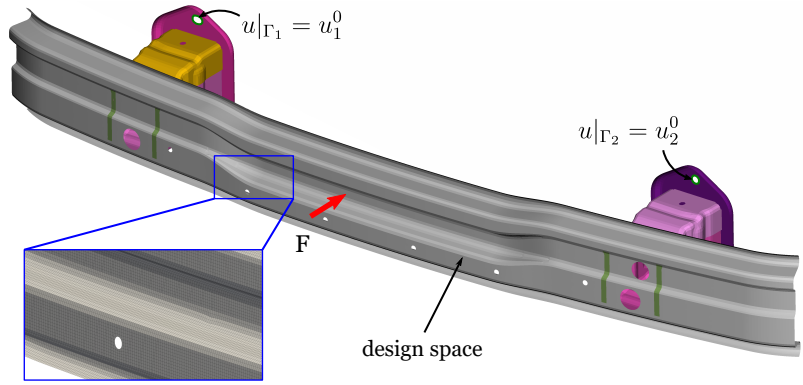

(a) Design space, in grey, for the optimization, mesh density of model and boundary conditions.

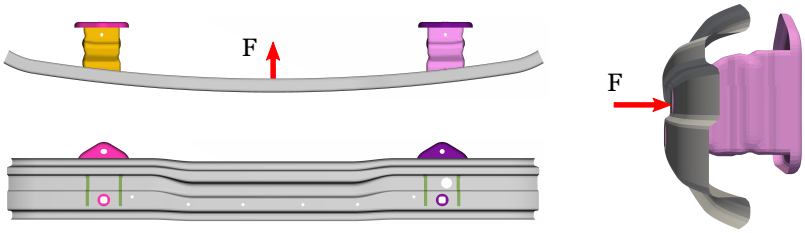

(b) Different views of front cross member computational model.

Figure 4.1 : Computational model of cross member.

Optimization results

Figure 4.2 illustrates the optimized designs for each performed optimization. It can be seen that the pattern and shape modes of the form update are similar for the unconstrained and both the constrained optimizations. This demonstrates the non-intrusive quality of the undercut response function, since it does not deflect from the path followed by the optimizer. It merely prohibits the undercuts and allows the algorithm to explore freely the feasible solution space. As a result, the approached local minima from the constrained and unconstrained optimizations have similar designs.

For greater clarity in the comparison between constrained and unconstrained optimizations, cross sections of the initial and improved geometries are plotted against each other in figure 4.4. It is apparent from both plots, that the undercuts of the unconstrained optimization are prevented and the the developed surface inclination is equal or smaller than the limit of 90° (top) and 75° (bottom).

The objective function evolution for the optimizations is illustrated in figure 4.5. Contrary to expectations, the constrained optimization with a 90° limit angle does not hinder the objective improvement when compared to the unconstrained optimization. On the contrary, the optimizer steers the geometry to a slightly stiffer design. A possible explanation is that the formation of the undercuts in the unconstrained optimization do not increase the stiffness of the structure and are a result of the sensitivity smoothing rather than the sensitivity information itself. The fact that a relatively large filter radius was used, larger than the bead depth in the initial design, points in this direction. This justification seems indeed reasonable also from an engineering perspective, since undercuts make the design more unstable under the prescribed loading. In the case of the constrained optimization with a 75° limit angle, the objective improvement is delayed significantly and only after around 20 iterations it begins to show signs of improvement. The bead draw angle in the initial design is 90°. Thus, the initial design lies in the infeasible space and the optimizer corrects in the direction of the undercut response gradient to push back to the feasible domain. This can be observed in figure 4.3, where the optimized geometries with the shape update length field are plotted. Regions 1, 2, 3 and their symmetric regions developed significant shape changes in order to attain a surface angle of 75°. On the other hand, the same regions in the unconstrained optimization (top) exhibit almost zero shape update. Therefore, this surface evolution does not improve the objective and is a result of the undercut response.

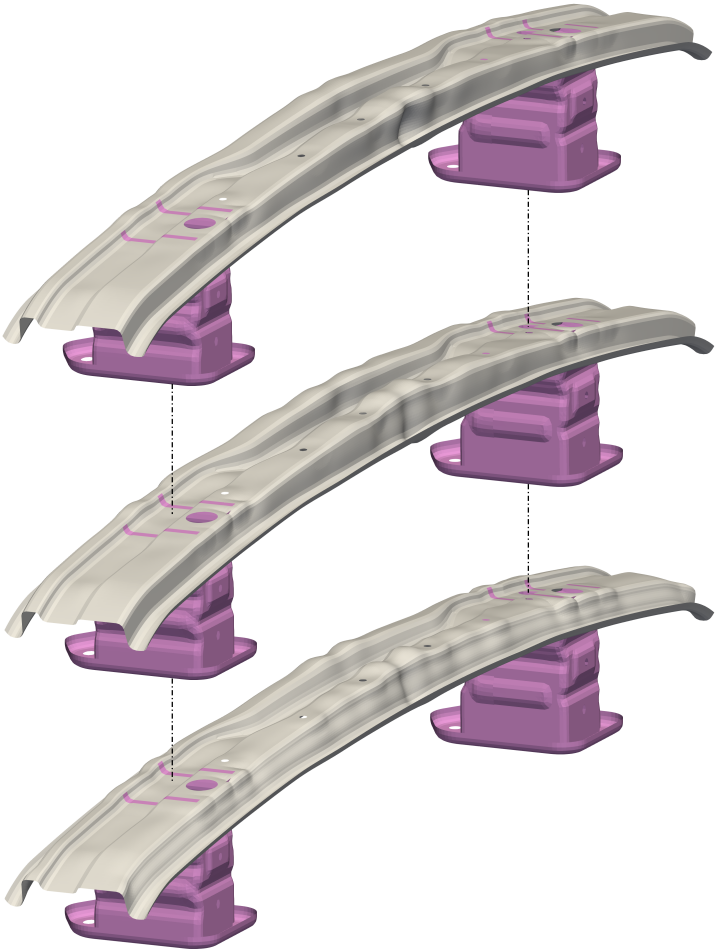

Figure 4.2 : Surface geometry of the model after unconstrained stiffness optimization (top), after optimization with the undercut constraint with a limit angle of 0° (middle) and with a limit angle of15°.

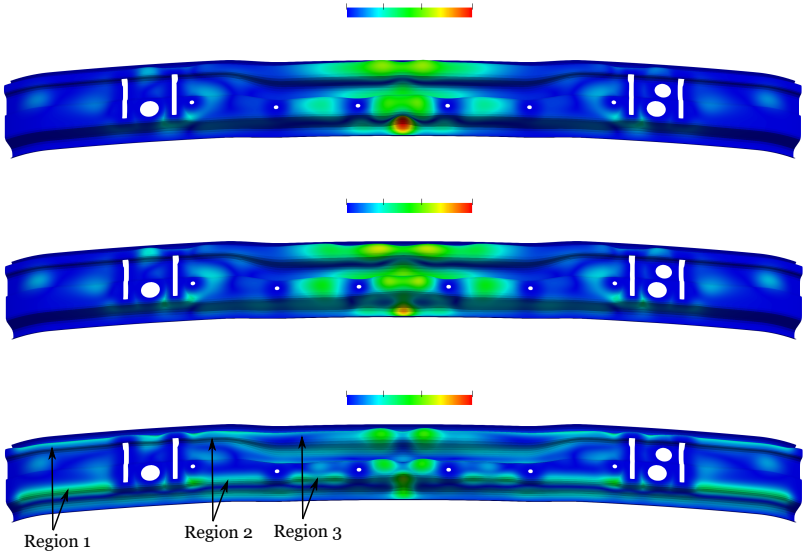

Figure 4.3 : Shape update length distribution after unconstrained stiffness optimization (top), after optimization with the undercut constraint with a limit angle of 0° (middle) and with a limit angle of15°. Blue indicates zero and red indicates the maximal value.

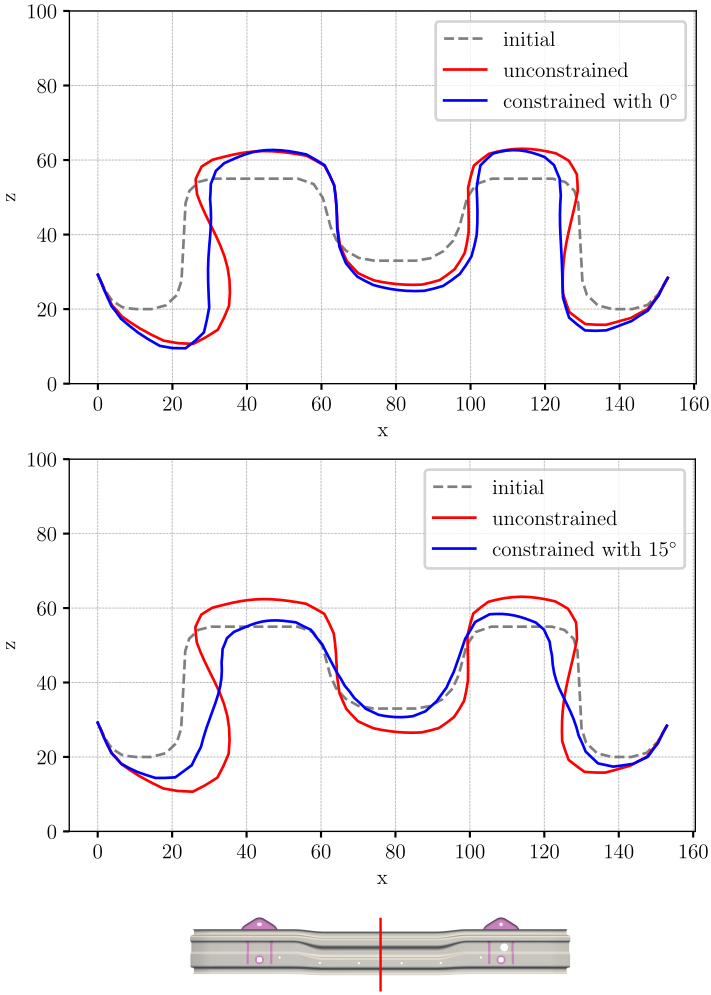

Figure 4.4 : Cross section profile comparison between initial design (grey), unconstrained optimal design (red) and optimal design with the undercut constraint (blue) with 0° (top) and 15° (bottom).

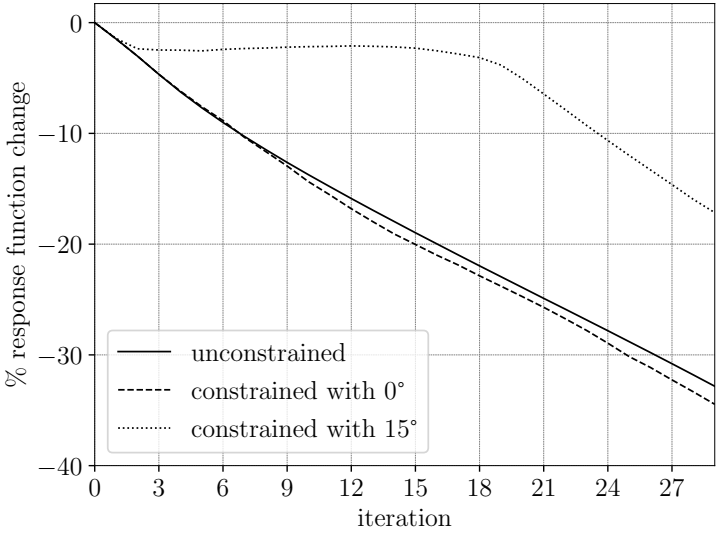

Figure 4.5 : Response function evolution comparison of unconstrained optimization and constrained optimization with 0° (top) and 15° (bottom).

4.2 Hood hinge system bracket

In this section, the successful multi-constraint optimization of a tailgate hinge system bracket will be presented. This application shows the capabilities and modularity of our software to handle models with solid elements and multiple constraints coming from different external solvers.

Model description

The tailgate model is subject to a number of static nonlinear load cases that ensure the structure's integrity during construction and during the service phase of the vehicle's lifetime. Important assessment values are the stiffness of the system and the maximal von Mises stress.

Due to the high computational cost of a full model simulation and its inherent nonlinearities, i.e., contact between assembly parts, the simulation model was reduced to only the hinge system bracket. In addition, since adjoint sensitivities are available from solvers only for linear static cases, the static nonlinear load cases were linearized in the following way: The bracket welding points' displacements under the nonlinear static analysis were applied as Dirichlet boundary conditions for a linear static linear analysis. The optimization was performed for three of those load cases, the von Mises stress of which are shown in figure 4.13(a). Figure 4.6 illustrates the bracket model and the surfaces where the boundary conditions are applied. The mesh density is variable and is higher in areas where larger shape updates are to be expected. A growth ratio larger than one was used for the volume meshing in order to reduce computational cost.

Optimization setup

The need for different solvers was born from the fact that not all response function sensitivity information is provided by one solver. Goal of the optimization was to minimize the weight of the bracket, subject to a geometric constraint with the application of an aggregate version of the Vertex Morphing packaging constraint, found in the literature [66], and strain energy constraints for each of the three load cases to their initial

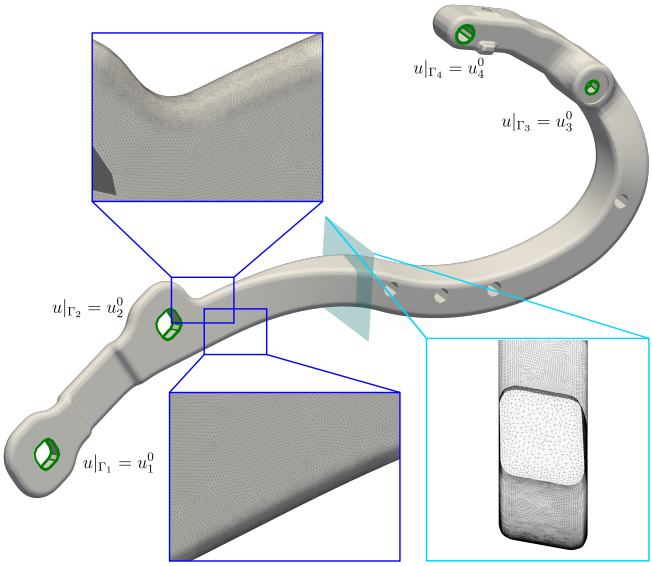

(a) Boundary conditions at initial geometry with surface mesh density and solid mesh density at selected cross section.

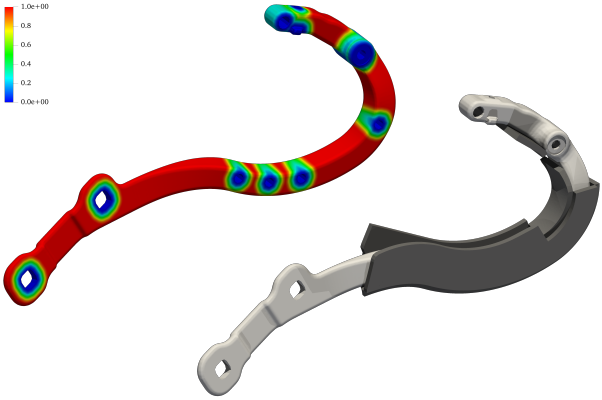

(b) Multiplication factor of the shape update in order to fix movement of boundary nodes (left) and the packaging geometry of the optimization (right).

Figure 4.6 : Computational model for the optimization of the the hinge bracket.

value using the formula:

$$C = \frac{1}{2}\boldsymbol{u}^T \boldsymbol{f} \tag{4.1}$$

$$= \frac{1}{2}\boldsymbol{u}^T \boldsymbol{K}\boldsymbol{u} \tag{4.2}$$

$$= \frac{1}{2}\int \boldsymbol{\epsilon}^T \boldsymbol{\sigma}\, dv \tag{4.3}$$

In the case where only Dirichlet boundary conditions are applied, the strain energy is a direct measure of the structural stiffness $\boldsymbol{K}$. In addition, a p-norm type black-box response function was used to constrain the maximal allowable von Mises stress, limited again at the initial value for each load case.

The notion of a control space in Vertex Morphing is ideally suited to handle the challenge of multiple solvers. The objective and constraint function gradients are mapped into the control space, as explained in chapter 2.3.1 and thoroughly in [49]. The search direction for the optimization is then calculated, and finally the shape update is mapped back to all geometries. Provided that the Vertex Morphing filter radius is larger than the minimum required for a smooth shape update, non-matching meshes of different mesh densities are updated with minimal geometric deviation from each other. The surface discretization of solver 1 and solver 2 is shown in figure 4.7. The geometric constraint needs to

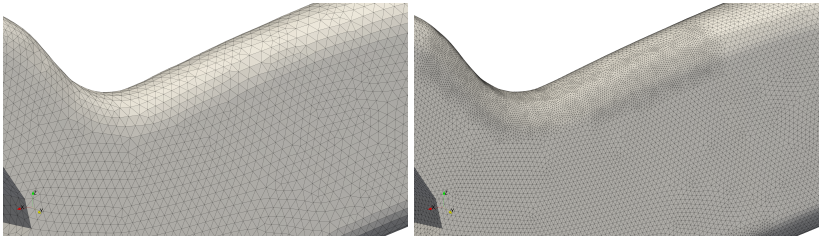

Figure 4.7 : Surface disretization of Solver 1 (left) and Solver 2 (right).

be applied only on one of the meshes, since fulfillment of a constraint in the control space guarantees its fulfillment in all destination geometries.

4.2.1 Automatic solid mesh motion

When shape optimizing components modeled with a solid mesh, one has to make sure that after every surface shape update the internal nodes of the mesh also follow. Otherwise, after a few iterations the analysis will fail because of collapse of the faces of the solid elements. In addition, the mesh quality has to be preserved, especially at regions with distorted elements. There are different approaches for the mesh motion, well documented in literature, and the problem is especially prominent in CFD optimization. The motion of the internal solid nodes is determined by solving the equations of linear elasticity (without inertial terms) with variable Young Modulus on the solid elements. This solution method is similar to that of [53], where the solution of the Laplace equation with variable diffusion is used. Both are second order elliptic partial differential equations, such that although the physical interpretation of the unknown variables differ, the mathematical problem is essentially identical. The shape update of the surface nodes is applied as a displacement boundary condition for the solution of the problem. As observed in 4.6(a), a volume growth rate larger than one was used for meshing the geometry in order to reduce mesh density. Mesh quality and accuracy of the solution are more important closer to the surface. Three different Young Modulus laws were used, all distance-based. The Young Modulus E_i of element i is a function of the element's centroid P_i^c nearest distance $d_{P_i^c-\Gamma}$ from the surface Γ:

- $E_i = \frac{1}{\sqrt{d_{P_i^c-\Gamma}}}$; sublinear dependence
- $E_i = \frac{1}{d_{P_i^c-\Gamma}}$; linear dependence
- $E_i = \frac{1}{d^2_{P_i^c-\Gamma}}$; quadratic dependence

The comparison between the different mesh motion rules follows in the next paragraph.

The optimization design space is input as a node set from the user and, to their convenience, is part of the domain whose nodes are free

to move, either due to optimization shape update or automatic mesh motion. Figure 4.8 illustrates the problem definition. Design space for the shape optimization is the right half of the geometry in dark grey. Γ_{sf} denotes the nodes and elements that lie on the surface of the design space. Γ_b is the interface surface between design and nondesign space. For the shape optimization problem, the nodes and elements in Γ_{sf} are also considered surface nodes and elements, since our optimization software only inputs information about the design space. Hence, the equation $\Gamma = \Gamma_{sf} + \Gamma_b$ holds. As Ω_{sl} are defined the solid nodes and solid elements. Sensitivity information on non-surface nodes is meaningless

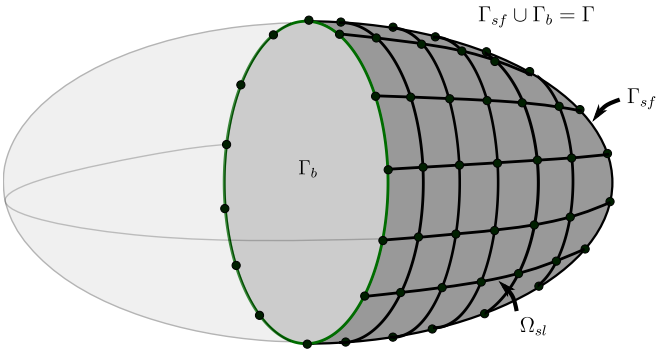

Figure 4.8 : Schematic of a solid 3D geometry for shape optimization. Design space for the optimization problem is the right half of the structure in dark grey.

since response function changes only come from updating the external surface of the geometry. Thus, design space is reduced to only surface nodes (Γ_{sf}) in order to further reduce numerical cost. Naturally, integral part of the procedure is the identification of surface nodes and creation of surface triangle elements. The following algorithm is specific to the case of tetrahedral-only meshes but can be easily generalized for other solid elements such as hexahedra or pyramids. A node X_i is solid when the following condition holds:

$$N_{X_i}^F = \frac{3N_{X_i}^E}{2} \tag{4.4}$$

where $N_{X_i}^F$ is the number of faces of the tetrahedra whose vertices include X_i, and $N_{X_i}^E$ is the number of neighboring tetrahedra of node X_i. This is

a generalization of the surface mesh edge detection rule, where a node X_i is an internal, and not an edge, node if the following condition holds:

$$N_{X_i}^N = N_{X_i}^E \tag{4.5}$$

where $N_{X_i}^N$ is the number of the neighboring nodes of node X_i and $N_{X_i}^E$ defined as above. Here, $N_{X_i}^N$ can also be seen as number of edges attached to X_i. In turn, extrapolating from 2D to 3D, edges become faces and 2D elements become 3D elements leading to 4.4. Figure 4.9 visually clarifies this equation. Looking at the right graph, the faces connected to the solid node X_i are exactly $3N_{X_i}^E$ (three faces for every neighboring element). Going back to the right graph where the neighboring elements are bordering with each other, every face is shared by exactly two tetrahedra. By dividing with 2 we reach the equality of 4.4. Finally, the faces of

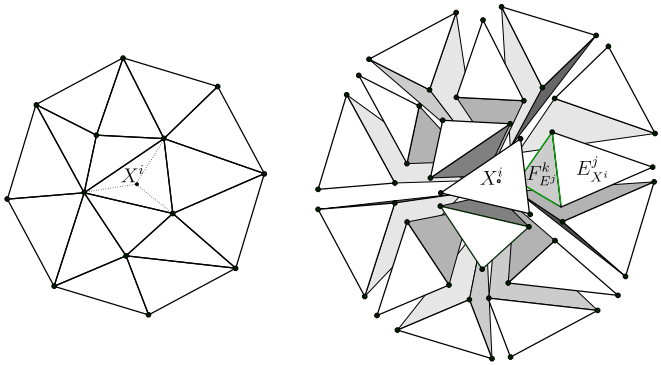

Figure 4.9 : Schematic visualization of the neighboring tetrahedra of a solid node with connected faces (left) and with disconnected ones (right).

the tetrahedra that are shared by only one element are used as triangle surface elements for the optimization model. The pseudocode of this automatic tetrahedral mesh motion is described in algorithm 4.1.

Optimization results

The optimal shape design is shown in figure 4.11. The solution space was explored using a filter radius smaller than the width of the bracket. This

Algorithm 4.1: Shape optimization with automatic tetrahedral mesh motion.

```
Read geometry Ω from input file
//Detect element neighbors of nodes
foreach node X_i in Ω do
    find e^{X_i}_{nghbr} = [...]
end
//Detect surface nodes
foreach node X_i in Ω do
    N^F_{X_i} = 0 foreach e_j in e^{X_i}_{nghbr} do
        foreach F_k in e_j do
            if not added then
                N^F_{X_i} += 1
            end
        end
    end
end
//Create surface elements
//Read boundary nodes and elements
//Start optimization loop
for i = 1,2,... do
    //Solve state and adjoint problem
    //Calculate search direction vector s
    //Calculate shape update vector δx
    //Calculate Young Modulus E for mesh motion
    foreach element e_i in Ω_sl do
        E_i = 1 / d^2_{P_i^c − Γ}
    end
    //Write input file for mesh motion
    //Solve state problem for mesh motion and get d_sl
    //Update surface nodes with δx
    //Update solid nodes with d_sl
end
```

was intentional in order to let the two opposite surfaces of the bracket to develop unaffected from each other. The thickness of the bracket is thus free to increase in some areas and decrease in others. The bottom and top surface become much thicker in order to support the in-plane and out-of-plane loading and the middle part of the bracket thins out in favor of mass reduction. The optimal cross sections, as shown in figure 4.12(b), are similar to the cross section of an I-beam which is excellent for unidirectional bending and shear loading while being cost-effective since material is not excessively used. The cross-sectional area of slice α increases with our shape optimization while for slice β there is a reduction and for γ an even larger one. Material is needed closer to the hole where the bracket is screwed with the rest of the structure and the boundary conditions are applied.

The absolute percentile change of the response functions is shown in the graph 4.10. The mass reduction is around 22% and the constraints of strain energy and von Mises stress remain almost constant with minimal violation. Figure 4.13 shows the von Misses stress distribution before and after optimization. The maximal values for all three load cases remain similar but the distribution has slight changes. Since the material is used optimally after optimization, there are larger areas with greater stresses than before.

Finally, a comparison between the three different distance-based Young Modulus rules for the automatic mesh motion is illustrated in figure 4.14. The applied rule greatly affects the solid mesh quality during optimization, which in turn also affects the response function values, especially for the von Mises stress which is a measure of the observed shearing. The chosen applied rule seems to also be case-specific. For CFD applications where the fluid domain is very large compared to the structure moving in it, the inverse quadratic distance rule is more suitable since regions far away from the fluid-structure boundary are of rather small interest and a deformed mesh there has minimal effect on the solution. In the case of the bracket, when raising the distance to an exponent equal or larger than -1 (such as in the second and third rule of 4.2.1), the elements around the center of gravity get squeezed and stretched as can be seen in the two rightmost columns of figure 4.14. This is due to the abrupt reduction of Young Modulus in short distances

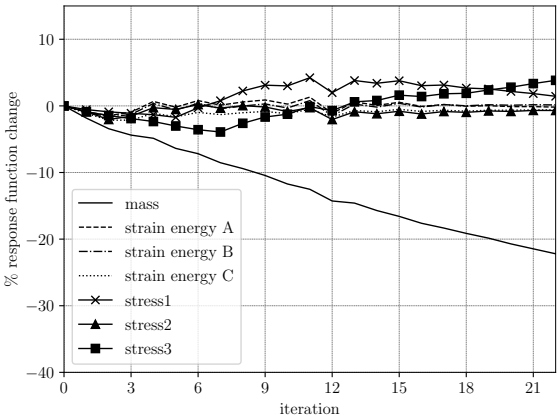

Figure 4.10 : Absolute percentile change of objective (mass) and constraint functions during optimization.

Figure 4.11 : Optimal design from opposing views.

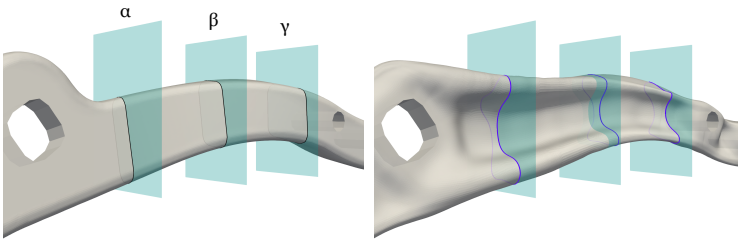

(a) Cross sections on initial geometry (left) and cross sections on optimal geometry (right).

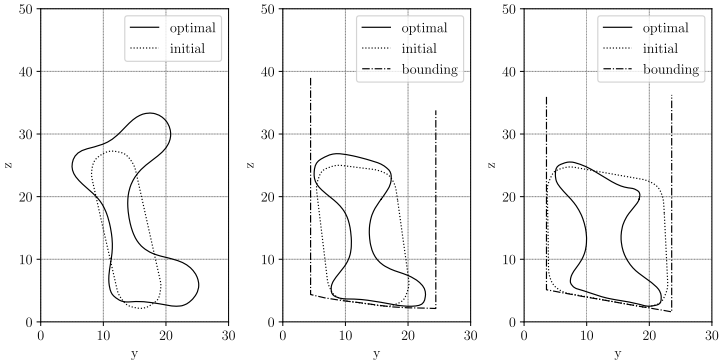

(b) Cross section α (left), cross section β (middle) and cross section γ (right).

Figure 4.12 : Initial and optimal selected cross sections.

from the surface. The first rule is more appropriate and leads to better mesh quality and failure at a much later optimization iteration without re-meshing.

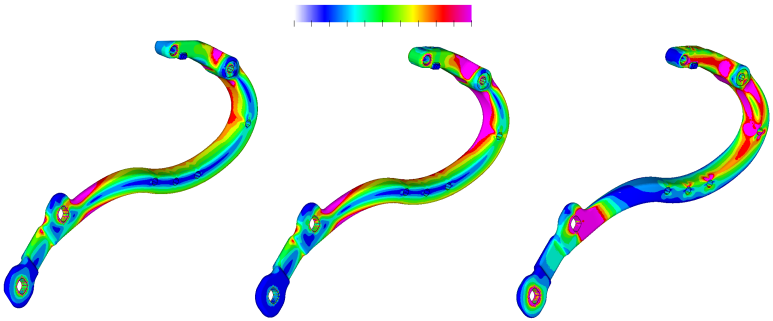

(a) Von Mises stress component for the three loadcases of the hood hinge-system for the initial design.

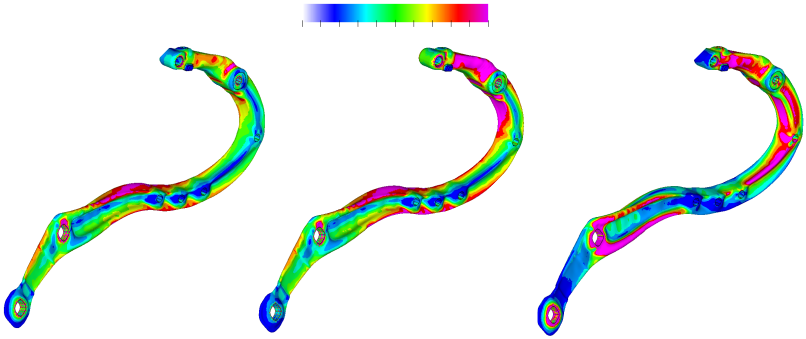

(b) Von Mises stress component for the three loadcases of the hood hinge-system for the optimal design.

Figure 4.13 : Von Mises stress components for three loadcases (from left to right) for initial (top) and optimal (bottom) geometry.

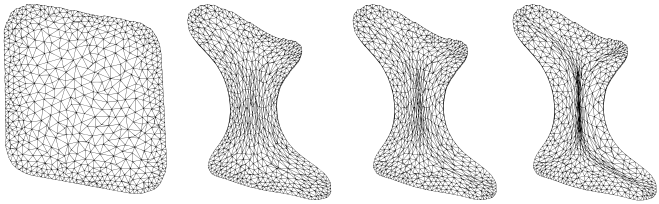

(a) Cross section α for initial geometry (far left) and optimal geometry with square root law (second from left), linear law(second from right) and quadratic law (far right).

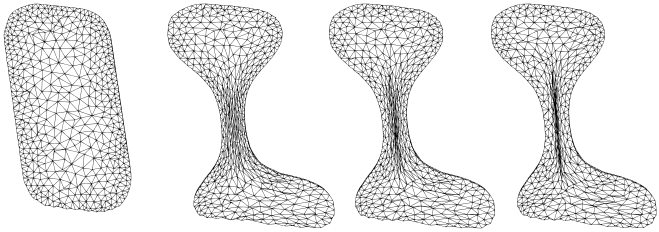

(b) Cross section β for initial geometry (far left) and optimal geometry with square root law (second from left), linear law(second from right) and quadratic law (far right).

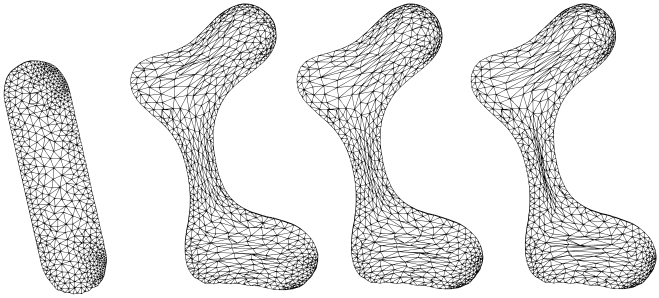

(c) Cross section γ for initial geometry (far left) and optimal geometry with square root law (second from left), linear law(second from right) and quadratic law (far right).

Figure 4.14 : Influence of Young Modulus law on mesh quality for cross sections α (top), β (middle) and γ (bottom).

4.3 Front-end shear panel

This application is another example of mass minimization with Vertex Morphing. This time though, the simultaneous shape and topology optimization formulation was applied to verify its capabilities in industrial cases. Important aspects of this application will be explained in the next paragraphs.

Model description

The front-end shear panel is an aluminum shell structure that serves to stiffen the front part of the car during the operational phase. It plays an important role in anti-symmetric torsional loading that takes place when the vehicle is steered to the left or to the right. The enforced design of the front-end shear panel is illustrated in figure 4.15. It can be seen that beads are impressed on the middle area of the shear panel. This is a technique that aims to increase the structural stiffness of the part. In the current design process, this technique is based on the experience and functional understanding of the designer or engineer. As it is not a result of some type of optimization, it is sub-optimal and a trial and error approach is applied in order to find an acceptable design. Evidently, this leads to many loops between design and simulation analysis, something that can be avoided with the use of mathematical optimization.

The load cases of our computational model are the following: loading applied during the assembling of the aluminum sheet with the rest of the front-end components, and an anti-symmetric torsional loading of the sheet during left turns of the vehicle. Both loads are applied in the context of a linear static analysis of the full vehicle. Naturally, this is a costly analysis and and optimization would take many days. In an attempt to reduce the optimization overall time, the same method as in the Bracket example of chapter 4.2 is applied: the model is reduced to only the shear panel, and its displacement field after the car body simulation is enforced as a boundary condition.

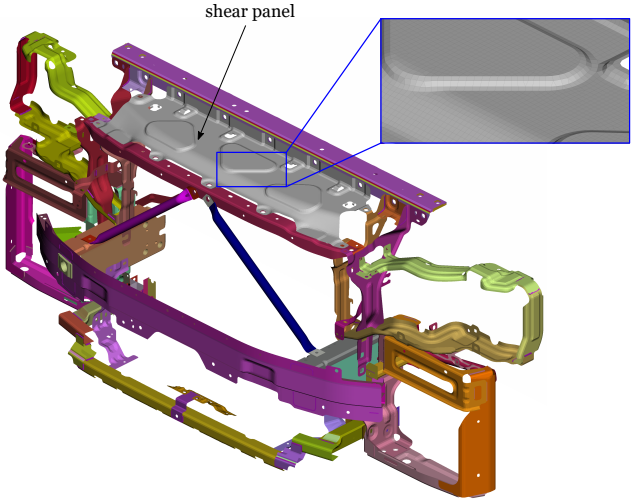

(a) Front-end geometry of the car including the shear panel and the bounding geometries around it used in the optimization.

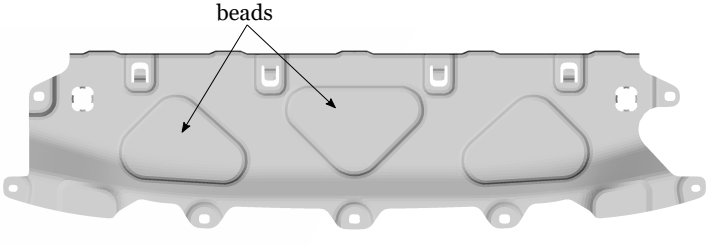

(b) The current design of the shear panel with the stiffening beads.

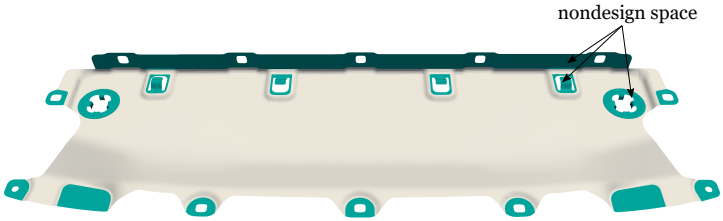

(c) Leveled shear panel geometry used as a starting point for the optimization. In grey the design space.

Figure 4.15

Optimization setup

For shape optimization, as opposed to topology optimization, there has to be an initial design that is to be improved. Logically, that initial design also affects the end result of the optimization and can have a great effect on its optimality. So that we can minimize the influence of the beaded design, it was decided to remove the beads and flatten the geometry out, such that the optimization starts from a leveled geometry, as depicted in figure 4.15(c). The existing mesh was refined by 2.5 times so that a smaller radius can be used and smaller shape modes can be exploited. The vertical flange and the areas around the connection points with other geometrical parts were left out of the design space so that the optimal design can be used for recalculation and validation in the full-body computational model.

As mentioned in the introductory paragraph, objective of the optimization was the reduction of mass. The solution space was constrained in that strain energies for both load cases should be equal or better to the strain energies of the beaded design (which is naturally stiffer than the leveled one). In addition, the mirror symmetry Vertex Morphing mapping of chapter 1 was applied and the internal packaging response function of our software. The leveled shear panel offset in direction $+z$ and $-z$ by $10\,mm$ was used as bounding surface for the geometric constraint.

4.3.1 Comparison study of optimization approaches

In an attempt to investigate and study the differences between the proposed simultaneous shape-topology optimization formulation and the existing wide-spread optimization processes for weight-minimization, it was decided to perform a series of optimization approaches for this application:

- Shape optimization followed by a design thickness reduction.
- A serial optimization approach where a shape optimization of the initial design is followed by a topology optimization.

- A serial optimization approach where a topology optimization of the initial design is followed by a shape optimization.
- A staggered optimization approach where in every iteration a shape and topology optimization problem are solved independent to each other.
- A simultaneous optimization with the unified shape and topology optimization formulation proposed in this thesis.

In order to conduct an unbiased comparison study, the structural stiffness of all optimal designs was intended to be equal and was controlled through the constraint limit. The main comparison criteria were the reduction in mass, the ease of use, and the overall computational efficiency of the process.

The first approach is commonly employed in industrial environments. A shape optimization minimizes compliance until convergence and, subsequently, structural thickness is reduced until compliance drops to the desired limit. Naturally, there are manufacturing constraints regarding minimum sheet metal thickness which make this approach often impractical. In addition, it has to be taken into account that structural thickness influences the formability and manufacturability of the component. Even though results are far from optimal, the approach is listed for the sake of completeness.

In the case of the serial optimization approaches, the rationale is that unconstrained shape optimization is a powerful tool to increase the structural stiffness of a component, and that topology optimization is the best way to achieve mass reduction for a given stiffness limit. It can be argued that mass reduction could be also achieved with a shape optimization where nodal mass sensitivities are used to steer the design towards a direction that both minimizes the weight and increases the stiffness. This has been observed, after all, in the bracket application of section 4.2. For solid meshes it is indeed true. In the case of a shell structure, shape optimization can minimize the mass through shrinking and flattening of the surfaces. However, this is restrictive for most industrial cases where the edges of a design are neighboring with other

parts and have to be frozen during optimization. Moreover, it prohibits the formation of beads that increase structural stiffness.

Thus, in the first serial approach the structure is firstly shape optimized to maximize its stiffness while its mass is kept almost constant. Shape optimization is stopped either when convergence of the objective function is achieved, or when mesh quality is deteriorated by element distortion. Subsequently, a topology optimization reduces mass as much as possible for a compliance constraint fraction equal to the ratio between the desired and initial compliance of the shape optimized design. Similarly, in the second serial approach mass is reduced as much as possible and then structural stiffness is maximized until convergence or mesh quality deterioration. A first obvious difficulty during the serial approaches is the selection of the constraint and objective values for which to aim for before moving on to the next optimization type.

The staggered optimization approach is similar to the proposed simultaneous shape topology optimization, except for the fact that shape and topology optimization act independently from each other on the same geometry at every iteration step.

Finally, the simultaneous approach has already been extensively presented and discussed in chapter 3.3.

Optimization results

The results of the first approach are summarized in table 4.1. The maximum mass reduction for which the stiffness limit is satisfied is about 11%. The objective function evolution during shape optimization can be seen in figure 4.19. It is interesting to note that stiffness change is almost linear to thickness change after shape optimization. This can be explained by the fact that shape optimization changes the load-paths so that the structure goes under tension and compression, mechanical load-bearing modes more efficient in comparison to bending.

Starting with the first serial approach, the initial topology optimization of the starting design was executed for 150 iterations until convergence was achieved. The compliance constraint limit was selected so that mass

Table 4.1 : Summary of response function percentile change for the first two optimization approaches.

thickness decrease after shape optimization			
thickness	% initial mass	compliance %	% compliance to limit
1.0	100.0	100.0	116.4
0.91	93.1	91.2	106.1
0.875	89.7	86.6	100.8
0.83	86.2	82.0	95.5

reduction is as large as possible, while the subsequent shape optimization can successfully converge at the desired stiffness value despite geometric constraints. Hence, finding the correct constraint values might require a few unsuccessful optimizations and a lot of experience, since constraint relaxation does not affect objective improvement linearly. Fig. 4.16(a) depicts the thickness distribution (top) and the percentile change of the response function of the topology optimization. Subsequently, a geometrically constrained shape optimization is executed until mesh distortion reaches unacceptable levels, which takes about 250 iterations. The objective evolution is shown in figure 4.16(a). Note in 4.16(b) that the contour of the voids changes slightly both in- and out-of-plane because of the structural shape optimization, thus marginally changing the final mass.

In the second serial approach the order of topology and shape optimization is reversed: shape optimization comes first with a goal of stiffening the structure, followed by topology optimization to reduce the mass. The idea here is to let shape optimization increase the stiffness more than the desired value, such that when topology optimization later takes place, the stiffness is compromised to the chosen limit. After 250 shape optimization iterations an improvement of approximately 230% is observed (fig. 4.19). Figure 4.18(a) illustrates the shape-optimized design. It can be seen that the regions where larger shape updates are observed are the same during shape optimization of the topology-optimized design of the first approach. Furthermore, it is also noteworthy to highlight that shape optimization on the initial design improves the objective func-

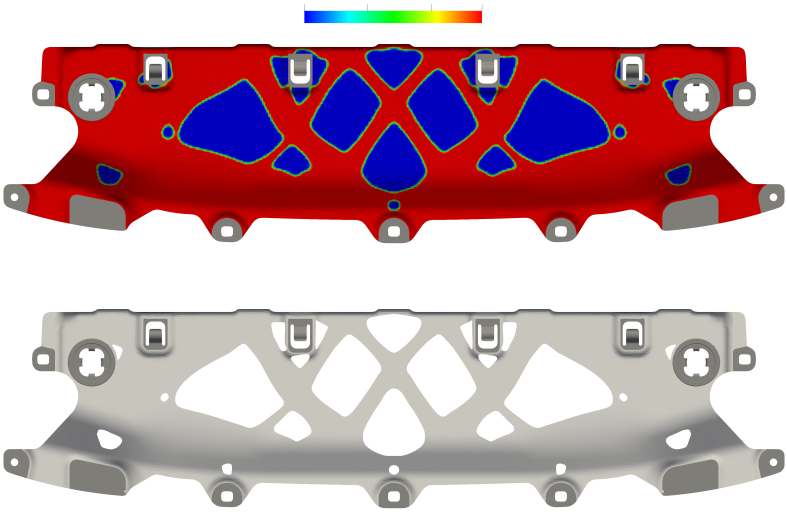

(a) Distribution of sheet-thickness after topology optimization (top) and design after hole-cutting with a commercial pre-processing software (bottom).

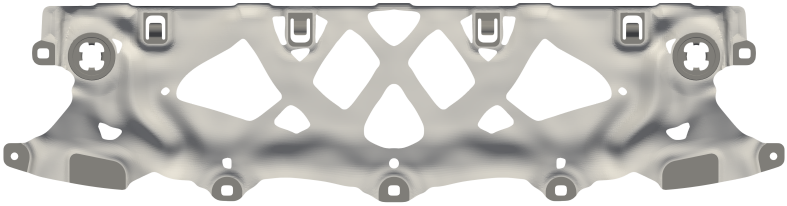

(b) Optimal design after shape optimization of the above topology-optimized geometry.

Figure 4.16 : Resulting optimal designs of the first serial approach optimization.

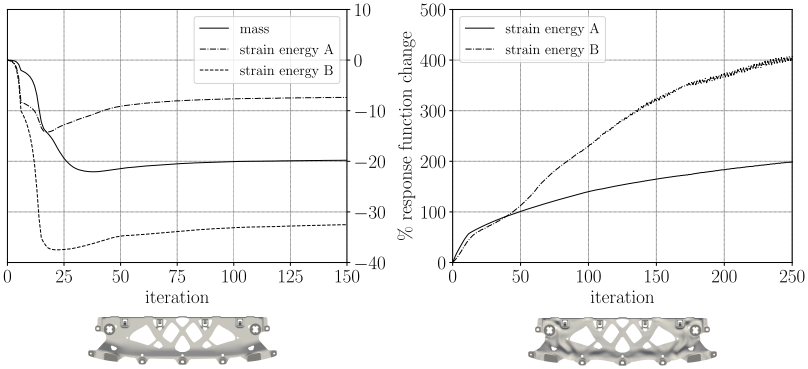

Figure 4.17 : Objective and constraint response function evolution for shape optimization (left) and topology optimization (right) of the first serial optimization approach.

tion slightly more than on the topology-optimized design. Afterwards, topology optimization is executed and yields the thickness distribution of figure 4.18(b). Even though total mass reduction is almost the same (Fig. 4.19) in comparison to the first serial method, the void pattern and size are quite different. This servers as a reminder to the nonlinear and non-convex nature of a topology optimization problem where infinite local minima exist. During the subsequent topology optimization convergence is achieved in about 150 iterations, which is the same as in the topology optimization of the first approach.

The third approach differs in that the two types of structural optimization are executed concurrently in every iteration of the optimization but are uncoupled from each other. The justification here is that by updating both the shape and thickness distribution in every optimization iteration, the order of the optimization types will not affect the results, as we have seen above. Since our topology optimization formulation uses a binary starting point (all design variables start with the maximal thickness value), the design variables can only move unidirectionally and become smaller, forming the void areas and reducing the weight. It is therefore infeasible to stiffen the design through our topology optimization formulation and this is left merely to the shape optimization. Figure 4.20(b) illustrates that even though both strain energy constraints are satisfied

(a) Optimal design after shape optimization of leveled design.

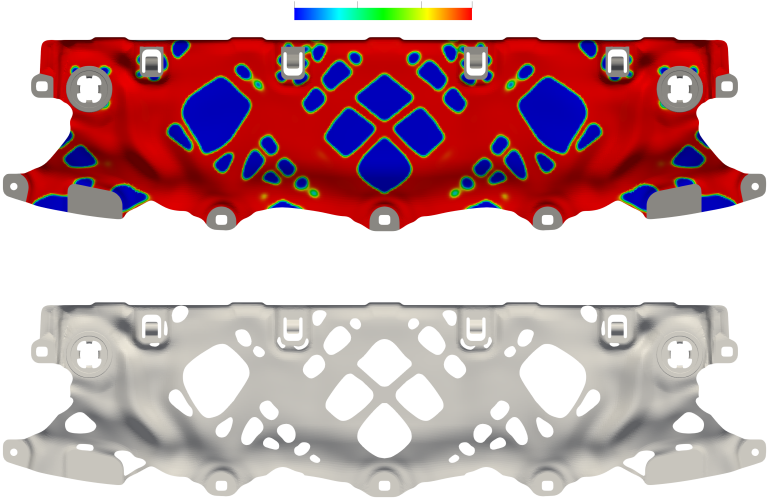

(b) Distribution of sheet-thickness after topology optimization of the shape-optimized design of above figure (top) and design after hole-cutting with a commercial pre-processing software (bottom).

Figure 4.18 : Resulting optimal designs of the second serial approach optimization.

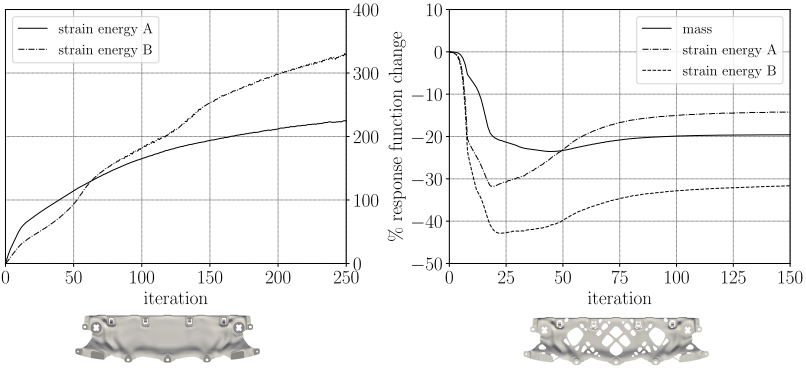

Figure 4.19 : Objective and constraint response function evolution for shape optimization (left) and topology optimization (right) of the second serial optimization approach.

from the shape and thickness updates, the mass is not being reduced. The reason for this is that the uncoupled sensitivities do not work collaboratively and the constraints are enforced twice on the problem: once for the shape and once for the topology optimization. Namely, while the constraint values are zig-zagging around their limits, as expected with the gradient projection algorithm, topology and shape optimization are trying simultaneously and separately from each other to update the design variables in a direction that satisfies the constraints and improves the objective function. Thus, void areas are not formed (figure 4.20(a)) and thickness design variables oscillate aimlessly without resulting in mass reduction. As expected, shape and thickness sensitivities have to work synergetically in order for the optimization to be successful.

For the simultaneous shape and topology optimization formulation proposed in this thesis, two different setups are investigated: one in which the nodal shape sensitivities with respect to mass are excluded from the optimization, and one in which they are included. In the first case, the mass objective function is differentiated only with respect to the thickness design variables. The motive here is to investigate the quantitative and qualitative effect of the shape mass sensitivities on the optimization outcome. Both optimizations were executed for 200 iterations with a

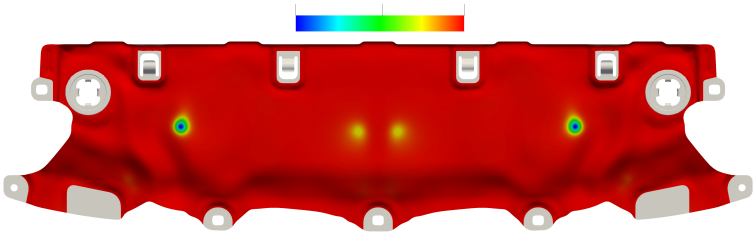

(a) Step-wise serial optimization resulting shape update and thickness distribution.

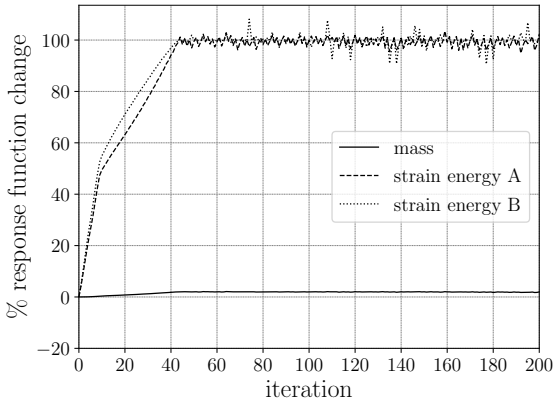

(b) Mass objective function and strain energy constraints evolution for topology optimization of step-wise serial approach.

Figure 4.20 : Results of step-wise serial approach optimization.

ratio between shape and thickness update equal to 10 (maximal shape update was 0.7 mm and maximal thickness update was 0.07 mm). As expected, the inclusion of mass shape sensitivities affects the optimal design of the converged optimization. Chosen cross-sectional surface cuts of the initial and optimal geometries are shown in figure 4.24. Discontinuities in the slices of the optimal designs are due to hole openings. It can be seen that the optimal design of the optimization with only thickness sensitivities of the objective function shows a larger total shape update that the one with both shape and thickness sensitivities. This can be attributed to the fact that mass shape sensitivities of non-edge

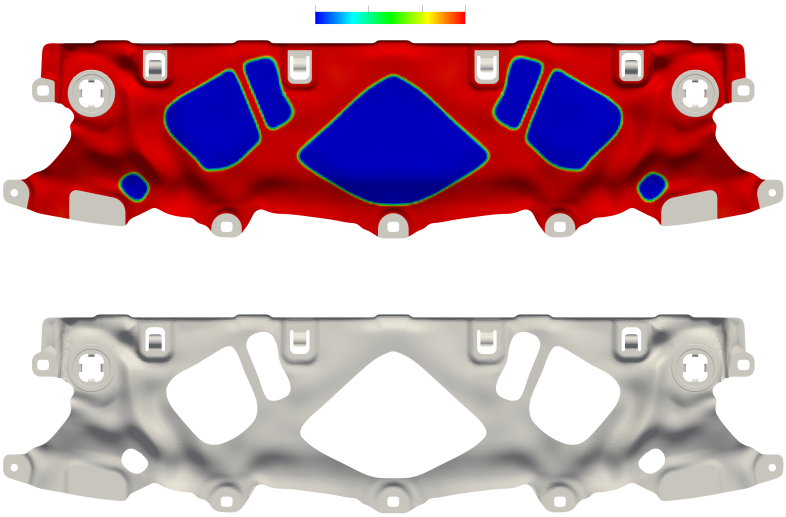

(a) Simultaneous shape and topology optimization optimal design with thickness distribution (top) and with holes cut open (bottom).

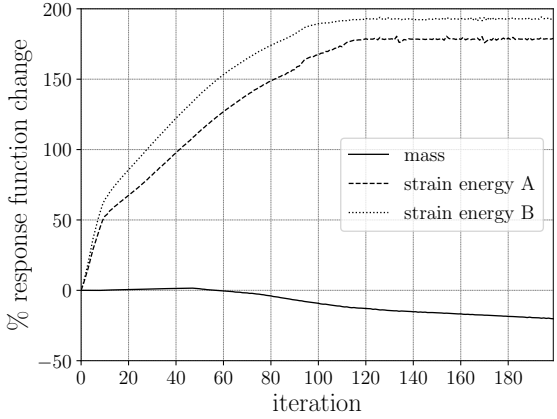

(b) Mass objective function and strain energy constraints evolution for simultaneous shape and topology optimization.

Figure 4.21 : Results of simultaneous shape and topology optimization with mass objective function constant with respect to thickness design variables.

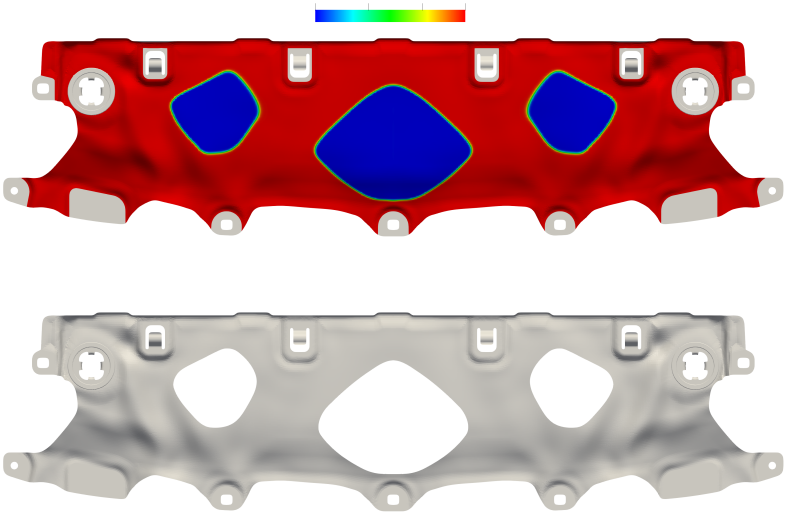

(a) Simultaneous shape and topology optimization optimal design with thickness distribution (top) and with holes cut open (bottom).

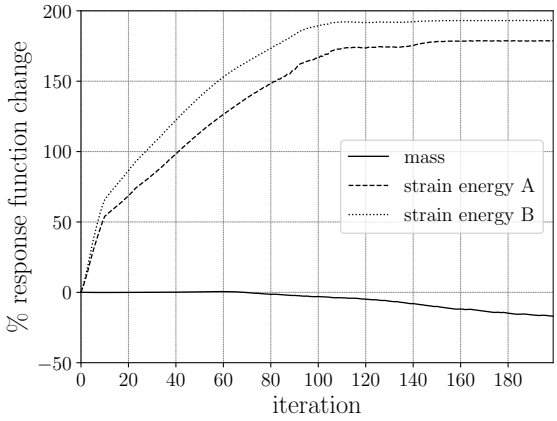

(b) Mass objective function and strain energy constraints evolution for simultaneous shape and topology optimization.

Figure 4.22 : Results of simultaneous shape and topology optimization with mass objective function variable with respect to thickness design variables.

nodes point towards a direction that flattens the shell structure in order to minimize surface area. Comparing the contours of the two designs in figure 4.23, it can also be observed that shape mass sensitivities tend to update the shape of the edges towards the in-plane direction, with intention to shrink the whole structure. In order to compensate for the structural stiffness lost due to the lack of freedom for sufficient out-of-plane shape update, the void size from topology optimization tends to be smaller for the same number of iterations. If the optimization with included mass shape sensitivities is executed for 10 to 30 more iterations, the final weight reduction will be similar for both optimizations. It is therefore interesting to be noted, that the inclusion, or not, of mass shape sensitivities can be used as a design-handle from the engineer in order to steer the optimization towards an optimal geometry that has desired geometric features.

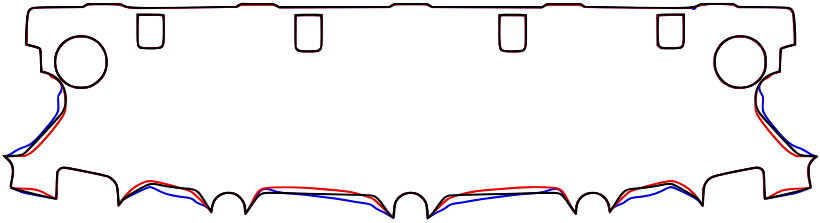

Figure 4.23 : Contour of initial shape (black) vs. optimal shape with mass shape sensitivities (blue) and without mass shape sensitivities (red).

Last but not least, the optimal shear-panel designs from both simultaneous optimizations were put in place of the beaded shear-panel design in the full car-body computational model in order to validate the results of the sub-model optimization. Figure 4.25 compares the displacement plots of the car-body torsional simulation analysis for the initial and optimized designs. Finally, table 4.2 summarizes the percentile change of the strain energy for all car-body simulation load-cases, proving that the sub-model optimizations were successful.

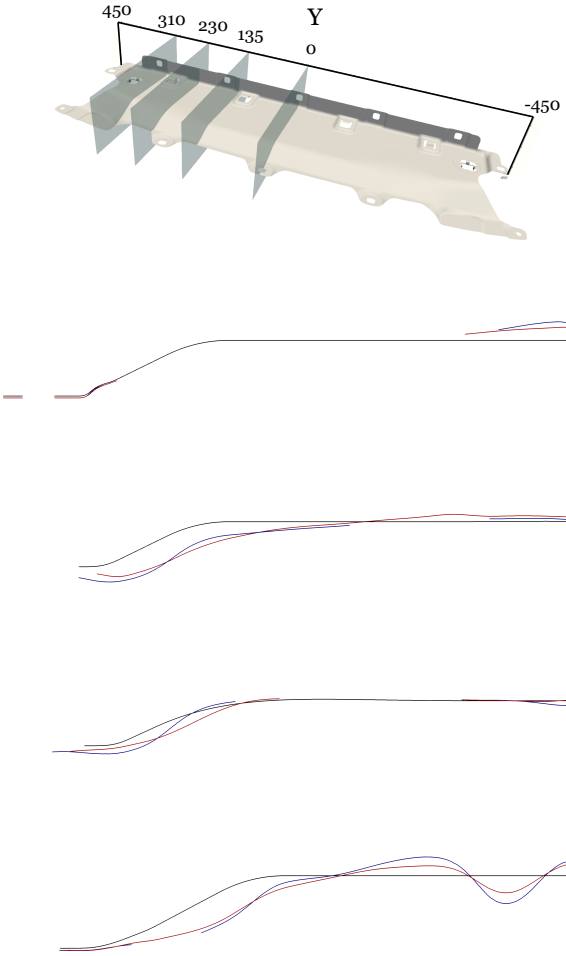

Figure 4.24 : Cross sections along the width of the structure starting from $Y = 0$ (top) towards $Y > 0$ (bottom). Initial shape (black) vs. optimal shape with mass shape sensitivities (blue) and without mass shape sensitivities (red).

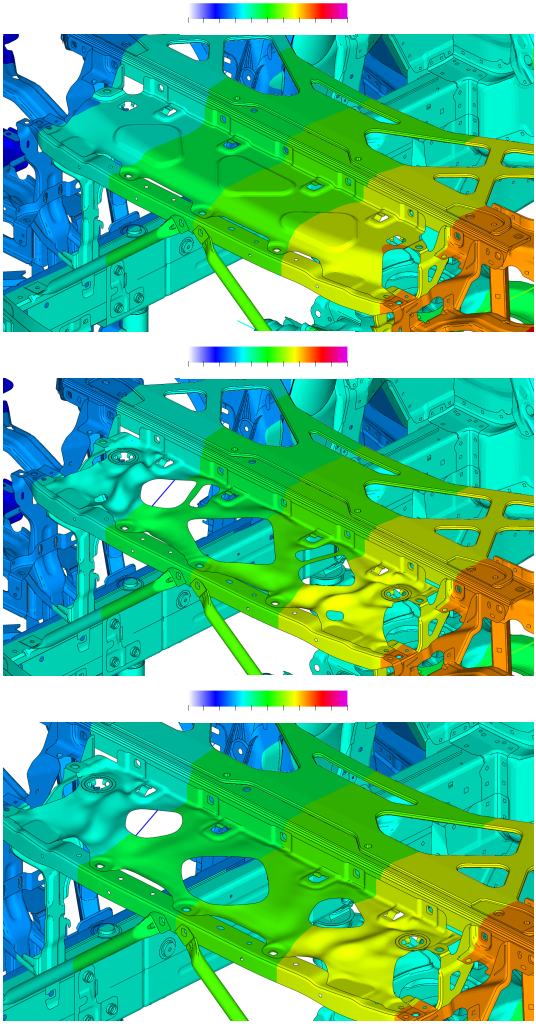

Figure 4.25 : Displacement plot for anti-symmetric torsional loading for the initial design (top) vs. the optimal designs from the simultaneous optimization without mass shape sensitivities (center) and with mass shape sensitivities (bottom).

Table 4.2 : Summary of response function percentile change for the full car-body analysis.

Function	change %	
	Constrained	Unconstrained
mass	-20.11	-17.01
Torsion I	0.00	0.00
Torsion II	0.17	0.19
Torsion III	0.15	0.17
Torsion IV	0.62	0.66
Torsion V	0.15	0.17

4.4 Hood inner panel

The proposed simultaneous shape and topology optimization formulation was put to test on another sheet metal component, the inner panel of a car hood. The fundamental difference of this application, in comparison to the shear panel of section 4.3, is that the void pattern is predetermined. In the current design process simulation engineers follow empirical rules of thumb based on cumulative collective experience. Our optimizer steers the inner panel to a design that is lighter than the initial one and stiffer for all the prescribed load cases. A summary of the successful optimization is given below.

Model description

The inner panel is a structural component of the hood system whose purpose is to stiffen the hood against external loading. Hood and inner panel are connected to each other by means of flanging the edges of the hood around the panel, and with adhesive connectors in the middle area of the inner panel. The computational model is illustrated in figure 4.26. Each prescribed force F_1, F_2, F_3 and F_4 represents one static nonlinear load case. The current design of the inner panel is shown in the middle of the figure. Reinforcing metal sheets are added to the hood system to increase the stiffness in critical regions. The modified design for the optimization is depicted at the bottom of the figure.

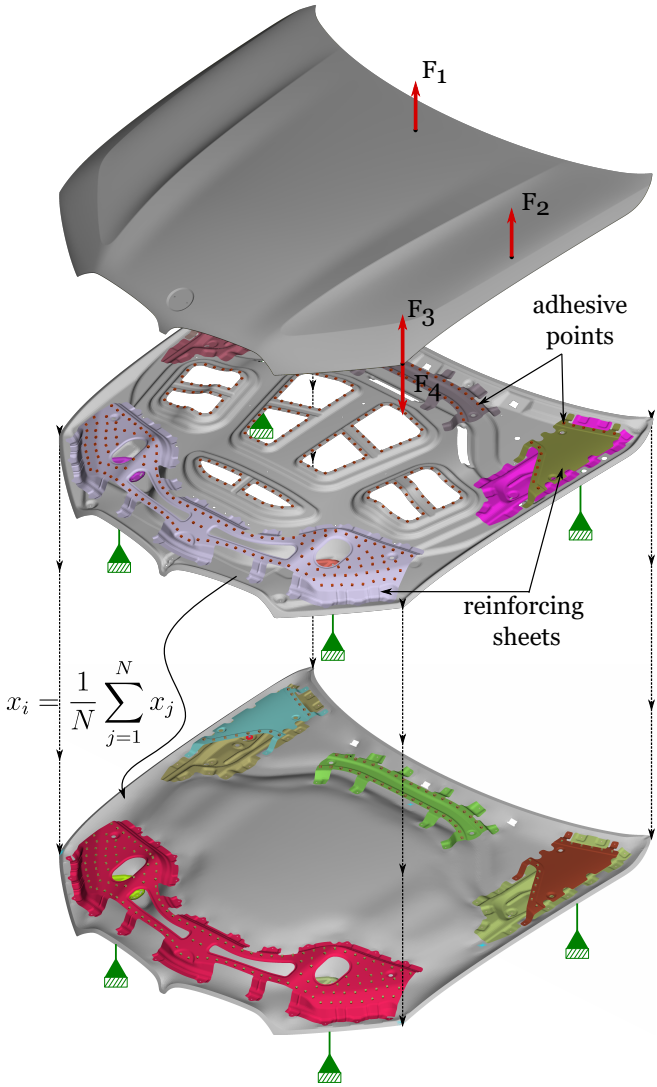

Figure 4.26 : Components of the full computational model. Hood (top) with load case forces, current hood inner panel design state (middle) and modified hood inner panel for optimization (bottom) with boundary conditions.

Optimization setup

The computational model of the hood system includes material and contact nonlinearities. In order to maintain the accuracy of the sensitivity output from the solver, it was decided to use the complete hood system for the optimization. The alternative would be, as in the shear panel application (4.3), to isolate the design space for the optimization (inner panel) and prescribe boundary conditions on the sub-model connectors. Keeping the full model leads to the requirement of a linearization: the contacts were substituted with rigid body elements and a linear formulation was used for the static analysis.

As was also the case with the shear panel (4.3), the optimization needs to start from a neutral design. The holes of the current design were filled with material so that the optimizer can suggest a novel void pattern that can substitute the current one. Excluded from the optimization were the regions around the welding points that connect the design space with other components of the assembly. Those areas remain common for both the modified and initial design. A laplacian smoothing algorithm is applied on the rest of the design space, such that each node position changes according to the function:

$$\bar{x}_i = \frac{1}{N} \sum_{j=1}^{N} \bar{x}_j \tag{4.6}$$

where N is the number of neighboring nodes of node i, $\bar{x}_j$ is the position of the j-th neighboring node and $\bar{x}_i$ is the new position for node i. The rationale behind this is the following: the preexisting design is a result of a type of CAD-based shape optimization. Design variables in CAD-based optimization are geometrical features, e.g., fillet radii, number and size of holes or number and size of beads. In node-based shape optimization with Vertex Morphing feature lines of the geometry are preserved, especially in the early stages of the optimization. Thus, starting a shape optimization from this predefined configuration limits the search space of the optimizer and, more likely than not, will converge to a local minimum in the vicinity of the initial design. The more neutral the optimization starting design is, the higher the likelihood that the optimized design will contain features that are optimal and

unimaginable to the designer. The initial design and the modified one for the simultaneous optimization are depicted once again in figure 4.27. Horizontal cross section profiles of the geometries are plotted against each other to display the smoothing of the feature lines.

The strain energies of the four load cases were applied as constraints to the optimization. The ratio of limit to initial constraint value was 0.75. In other words, improvement of the stiffness for all load cases by 25% was required. In addition, a packaging constraint and a maximum length update constraint of $10\,mm$ were added to the optimization. Reflection symmetry was imposed by using the enhanced Vertex Morphing formulation that was proposed in chapter 3.2. Finally, the ratio of shape to thickness length update was set to be equal to 10.

Optimization results

Two simultaneous optimizations were executed on the inner panel, with the the filter radius of the thickness design variables being the only difference between them: in the first one, the filter radius was approximately 3 times the element size of the design space, and in the second one, it was set to 6 times the element size. The motivation behind this was to investigate the effect of the Vertex Morphing filter radius on the optimal hole distribution and pattern. It should be noted that the filter radius for shape design variables was kept constant in both optimizations at approximately 6 times the average element size in order to avoid the formation of small scale details and features. The optimized geometry with the thickness distribution (left) and after surface cutting of the elements with zero thickness (right) is shown in figures 4.28 and 4.29 for the small and large filter radius optimization, respectively. The hole distribution is similar for both optimizations. What changes is the shape and size of the holes. The bigger the filter radius, the bigger and rounder the holes tend to be. At the same time, the transition region from zero to maximum thickness is larger, for the larger filter radius. As a result, with a larger filter radius more optimization iterations are required to achieve a similar objective function improvement compared to a smaller filter radius, as is the case in this application.

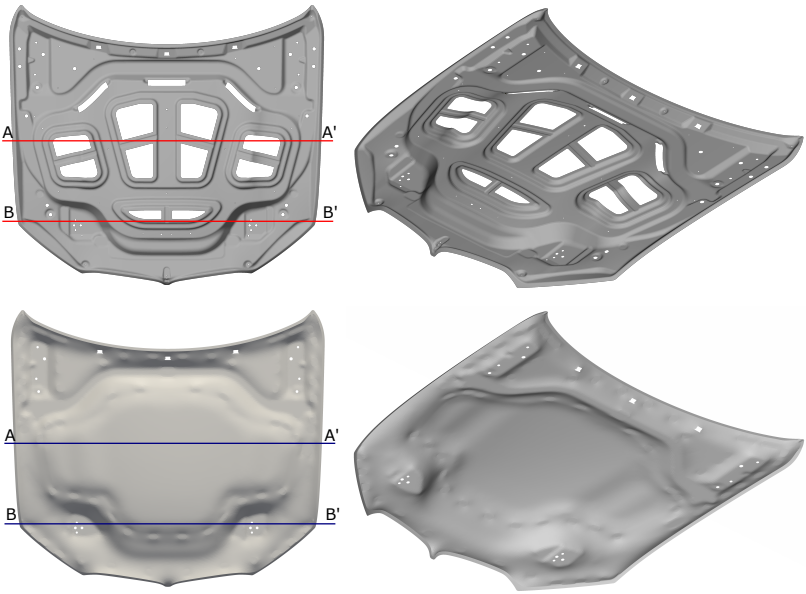

(a) Different views of the current hood inner panel design state (top row) and modified hood inner panel (bottom row).

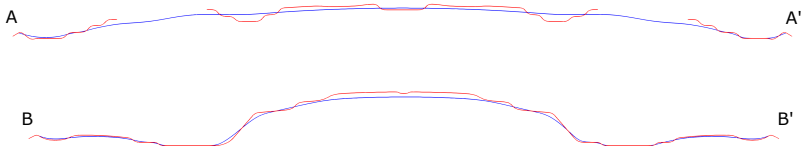

(b) Cross section profile comparison between design state and modified state of hood inner panel. Planes shown in top figure.

Figure 4.27 : Hood inner panel current design state and modified design used as starting point for the optimization.

It is interesting to compare the hole distribution of the optimized geometries with that of the initial design. In all designs, holes develop in the middle area of the part. A reasonable explanation is that, since the middle area is the furthest away from the boundary conditions, it contributes the least to the overall structural stiffness. However, it can be seen that during the optimization holes also develop at the top left and right of the geometry where the inner panel connects with the hinge system and the rest of the car. At first this might seem unreasonable but after a closer look it becomes clear that those regions are structurally supported extensively from the existing reinforcing sheets. Thus, there is excess material and it can be reduced.

At the bottom of each graph, the response function absolute change is plotted. For roughly the first 30 to 40 iterations, mass reduction is slow since the algorithm's focus is to push the design towards the feasible domain via shape update of the nodes. Afterwards, thickness update begins to reduce the mass almost linearly with respect to the iteration number and shape update ensures that the continuous weight reduction does not compromise the structural stiffness. It can be seen, that, for both optimizations, the constraint values oscillate around their limits. This can be attributed to the fact that our optimization formulation is based on a linear approximation of the response functions (first-order gradients) in combination with the high nonlinearity of the response functions.

The diagram of figure 4.30 has an interesting message for the understanding of the proposed simultaneous optimization. The search direction is composed of the projection move and the restoration move. The former is the projection of the objective gradient into the subspace tangent to the active constraints. The latter is to bring the search direction back to the constraint boundary by moving back in the direction of the constraint gradient. The desired ratio between shape and thickness maximal update is achieved mostly through correction move manipulation. As can be observed, the projected direction ratio has a value that varies from ~ 0.1 to ~ 2.0 and only after correction is the desired ratio attained. Scaling of thickness objective and constraint sensitivities with the same factor has a different effect on the ratio of the search direction. This explains the importance of the correction move in the proposed simulta-

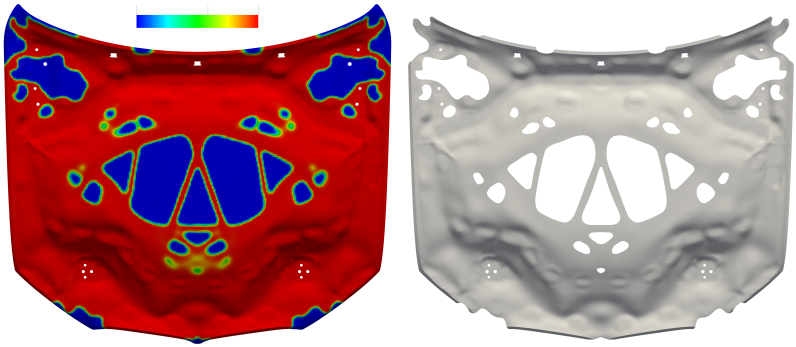

(a) Simultaneous shape and topology optimization optimal design with thickness distribution (left) and with holes cut open (right) for a filter radius of $25mm$.

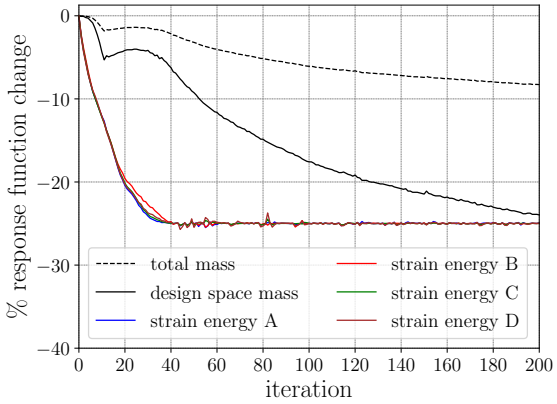

(b) Response function evolution for simultaneous optimization with filter radius $25mm$

Figure 4.28 : Simultaneous shape and topology optimization optimal hood inner panel results for filter radius $25mm$.

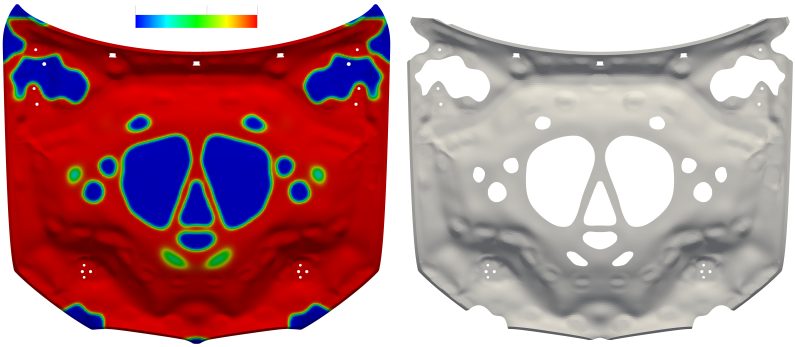

(a) Simultaneous shape and topology optimization optimal design with thickness distribution (left) and with holes cut open (right) for a filter radius of $50mm$.

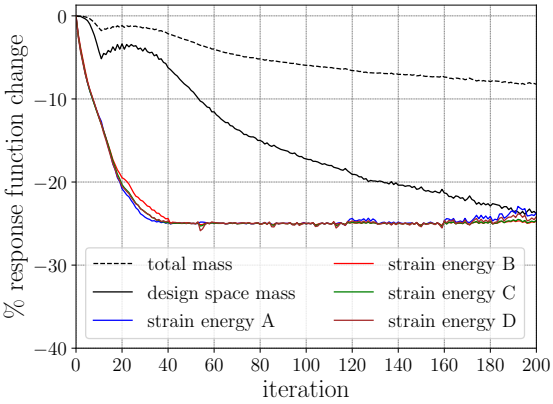

(b) Response function evolution for simultaneous optimization with filter radius $50mm$

Figure 4.29 : Simultaneous shape and topology optimization optimal hood inner panel results for filter radius $50mm$.

neous optimization, where mass is the objective, and not the constraint, function (as in traditional sensitivity-based topology optimization) and the starting thickness is equal to the maximum possible value. Mass, then, is reduced by the projection move and the correction move assures that constraints are not violated.

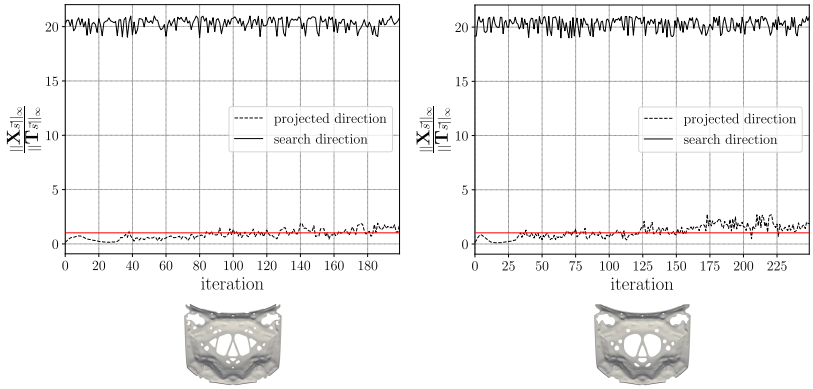

Figure 4.30 : Shape to thickness design variable update ratio per iteration for simultaneous optimization with a filter radius of $25mm$ (left) and $50mm$ (right). The red line denotes a ratio of 1.

In order to validate the success of the optimizations, the improved designs were tested in the full nonlinear model. The displacement fields, for all four load cases, of both improved designs are plotted against those of the initial design in figures 4.31 and 4.32 respectively. As it can be seen, the displacement field of the hood has improved significantly, especially for load case I, III and IV. Table 4.3 summarizes, for both optimizations, the percentile change of the response functions with respect to the initial design values. A staggering improve of the structural stifness of up to approximately 50% in some of the load cases and a mass reduction of almost 15%. For real life industrial applications such order of improvement is rather generous.

Admittedly, such a design could not be included into a vehicle immediately out-of-the-box yet. The hood system and its respective components is highly complex and more manufacturing, geometric, and physical constraints need to be fulfilled before it can be deployed. Nonetheless, the

proposed simultaneous optimization shows the potential to be gained, by leading to design suggestions and modifications, if incorporated in the design process.

Table 4.3 : Summary of response function percentile change for the full model analysis (mass change only for design space).

Function	change %	
	Filter radius $25mm$	Filter radius $50mm$
mass	-14.12	-13.43
Stiffness I	-51.19	-53.59
Stiffness II	-14.00	-21.84
Stiffness III	-40.86	-34.54
Stiffness IV	-31.71	-32.38

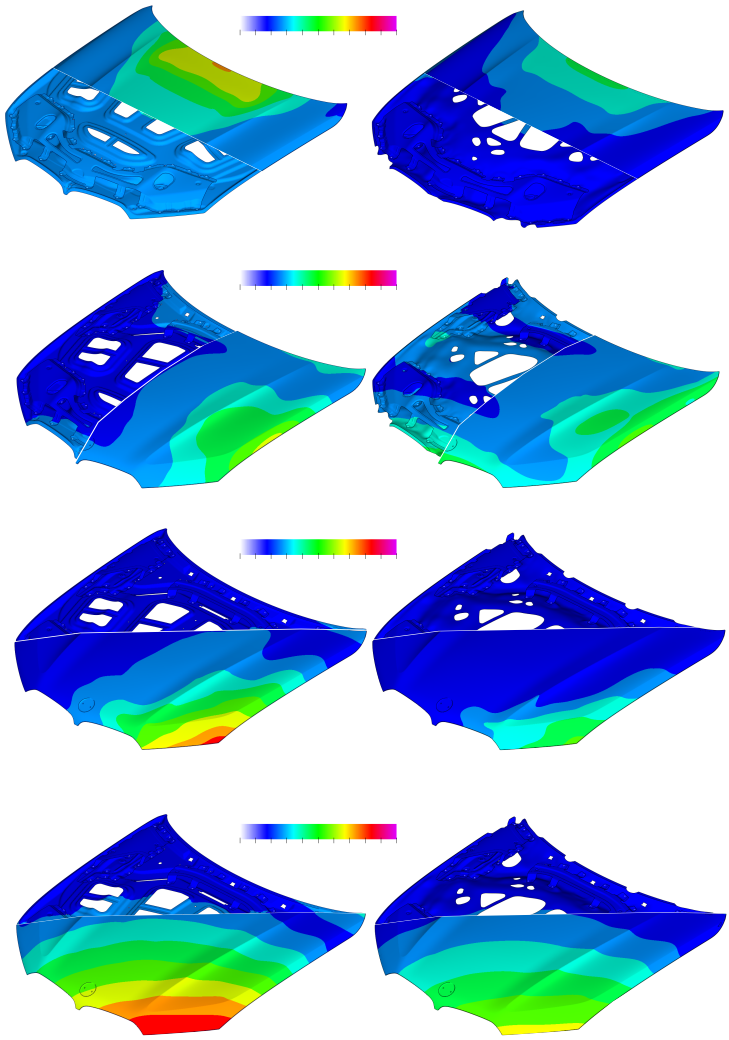

Figure 4.31 : Displacement field for all four load cases (row-wise) for the initial design (left column) and the simultaneous optimization with filter radius of $25mm$ design (right column).

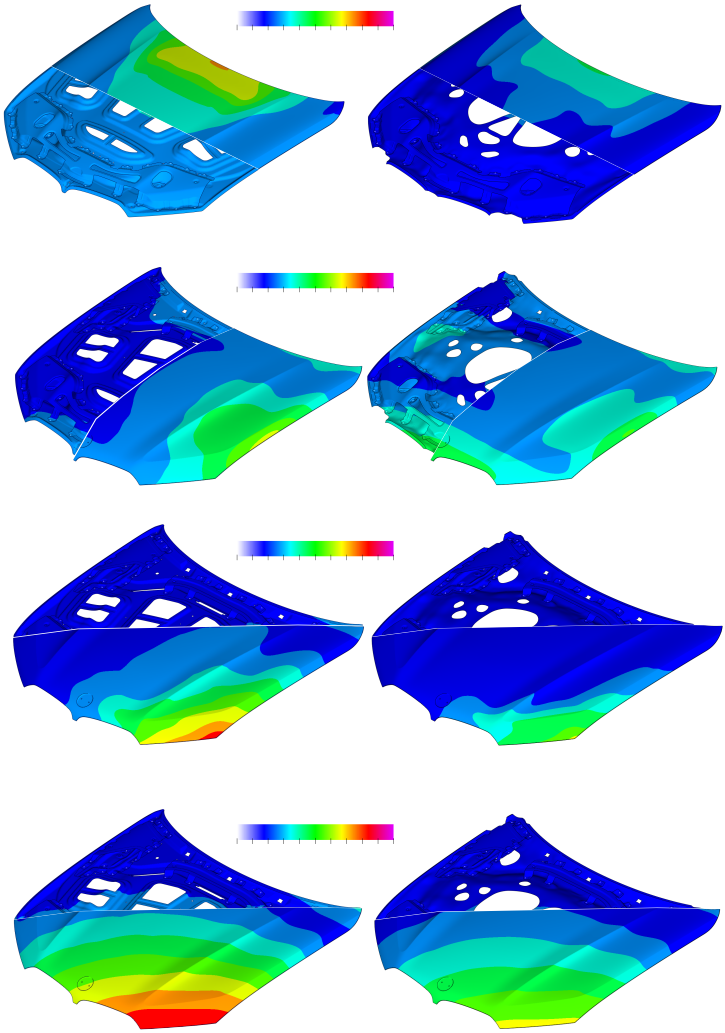

Figure 4.32 : Displacement field for all four load cases (row-wise) for the initial design (left column) and the simultaneous optimization with filter radius of $50mm$ design (right column).

Chapter 5

Conclusions and outlook

This thesis is the natural continuation of prior work on the topic and deals with the integration of numerical structural optimization with the Vertex Morphing parametrization into the design process of BMW. Novel methods for the incorporation of three industrial constraints were proposed and implemented in a numerical structural optimization workflow within BMW. Different techniques of manipulating the optimization problem were identified and used as a basis to introduce these constraints, such as direct addition of a mathematical constraint function to the optimization problem, enhancement of the Vertex Morphing mapping, and a dimensional extension of the Vertex Morphing parametrization. Focus was ease of use, consistency with the Vertex Morphing formulation, computational efficiency, and integrability in an industrial environment.

An aggregate constraint function that prohibits formulation of undercut regions during optimization was proposed. The point-wise problem was transposed into a global undercut volume minimization problem. The optimal design surface slope can be defined by an input parameter which

controls the constraint function calculation and, in turn, the sensitivities. This feature allows development of overhang or slab regions, such that manufacturability with the intended process is ensured, i.e., with additive or subtractive manufacturing. In comparison to point-wise constraints, the proposed method is computationally faster.

Moreover, the constraint for reflection symmetry of designs that are described by non-symmetric boundary conditions was tackled with an enhancement of the Vertex Morphing parametrization. Through the utilization of an adaptive convolution kernel, which results in densification of the mapping matrix, the sensitivity and the shape update fields are averaged about the symmetry plane. The method's robustness in handling non-symmetric meshes is demonstrated through optimization of a conceptual 1D test case.

Finally, the Vertex Morphing parametrization was extended from 3D to 4D with the addition of nodal thickness design variables. Vertex Morphing has proven a consistent framework for thickness and topology optimization. Filtering methods applied in topology optimization for sensitivity or density field filtering can be replaced by the Vertex Morphing mapping without any loss of information or generality. Additionally, to ensure that nodal thickness values will remain in the admissible range during optimization, an s-shaped reparametrization of the thickness design variables, on top of the Vertex Morphing parametrization, is proposed. The problem of step size length proportionality for the shape and thickness design variables was formulated as a root finding problem and solved with a classic bracketing method. Convergence characteristics of the method are investigated through optimization of a simple application.

The methods were put successfully to test through optimization of a range of industrial automotive applications, provided by BMW, in chapter 4. In order to enable shape optimization of a hood hinge system bracket modeled with a solid mesh, an automatic solid mesh motion was developed in our numerical framework. Moreover, for a front-end shear panel optimization, a comparative study between the simultaneous shape and topology optimization approach in this thesis, a staggered shape and topology optimization approach, and serial optimization approaches

was conducted in terms of overall optimality and computational efficiency, proving the efficacy of the proposed formulation. Finally, for the optimization of a hood inner panel, the effect of the Vertex Morphing mapping filter radius on the topology and shape of the optimal design was investigated.

According to the author's perspective, further research in the direction of optimization algorithms that would accelerate convergence of the proposed simultaneous shape and topology optimization approach is needed. Furthermore, this work could provide inspiration for the development of methods to incorporate more industrial constraints in numerical optimization.

Bibliography

[1] G. Allaire, C. Dapogny, R. Estevez, A. Faure, and G. Michailidis. "Structural optimization under overhang constraints imposed by additive manufacturing technologies." In: *Journal of Computational Physics* 351 (2017), pp. 295–328. DOI: https://doi.org/10.1016/j.jcp.2017.09.041.

[2] G. Allaire, F. Jouve, and G. Michailidis. "Casting constraints in structural optimization via a level-set method." In: *10th World Congress on Structural and Multidisciplinary Optimization*. Orlando, United States, May 2013.

[3] G. Allaire, F. Jouve, and A.-M. Toader. "A level-set method for shape optimization." In: *Comptes Rendus Mathematique* 334.12 (2002), pp. 1125–1130.

[4] G. Allaire and R. V. Kohn. "Optimal design for minimum weight and compliance in plane stress using extremal microstructures." In: *European Journal of Mechanics A-solids* 12 (1993), pp. 839–878.

[5] G. Allaire, F. de Gournay, F. Jouve, and A.-M. Toader. "Structural optimization using topological and shape sensitivity via a level set method." In: *Control and Cybernetics* 34.1 (2005), 59–80.

[6] G. Allaire, F. Jouve, and G. Michailidis. “Thickness control in structural optimization via a level set method.” In: *Structural and Multidisciplinary Optimization* 53 (June 2016). DOI: 10.1007/s00158-016-1453-y.

[7] G. Allaire, F. Jouve, and A.-M. Toader. “Structural optimization using sensitivity analysis and a level-set method.” In: *Journal of Computational Physics* 194.1 (2004), pp. 363–393. DOI: https://doi.org/10.1016/j.jcp.2003.09.032.

[8] L. Ambrosio and G. Buttazzo. “An optimal design problem with perimeter penalization.” In: *Calculus of Variations* 1 (Mar. 1993), pp. 55–69. DOI: 10.1007/BF02163264.

[9] C. S. Andreasen, M. O. Elingaard, and N. Aage. “Level set topology and shape optimization by density methods using cut elements with length scale control.” In: *Structural and Multidisciplinary Optimization* (2020), pp. 1–23.

[10] R. Ansola, J. Canales, J. Tarrago, and J. Rasmussen. “On simultaneous shape and material layout optimization of shell structures.” In: *Structural and Multidisciplinary Optimization* 24 (Jan. 2002), pp. 175–184. DOI: 10.1007/s00158-002-0227-x.

[11] R. Ansola, J. Canales, J. A. Tárrago, and J. Rasmussen. “An integrated approach for shape and topology optimization of shell structures.” In: *Computers & Structures* 80.5 (2002), pp. 449–458. DOI: https://doi.org/10.1016/S0045-7949(02)00019-6.

[12] S. Arnout, M. Firl, and K.-U. Bletzinger. “Parameter free shape and thickness optimisation considering stress response.” In: *Structural and Multidisciplinary Optimization* 45 (June 2012). DOI: 10.1007/s00158-011-0742-8.

[13] D. Ashlock. *Evolutionary Computation for Modeling and Optimization*. Jan. 2006. ISBN: 978-0-387-22196-0. DOI: 10.1007/0-387-31909-3.

[14] D. Baumgärtner, A. Viti, A. Dumont, G. Carrier, and K.-U. Bletzinger. “Comparison and combination of experience-based parametrization with Vertex Morphing in aerodynamic shape optimization of a forward-swept wing aircraft.” In: *17th AIAA/ISSMO Multidisciplinary Analysis and Optimization Conference*. DOI: 10.2514/6.2016-3368. eprint: https://arc.aiaa.org/doi/pdf/10.2514/6.2016-3368.

[15] M Beckers. “Topology optimization using a dual method with discrete variables.” In: *Structural optimization* 17.1 (Feb. 1999), pp. 14–24.

[16] M. Bendsøe. “Bendsoe, M.P.: Optimal Shape Design as a Material Distribution Problem. Structural Optimization 1, 193-202.” In: *Structural Optimization* 1 (Jan. 1989), pp. 193–202. DOI: 10.1007/BF01650949.

[17] M. P. Bendsøe and N. Kikuchi. “Generating optimal topologies in structural design using a homogenization method.” In: *Computer Methods in Applied Mechanics and Engineering* 71.2 (1988), pp. 197–224. DOI: https://doi.org/10.1016/0045-7825(88)90086-2.

[18] M. P. Bendsoe and O. Sigmund. *Topology optimization: theory, methods, and applications*. Springer Science & Business Media, 2013.

[19] J. A. Bennett and M. E. Botkin. “Structural shape optimization with geometric description and adaptive mesh refinement.” In: *AIAA Journal* 23.3 (1985), pp. 458–464. DOI: 10.2514/3.8935. eprint: https://doi.org/10.2514/3.8935.

[20] K.-U. Bletzinger. “A consistent frame for sensitivity filtering and the vertex assigned morphing of optimal shape.” In: *Structural and Multidisciplinary Optimization* 49 (Jan. 2014). DOI: 10.1007/s00158-013-1031-5.

[21] K.-U. Bletzinger. “Shape Optimization.” In: *Encyclopedia of Computational Mechanics Second Edition*. American Cancer Society, 2017, pp. 1–42. ISBN: 9781119176817. DOI: https://doi.org/10.1002/9781119176817.ecm2109.

eprint: https://onlinelibrary.wiley.com/doi/pdf/10.1002/9781119176817.ecm2109.

[22] K.-U. Bletzinger and K. Maute. “Towards generalized shape and topology optimization.” In: *Engineering Optimization* 29.1-4 (1997), pp. 201–216.

[23] V. Braibant and C. Fleury. “Shape optimal design using B-splines.” In: *Computer Methods in Applied Mechanics and Engineering* 44.3 (1984), pp. 247–267. DOI: https://doi.org/10.1016/0045-7825(84)90132-4.

[24] T. E. Bruns and D. A. Tortorelli. “Topology optimization of non-linear elastic structures and compliant mechanisms.” In: *Computer Methods in Applied Mechanics and Engineering* 190.26 (2001), pp. 3443–3459. DOI: https://doi.org/10.1016/S0045-7825(00)00278-4.

[25] M. Burger, B. Hackl, and W. Ring. “Incorporating topological derivatives into level set methods.” In: *Journal of Computational Physics* 194.1 (2004), pp. 344–362.

[26] J. Céa, S. Garreau, P. Guillaume, and M. Masmoudi. “The shape and topological optimizations connection.” In: *Computer methods in applied mechanics and engineering* 188.4 (2000), pp. 713–726.

[27] S. Chen, M. Y. Wang, and A. Q. Liu. “Shape feature control in structural topology optimization.” In: *Computer-Aided Design* 40.9 (2008), pp. 951–962. DOI: https://doi.org/10.1016/j.cad.2008.07.004.

[28] D. Chenais. “On the existence of a solution in a domain identification problem.” In: *Journal of Mathematical Analysis and Applications* 52.2 (1975), pp. 189–219. DOI: https://doi.org/10.1016/0022-247X(75)90091-8.

[29] G. Cheng, Y. Mei, and X. Wang. “A Feature-Based Structural Topology Optimization Method.” In: *IUTAM Symposium on Topological Design Optimization of Structures, Machines and Materials*. Ed. by M. P. Bendsøe, N. Olhoff, and O. Sigmund. Dordrecht: Springer Netherlands, 2006, pp. 505–514. ISBN: 978-1-4020-4752-7.

[30] K.-T. Cheng and N. Olhoff. “An investigation concerning optimal design of solid elastic plates.” In: *International Journal of Solids and Structures* 17.3 (1981), pp. 305–323. DOI: https://doi.org/10.1016/0020-7683(81)90065-2.

[31] A. N. Christiansen, M. Nobel-Jørgensen, N. Aage, O. Sigmund, and J. A. Bærentzen. “Topology optimization using an explicit interface representation.” In: *Structural and Multidisciplinary Optimization* 49.3 (2014), pp. 387–399.

[32] S. Conte and C. de Boor. “CHAPTER THREE: THE SOLUTION OF NONLINEAR EQUATIONS.” In: *Elementary Numerical Analysis*, pp. 72–127. DOI: 10.1137/1.9781611975208.ch3. eprint: https://epubs.siam.org/doi/pdf/10.1137/1.9781611975208.ch3.

[33] G. Darboux. *Lecons sur la Theorie Generale des surfaces*. Gauthier-Villars, 1946.

[34] N. P. van Dijk, K. Maute, M. Langelaar, and F. Van Keulen. “Level-set methods for structural topology optimization: a review.” In: *Structural and Multidisciplinary Optimization* 48.3 (2013), pp. 437–472.

[35] M. Dowell and P. Jarratt. “A modified regula falsi method for computing the root of an equation.” In: *BIT Numerical Mathematics* 11 (1971), pp. 168–174.

[36] F.-J. Ertl, G. Dhondt, and K.-U. Bletzinger. “Vertex assigned morphing for parameter free shape optimization of 3-dimensional solid structures.” In: *Computer Methods in Applied Mechanics and Engineering* 353 (2019), pp. 86 –106. DOI: https://doi.org/10.1016/j.cma.2019.05.004.

[37] H. A. Eschenauer, V. V. Kobelev, and A. Schumacher. “Bubble method for topology and shape optimization of structures.” In: *Structural optimization* 8.1 (1994), pp. 42–51.

[38] J. Ford. “Improved algorithms of illinois-type for the numerical solution of nonlinear equations.” In: *University of Essex, Department of Computer Science* (1995).

[39] A. Gaynor and J. Guest. “Topology optimization considering overhang constraints: Eliminating sacrificial support material in additive manufacturing through design.” In: *Structural and Multidisciplinary Optimization* 54 (Nov. 2016). DOI: 10.1007/s00158-016-1551-x.

[40] A. Geiser, I. Antonau, and K.-U. Bletzinger. “AGGREGATED FORMULATION OF GEOMETRIC CONSTRAINTS FOR NODE-BASED SHAPE OPTIMIZATION WITH VERTEX MORPHING.” In: Jan. 2021, pp. 80–94. DOI: 10.7712/140121.7952.18383.

[41] D. Goldberg, G. David Edward, D. Goldberg, and V. Goldberg. *Genetic Algorithms in Search, Optimization, and Machine Learning*. Artificial Intelligence. Addison-Wesley Publishing Company, 1989. ISBN: 9780201157673.

[42] J. K. Guest, J. H. Prévost, and T. Belytschko. “Achieving minimum length scale in topology optimization using nodal design variables and projection functions.” In: *International Journal for Numerical Methods in Engineering* 61 (2 Sept. 2004), pp. 238–254. DOI: 10.1002/nme.1064.

[43] J. Guest. “Imposing maximum length scale in topology optimization.” In: *Structural and Multidisciplinary Optimization* 37 (Feb. 2009), pp. 463–473. DOI: 10.1007/s00158-008-0250-7.

[44] X. Guo, W. Zhang, and W. Zhong. “Explicit feature control in structural topology optimization via level set method.” In: *Computer Methods in Applied Mechanics and Engineering* 272 (2014), pp. 354 –378. DOI: https://doi.org/10.1016/j.cma.2014.01.010.

[45] X. Guo, K. Zhao, and M. Y. Wang. “A new approach for simultaneous shape and topology optimization based on dynamic implicit surface function.” In: *Control and Cybernetics* 34 (2005), pp. 255–282.

[46] R. Haber, C. Jog, and M. Bendsøe. “A new approach to variable-topology shape design using a constraint on perimeter.” English (US). In: *Structural and Multidisciplinary*

Optimization 11.1 (Jan. 1996), pp. 1–12. DOI: 10.1007/BF01279647.

[47] B. Hassani, M. Tavakkoli, and H. Ghasemnejad. “Simultaneous shape and topology optimization of shell structures.” In: *Structural and Multidisciplinary Optimization* 48 (July 2013). DOI: 10.1007/s00158-013-0894-9.

[48] M. Hojjat. “Node-based parametrization for shape optimal design.” Dissertation. München: Technische Universität München, 2015.

[49] M. Hojjat, E. Stavropoulou, and K.-U. Bletzinger. “The Vertex Morphing method for node-based shape optimization.” In: *Computer Methods in Applied Mechanics and Engineering* 268 (2014), pp. 494 –513. DOI: https://doi.org/10.1016/j.cma.2013.10.015.

[50] M. H. Imam. “Three-dimensional shape optimization.” In: *International Journal for Numerical Methods in Engineering* 18.5 (1982), pp. 661–673. DOI: https://doi.org/10.1002/nme.1620180504. eprint: https://onlinelibrary.wiley.com/doi/pdf/10.1002/nme.1620180504.

[51] A. Jacobson, D. Panozzo, et al. *libigl: A simple C++ geometry processing library*. https://libigl.github.io/. 2018.

[52] K. James, J. Hansen, and J. Martins. “Structural topology optimization for multiple load cases using a dynamic aggregation technique.” In: *Engineering Optimization* 41 (Dec. 2009), pp. 1103–1118. DOI: 10.1080/03052150902926827.

[53] H. Jasak and Z. Tukovic. “Automatic mesh motion for the unstructured Finite Volume Method.” In: *Transactions of Famena* (2006). DOI: 10.1126/science.1247727. arXiv: arXiv:1011.1669v3.

[54] G. Kennedy and J. Hicken. “Improved constraint-aggregation methods.” In: *Computer Methods in Applied Mechanics and Engineering* 289 (June 2015). DOI: 10.1016/j.cma.2015.02.017.

[55] M. Keuthen and M. Ulbrich. “Moreau–Yosida regularization in shape optimization with geometric constraints.” In: *Computational Optimization and Applications* 62 (Sept. 2015), pp. 181–216. DOI: 10.1007/s10589-014-9661-0.

[56] S. Kirkpatrick, C. D. Gelatt Jr, and M. P. Vecchi. “Optimization by simulated annealing.” In: *science* 220.4598 (1983), pp. 671–680.

[57] R. V. Kohn and G. Strang. “Optimal design and relaxation of variational problems, I.” In: *Communications on Pure and Applied Mathematics* 39.1 (1986), pp. 113–137. DOI: https://doi.org/10.1002/cpa.3160390107. eprint: https://onlinelibrary.wiley.com/doi/pdf/10.1002/cpa.3160390107.

[58] C. Le, T. Bruns, and D. Tortorelli. “A gradient-based, parameter-free approach to shape optimization.” In: *Computer Methods in Applied Mechanics and Engineering* 200.9 (2011), pp. 985–996. DOI: https://doi.org/10.1016/j.cma.2010.10.004.

[59] J. Leiva, B. Watson, and I. Kosaka. “An Analytical Directional Growth Topology Parameterization to Enforce Manufacturing Requirements.” In: vol. 2. Apr. 2004. ISBN: 978-1-62410-079-6. DOI: 10.2514/6.2004-1645.

[60] J. Leiva, B. Watson, and I. Kosaka. “An Analyticall Bi-Directional Growth Parameterization to Obtain Optimal Castable Topology Designs.” In: vol. 5. Aug. 2004. ISBN: 978-1-62410-019-2. DOI: 10.2514/6.2004-4596.

[61] J. L. Lions. *Optimal control of systems governed by partial differential equations problèmes aux limites*. Grundlehren der mathematischen Wissenschaften A Series of Comprehensive Studies in Mathematics. Berlin: Springer, 1971.

[62] K Maute and E Ramm. “Adaptive topology optimization.” In: *Structural optimization* 10.2 (1995), pp. 100–112.

[63] H. P. Mlejnek. “Some aspects of the genesis of structures.” In: *Structural optimization* 5.1 (Mar. 1992), pp. 64–69.

[64] B. Mohammadi and O. Pironneau. “Applied Shape Optimization for Fluids, Second Edition.” In: *Numerical mathematics and scientific computation*. 2009.

[65] R. Najian Asl. “Shape optimization and sensitivity analysis of fluids, structures, and their interaction using Vertex Morphing parametrization.” Dissertation. München: Technische Universität München, 2019.

[66] R. Najian Asl, S. Shayegan, A. Geiser, M. Hojjat, and K.-U. Bletzinger. “A Consistent Formulation for Imposing Packaging Constraints in Shape Optimization Using Vertex Morphing Parametrization.” In: *Struct. Multidiscip. Optim.* 56.6 (Dec. 2017), 1507–1519. DOI: 10.1007/s00158-017-1819-9.

[67] J. A. Norato, M. P. Bendsøe, R. B. Haber, and D. A. Tortorelli. “A topological derivative method for topology optimization.” In: *Structural and Multidisciplinary Optimization* 33.4-5 (2007), pp. 375–386.

[68] N. Olhoff, M. P. Bendsøe, and J. Rasmussen. “On CAD-integrated structural topology and design optimization.” In: *Computer Methods in Applied Mechanics and Engineering* 89.1-3 (1991), pp. 259–279.

[69] S. Osher and J. A. Sethian. “Fronts propagating with curvature-dependent speed: Algorithms based on Hamilton-Jacobi formulations.” In: *Journal of computational physics* 79.1 (1988), pp. 12–49.

[70] C. Othmer. “Adjoint methods for car aerodynamics.” In: *Journal of Mathematics in Industry* 4 (Dec. 2014), p. 6. DOI: 10.1186/2190-5983-4-6.

[71] D. Panozzo, E. Puppo, and L. Rocca. “Efficient multi-scale curvature and crease estimation.” In: *2nd International Workshop on Computer Graphics, Computer Vision and Mathematics, GraVisMa 2010 - Workshop Proceedings* (Jan. 2010), pp. 9–16.

[72] P. Y. Papalambros and M. Chirehdast. “An integrated environment for structural configuration design.” In: *Journal of Engineering Design* 1.1 (1990), pp. 73–96.

[73] O. Pironneau. “On optimum design in fluid mechanics.” In: *Journal of Fluid Mechanics* 64.1 (1974), 97–110. DOI: 10.1017/S0022112074002023.

[74] N. Poon and J. Martins. “An Adaptive Approach to Constraint Aggregation Using Adjoint Sensitivity Analysis.” In: *Structural and Multidisciplinary Optimization* 34 (July 2007), pp. 61–73. DOI: 10.1007/s00158-006-0061-7.

[75] T. A. Poulsen. “A new scheme for imposing a minimum length scale in topology optimization.” In: *International Journal for Numerical Methods in Engineering* 57.6 (2003), pp. 741–760. DOI: https://doi.org/10.1002/nme.694. eprint: https://onlinelibrary.wiley.com/doi/pdf/10.1002/nme.694.

[76] J. B. Rosen. “The gradient projection method for nonlinear programming. Part II. Nonlinear constraints.” In: *Journal of the society for industrial and applied mathematics* 9.4 (1961), pp. 514–532.

[77] J. B. Rosen. “The gradient projection method for nonlinear programming. Part I. Linear constraints.” In: *Journal of the society for industrial and applied mathematics* 8.1 (1960), pp. 181–217.

[78] G. I. Rozvany. “A critical review of established methods of structural topology optimization.” In: *Structural and multidisciplinary optimization* 37.3 (2009), pp. 217–237.

[79] J. Samareh. “Survey of Shape Parameterization Techniques for High-Fidelity Multidisciplinary Shape Optimization.” In: *Aiaa Journal - AIAA J* 39 (May 2001), pp. 877–884. DOI: 10.2514/2.1391.

[80] J. A. Samareh. *A Survey Of Shape Parameterization Techniques*. 1999.

[81] O. Schmitt, J. Friederich, S. Riehl, and P. Steinmann. “On the formulation and implementation of geometric and manufacturing constraints in node–based shape optimization.” In: *Structural and Multidisciplinary Optimization* 53 (Apr. 2016). DOI: 10.1007/s00158-015-1359-0.

[82] O. Schmitt and P. Steinmann. “Control of minimum member size in parameter-free structural shape optimization by a medial axis approximation.” In: *Computational Mechanics* 61 (June 2018). DOI: 10.1007/s00466-017-1477-1.

[83] O. Schmitt and P. Steinmann. “On curvature approximation in 2D and 3D parameter–free shape optimization.” In: *Structural and Multidisciplinary Optimization* 55 (May 2017). DOI: 10.1007/s00158-016-1595-y.

[84] J. A. Sethian. *Level set methods and fast marching methods: evolving interfaces in computational geometry, fluid mechanics, computer vision, and materials science*. Vol. 3. Cambridge university press, 1999.

[85] A. Seyranian, E. Lund, and N. Olhoff. “Multiple eigenvalues in structural optimization problems.” In: *Structural Optimization* 8 (Dec. 1994), pp. 207–227. DOI: 10.1007/BF01742705.

[86] O. Sigmund. “Morphology-based black and white filters for topology optimization.” In: *Structural and Multidisciplinary Optimization* 33 (Apr. 2007), pp. 401–424. DOI: 10.1007/s00158-006-0087-x.

[87] O. Sigmund. “On the Design of Compliant Mechanisms Using Topology Optimization.” In: *Mechanics of Structures and Machines* 25.4 (1997), pp. 493–524. DOI: 10.1080/08905459708945415. eprint: https://doi.org/10.1080/08905459708945415.

[88] O. Sigmund and K. Maute. “Topology optimization approaches.” In: *Structural and Multidisciplinary Optimization* 48.6 (2013), pp. 1031–1055.

[89] O. Sigmund and J. Petersson. “Numerical instabilities in topology optimization: A survey on procedures dealing with checkerboards, mesh-dependencies and local minima.” In: *Structural Optimization* 16 (Aug. 1998), pp. 68–75. DOI: 10.1007/BF01214002.

[90] J. Sokolowski and A. Zochowski. “On the topological derivative in shape optimization.” In: *SIAM journal on control and optimization* 37.4 (1999), pp. 1251–1272.

[91] G. Strang and R. V. Kohn. “Optimal design in elasticity and plasticity.” In: *International Journal for Numerical Methods in Engineering* 22.1 (1986), pp. 183–188. DOI: https://doi.org/10.1002/nme.1620220113. eprint: https://onlinelibrary.wiley.com/doi/pdf/10.1002/nme.1620220113.

[92] S. L. Vatanabe, T. N. Lippi, C. R. de Lima, G. H. Paulino, and E. C. Silva. “Topology optimization with manufacturing constraints: A unified projection-based approach.” In: *Advances in Engineering Software* 100 (2016), pp. 97–112. DOI: https://doi.org/10.1016/j.advengsoft.2016.07.002.

[93] M. Y. Wang, X. Wang, and D. Guo. “A level set method for structural topology optimization.” In: *Computer methods in applied mechanics and engineering* 192.1-2 (2003), pp. 227–246.

[94] X. Wang, Y. Mei, and M. Wang. “Incorporating topological derivatives into level set methods for structural topology optimization.” In: *10Th AIAA/ISSMO multidisciplinary analysis and optimization conference*. 2004, p. 4564.

[95] Q. Xia, T. Shi, M. Wang, and S. Liu. “A level set based method for the optimization of cast part.” In: *Structural and Multidisciplinary Optimization* 41 (May 2009), pp. 735–747. DOI: 10.1007/s00158-009-0444-7.

[96] Q. Xia, T. Shi, M. Wang, and S. Liu. “Simultaneous optimization of cast part and parting direction using level set method.” In: *Structural and Multidisciplinary Optimization* 44 (Dec. 2011), pp. 751–759. DOI: 10.1007/s00158-011-0690-3.

[97] Y. Xie and G. Steven. “A simple evolutionary procedure for structural optimization.” In: *Computers & Structures* 49.5 (1993), pp. 885–896. DOI: https://doi.org/10.1016/0045-7949(93)90035-C.

[98] G. H. Yoon and Y. Y. Kim. “The role of S-Shape mapping functions in the SIMP approach for topology optimization.” In: *KSME International Journal* 17.10 (2003), pp. 1496–1506. DOI: 10.1007/BF02982329.

[99] M. Zhou and G. Rozvany. “The COC algorithm, Part II: Topological, geometrical and generalized shape optimization.” In: *Computer Methods in Applied Mechanics and Engineering* 89.1 (1991). Second World Congress on Computational Mechanics, pp. 309–336. DOI: https://doi.org/10.1016/0045-7825(91)90046-9.

[100] M. Zhou, B. S. Lazarov, F. Wang, and O. Sigmund. “Minimum length scale in topology optimization by geometric constraints.” In: *Computer Methods in Applied Mechanics and Engineering* 293 (2015), pp. 266–282. DOI: https://doi.org/10.1016/j.cma.2015.05.003.

Bisherige Titel der Schriftenreihe

Band	Titel
1	Frank Koschnick, *Geometrische Lockingeffekte bei Finiten Elementen und ein allgemeines Konzept zu ihrer Vermeidung*, 2004.
2	Natalia Camprubi, *Design and Analysis in Shape Optimization of Shells*, 2004.
3	Bernhard Thomee, *Physikalisch nichtlineare Berechnung von Stahlfaserbetonkonstruktionen*, 2005.
4	Fernaß Daoud, *Formoptimierung von Freiformschalen - Mathematische Algorithmen und Filtertechniken*, 2005.
5	Manfred Bischoff, *Models and Finite Elements for Thin-Walled Structures*, 2005.
6	Alexander Hörmann, *Ermittlung optimierter Stabwerkmodelle auf Basis des Kraftflusses als Anwendung plattformunabhängiger Prozesskopplung*, 2006.
7	Roland Wüchner, *Mechanik und Numerik der Formfindung und Fluid-Struktur-Interaktion von Membrantragwerken*, 2006.
8	Florian Jurecka, *Robust Design Optimization Based on Metamodeling Techniques*, 2007.
9	Johannes Linhard, *Numerisch-mechanische Betrachtung des Entwurfsprozesses von Membrantragwerken*, 2009.
10	Alexander Kupzok, *Modeling the Interaction of Wind and Membrane Structures by Numerical Simulation*, 2009.
11	Bin Yang, *Modified Particle Swarm Optimizers and their Application to Robust Design and Structural Optimization*, 2009.

Band Titel

12 Michael Fleischer, *Absicherung der virtuellen Prozesskette für Folgeoperationen in der Umformtechnik*, 2009.

13 Amphon Jrusjrungkiat, *Nonlinear Analysis of Pneumatic Membranes - From Subgrid to Interface*, 2009.

14 Alexander Michalski, *Simulation leichter Flächentragwerke in einer numerisch generierten atmosphärischen Grenzschicht*, 2010.

15 Matthias Firl, *Optimal Shape Design of Shell Structures*, 2010.

16 Thomas Gallinger, *Effiziente Algorithmen zur partitionierten Lösung stark gekoppelter Probleme der Fluid-Struktur-Wechselwirkung*, 2011.

17 Josef Kiendl, *Isogeometric Analysis and Shape Optimal Design of Shell Structures*, 2011.

18 Joseph Jordan, *Effiziente Simulation großer Mauerwerksstrukturen mit diskreten Rissmodellen*, 2011.

19 Albrecht von Boetticher, *Flexible Hangmurenbarrieren: Eine numerische Modellierung des Tragwerks, der Hangmure und der Fluid-Struktur-Interaktion*, 2012.

20 Robert Schmidt, *Trimming, Mapping, and Optimization in Isogeometric Analysis of Shell Structures*, 2013.

21 Michael Fischer, *Finite Element Based Simulation, Design and Control of Piezoelectric and Lightweight Smart Structures*, 2013.

22 Falko Hartmut Dieringer, *Numerical Methods for the Design and Analysis of Tensile Structures*, 2014.

23 Rupert Fisch, *Code Verification of Partitioned FSI Environments for Lightweight Structures*, 2014.

24 Stefan Sicklinger, *Stabilized Co-Simulation of Coupled Problems Including Fields and Signals*, 2014.

Band Titel

25 Madjid Hojjat, *Node-based parametrization for shape optimal design*, 2015.

26 Ute Israel, *Optimierung in der Fluid-Struktur-Interaktion - Sensitivitätsanalyse für die Formoptimierung auf Grundlage des partitionierten Verfahrens*, 2015.

27 Electra Stavropoulou, *Sensitivity analysis and regularization for shape optimization of coupled problems*, 2015.

28 Daniel Markus, *Numerical and Experimental Modeling for Shape Optimization of Offshore Structures*, 2015.

29 Pablo Suárez, *Design Process for the Shape Optimization of Pressurized Bulkheads as Components of Aircraft Structures*, 2015.

30 Armin Widhammer, *Variation of Reference Strategy - Generation of Optimized Cutting Patterns for Textile Fabrics*, 2015.

31 Helmut Masching, *Parameter Free Optimization of Shape Adaptive Shell Structures*, 2016.

32 Hao Zhang, *A General Approach for Solving Inverse Problems in Geophysical Systems by Applying Finite Element Method and Metamodel Techniques*, 2016.

33 Tianyang Wang, *Development of Co-Simulation Environment and Mapping Algorithms*, 2016.

34 Michael Breitenberger, *CAD-integrated Design and Analysis of Shell Structures*, 2016.

35 Önay Can, *Functional Adaptation with Hyperkinematics using Natural Element Method: Application for Articular Cartilage*, 2016.

36 Benedikt Philipp, *Methodological Treatment of Non-linear Structural Behavior in the Design, Analysis and Verification of Lightweight Structures*, 2017.

Band Titel

37 Michael Sean Andre, *Aeroelastic Modeling and Simulation for the Assessment of Wind Effects on a Parabolic Trough Solar Collector*, 2018.

38 Andreas Apostolatos, *Isogeometric Analysis of Thin-Walled Structures on Multipatch Surfaces in Fluid-Structure Interaction*, 2019.

39 Altuğ Emiroğlu, *Multiphysics Simulation and CAD Integrated Shape Optimization in Fluid-Structure Interaction*, 2019.

40 Mehran Saeedi, *Multi-Fidelity Aeroelastic Analysis of Flexible Membrane Wind Turbine Blades*, 2017.

41 Reza Najian Asl, *Shape optimization and sensitivity analysis of fluids, structures, and their interaction using Vertex Morphing parametrization*, 2019.

42 Ahmed Abodonya, *Verification Methodology for Computational Wind Engineering Prediction of Wind Loads on Structures*, 2020.

43 Anna Maria Bauer, *CAD-integrated Isogeometric Analysis and Design of Lightweight Structures*, 2020.

44 Andreas Winterstein, *Modeling and Simulation of Wind-Structure Interaction of Slender Civil Engineering Structures Including Vibration Mitigation Systems*, 2020.

45 Franz-Josef Ertl, *Vertex Morphing for Constrained Shape Optimization of Three-dimensional Solid Structures*, 2020.

46 Daniel Baumgärtner, *On the Grid-based Shape Optimization of Structures with Internal Flow and the Feedback of Shape Changes into a CAD Model*, 2020.

47 Mohamed Khalil, *Combining Physics-based models and machine learning for an Enhanced Structural Health Monitoring*, 2021.

48 Long Chen, *Gradient Descent Akin Method*, 2021.

Band	Titel
49	Aditya Ghantasala, *Coupling Procedures for Fluid-Fluid and Fluid-Structure Interaction Problems Based on Domain Decomposition Methods*, 2021.
50	Ann-Kathrin Goldbach, *The CAD-Integrated Design Cycle for Structural Membranes*, 2021.
51	Iñigo Pablo López Canalejo, *A Finite-Element Transonic Potential Flow Solver with an Embedded Wake Approach for Aircraft Conceptual Design*, 2022.
52	Mayu Sakuma, *An Application of Multi-Fidelity Uncertainty Quantification for Computational Wind Engineering*, 2022.
53	Suneth Warnakulasuriya, *Development of Methods for Finite Element-Based Sensitivity Analysis and Goal-Directed Mesh Refinement Using the Adjoint Approach for Steady and Transient Flows*, 2022.
54	Klaus Bernd Sautter, *Modeling and Simulation of Flexible Protective Structures by Coupling Particle and Finite Element Methods*, 2022.